ABSTRACT

Stellar Helium Burning: A Further Measurement of the Beta-Delayed Alpha-Particle Emission of ^{16}N

Ralph Hayward France III
Yale University
1997

The $^{12}C(\alpha,\gamma)^{16}O$ reaction is of critical importance for understanding stellar evolution. During helium burning this reaction competes with the triple-alpha reaction that forms carbon. The final carbon/oxygen ratio at the end of this burning stage largely determines the final stages of the star. The beta-delayed alpha-emission of ^{16}N (i.e. prompt alpha-particles emitted from excited states of ^{16}O populated by the slow beta-decay of ^{16}N) has been predicted to provide a constraint on the cross section of this reaction, but requires a high sensitivity (B.R. ~ 10^{-9}) measurement. The low energy portion of the alpha-particle spectrum has been predicted to provide a sensitive means to deduce the reduced alpha-particle width of the bound 1^- state in ^{16}O.

In the past few years three attempts have been made to constrain the p-wave component of this cross section using the beta-delayed alpha-particle emission of ^{16}N. In this work we have made a high statistics measurement of this spectrum as a continuation of our earlier low statistics Yale-UConn experiment. We have improved the statistics by a factor of more than 5, the energy resolution by 20%, and we demonstrate an understanding of our line shape from known and measured quantities.

Our newly measured spectrum is compared to the three previous high statistics experiments and found to be consistent with the experimental results from Mainz and Seattle and inconsistent with those from TRIUMF.

Our discrepancy with the TRIUMF results is in the width of the primary peak, with the largest differences (nearly a factor of two) near the region of the interference minimum. This region of the spectrum determines the size of the f-wave contribution to the low energy secondary maximum. This is crucial as the magnitude of the p-wave contribution only is of importance to astrophysics due to the low energy (~300 keV) that stellar helium burning occurs in massive stars.

We conclude that with the current data sets the p-wave S-factor of the $^{12}C(\alpha,\gamma)^{16}O$ reaction cannot be determined at this stage with the accuracy (15-20 %) required for the stellar evolution models developed by Woosley and Weaver.

Stellar Helium Burning: A Further Measurement of the Beta-Delayed Alpha-Particle Emission of ^{16}N

A Dissertation
Presented to the Faculty of the Graduate School
of Yale University
in Candidacy for the Degree of
Doctor of Philosophy

by
Ralph Hayward France III
Dissertation Director: Moshe Gai
May 1997

for my dearest Ellen

ACKNOWLEDGEMENTS

This work would not have been possible without the help and support of many people. I am especially indebted to Moshe Gai, who has acted as my advisor for the past 8 years. I am deeply indebted to Zhiping Zhao, without whose efforts this experiment could never have been done. I would also like to thank Prof. D. Allan Bromley for being my official advisor for the period between Moshe Gai leaving Yale and receiving his appointment as Adjunct Professor. Prof. Bromley provided many useful comments regarding my future within physics.

I would like to thank my thesis committee: Moshe Gai, D. Allan Bromley, Francesco Iachello, Pierre Demarque, Charles Baltay, and Thierry Delbar for their helpful remarks. I am particularly indebted to Prof. Baltay, whose careful criticism made this a much superior work.

I would like to especially thank Ed Wilds, whose thesis work involved the same aparatus. Without his help this experiment would never have been completed.

I would like to also thank the other members of our group who collaborated with us on this experiment over the years. Early on there were Sumit Sen, Brian Lund,Sinan Utku, Brian Young, Steve Rugari, K. S. Lai, and Kevin Beard. In the last stages of the experiment we received significant help from James McDonald, Glenn Mac Lachlin, and Rebecca Jarvis. I would also like to thank Al Howard for many helpful discussions throughout the early experimental runs.

Special thanks must be reserved for Bob McGraff, John Barris, and Tom Barker, all of whom put in a great deal of extra effort which allowed this experiment to succeed.

I thank my colleagues and the staff at the Wright Nuclear Structure Laboratory and the Physics department for all their help over the years. In particular I would like to thank Jeff Ashenfelter, Nick Bateman, Sara Batter, Jean Belfonti, Dee Berenda, Dan Blumenthal, Charles Bockelman, Rita Bonito, Felix Chan, Amir Chisti, Partha Chowdhury, Joe Cimino, Phil Clarkin, Lisa Close, Ben Crowell, Karen DeFelice, Teddy Duda, Pat Ennis, Sam Ezeokoli, Walter Garnet, Joe Germani, Vicki Greene, Kevin Hahn, Kevin Hubbard, Al Jeddry, Nick Kaloskamis, Shiva Kumar, Tom Leonard, Craig Levin, Paul Paul Magnus, Don McDuff, Jeff Mitchell, Allen Ouellette, Peter Parker, Bernard Phlips, Kenzo Sato, Bill Schief, Mary Anne Schulz, Michael Smith, Stuart Smolen, Dick Wagner, Chris Winter, Kazim Yildiz, Mike Zeller.

I would like to thank my parents for helping to support me throughout my many years as a graduate student, and I would like to thank the vertebrate paleontologists Tom Holtz, Christine Chandler, and Makoto Manabe as well as my apartment mates Parley Agner and Nicholas Rennie who helped make my stay in New Haven bearable.

Table of Contents

I Introduction 1

II Nuclear Astrophysics 7
- A Introduction 7
- B Helium Burning 12
- C S-Factor Parametrization 14

III R-Matrix Parametrization 16

IV Experimental Procedure 24
- A Overview 24
- B ^{15}N Beam 25
- C Deuterium Target 26
- D Vacuum System 27
- E Catcher Foils 27
- F Alignment 30
- G Arm Rotation 31
- H The Detectors 31
- I Data Acquisition 36
- J Energy Calibration 43
- K Coincidence Calibration 45
- L Detector Efficiency 53

V Experimental Results and Data Analysis 56
- A Alpha-Particles in Singles 56
- B Alpha-Particles in Coincidence 56
- C Background 56
- D Corrections for Energy Shifts 63

E Correction for Line Shape 63

VI Discussion 69

VII Conclusion 84

Appendix A Tabulated Previous Data Sets 85

Appendix B Letter from H. Wäffler to F.C. Barker 90

Appendix C Tabulated Yale-UConn(‘96) Data Set and TRIUMF(‘94) and Seattle(‘95) Theory Curves 95

References 100

Table of Tables

4.1 Tabulated Contaminant Lines 48

Table of Figures

1.1 Early Theoretical Predictions. 2
1.2 Preliminary Fits by Gerry Hale. 3
1.3 Simplified Decay Scheme for the beta-decay of ^{16}N 4
1.4 The three previous ^{16}N beta-delayed alpha-particle spectra covering the region of the secondary maximum and minimum. 6

2.1 Two Hertzprung-Russel diagrams. 8
2.2 Schematic HR Diagram 9
2.3 The evolution of a 25 solar mass star. 11
2.4 Partial level scheme for the triple alpha-particle capture reaction. 13
2.5 Partial level scheme for the $^{12}C(\alpha,\gamma)^{16}O$ reaction. 13

4.1 Schematic diagram of the experimental set up. 28
4.1b Photograph of main vacuum chamber 29
4.2 Time structure of the ^{16}N and ^{8}Li experiments. 32
4.3a Layout of the Alpha-Array 33
4.3b Layout of the Beta-Array. 33
4.3c Layout During $^{10}B(n,\alpha)^{7}Li$ calibration runs 34
4.4a Schematic of the electronics located in the High Energy Vault which controlled the beam chopper and relayed back the chopper's position. 37
4.4b Schematic of electronics located in Target Room 2. 37

4.4c Schematic of SSB detector energy electronics. 39
4.4d Schematic of the time of flight electronics. 39
4.4e Schematic of the Alpha timing I electronics. 40
4.4f Schematic of the event logic electronics. 42
4.5 Typical source spectrum from ^{148}Gd, ^{208,209}Po, and ^{241}Am. 44
4.6 Typical spectrum from the ^{10}B(n,α)^{7}Li reaction. 46
4.7 Typical contaminant spectrum. 47
4.8 Typical energy spectrum from ^{227}Ac. 50
4.9 Typical timing spectrum from ^{227}Ac. 51
4.10 Typical ^{8}Li beta-delayed alpha-particle spectrum. 52
4.11 Summed 2d timing vs. alpha-particle energy plot for beta-delayed alpha-particles from ^{8}Li. 55

5.1 Alpha-particle spectrum measured in singles. 57
5.2 Summed ^{16}N data in 2d timing vs. energy plot. 58
5.3 Typical 50 keV wide slices from the 2d ^{8}Li and^{16}N time vs. energy plots projected upon the time axis. 59
5.4 Uncorrected beta-delayed alpha-partilce spectrum of ^{16}N. 60
5.5 Spectrum of beta-delayed alpha-particles from ^{16}N corrected for beta array coincidence efficiency. 61
5.6 Beta-delayed alpha-particle spectra from both Yale-UConn experiments showing the same line shape. 64
5.7 The energy and time resolution of the Yale-UConn(‘96) experiment as a function of energy. 65

5.8 Final beta-delayed alpha-particle spectrum. 67

6.1 Mainz('71) beta-delayed alpha-particle spectrum from ^{16}N. 70
6.2 TRIUMF('94) fitted curve compared with Seattle('95) fitted curve. 72
6.3 Mainz('71) data compared with TRIUMF('93) and Seattle('95) fitted curves. 73
6.4 Comparison of TRIUMF('94) and Seattle('95) fitted curves after averaging over the Yale-UConn('96) experimental resolution. 75
6.5 Yale-UConn('96) data as compared to the averaged TRIUMF('94) and Seattle('95) fitted curves. 76
6.6a Normalized ratio of Mainz('71) data to Seattle('95) data. 78
6.6b Normalized ratio of TRIUMF('94) data to Mainz('71) data. 79
6.6c Normalized ratio of TRIUMF('94) data to Seattle('95) data. 80
6.7a Normalized ratio of the averaged TRIUMF('94) fitted curve to the Yale-UConn('96) data. 81
6.7b Normalized ratio of the averaged Seattle('95) fitted curve to the Yale-UConn('96) data. 82
6.8 Normalized ratio of TRIUMF('93) data to TRIUMF('94) data. 83

I: INTRODUCTION

Since the early 1970's [Ba71] there has been intense interest in using the beta-delayed alpha-particle emission of ^{16}N to determine the rate of the ^{12}C(α,γ)^{16}O reaction during stellar helium burning. As shown in fig. 1.1, the energy spectrum of these alpha-particles over the region of interest was predicted to be dominated by a single broad 1^- state at 2.35 MeV and to have a secondary interference maximum at approximately 1.1 MeV with a minimum at about 1.4 MeV. Originally, it was advocated that the height of the secondary maximum is particularly sensitive to the p-wave astrophysical S-Factor (defined below) [Hu91, Ji90, Ba88].

However, more recently, it was demonstrated that the ^{16}N data that was fitted with large S-factors of 95 keVb [Zh93] and 81 keVb [Az94] can also be fitted with a small S-factor of 10-20 keVb [Ha96, Zh95], as shown in fig 1.2. As we discuss later, this new result raises serious doubts as to our ability to extract the S-factor unambiguously from current data.

In the beta-delayed alpha-particle emission of ^{16}N, ^{16}N (in its ground state) beta-decays to ^{16}O. The majority of the time the ^{16}N decays into either the ground state (B.R. = 26%) or the 3^- excited state at 6.13 MeV (B.R. = 68%) in ^{16}O. The decay scheme is shown in fig 1.3. The 2^+ states, which are of importance astrophysically, are not populated due to beta-decay parity selection rules; thus, these data can only probe the E1 component of the desired cross section.

The measured spectra are composed of p-wave and f-wave contributions. Most of the alpha-particle spectrum comes from the interference between the two 1^- states at 9.63 and 7.12 MeV; however, a small admixture from the tail of the 3^- state at 6.13 MeV also contributes. Due to the small energies present during stellar helium burning, only the 1^- (p-wave) component is of importance in astrophysics; thus, determining the 3^- (f-wave)

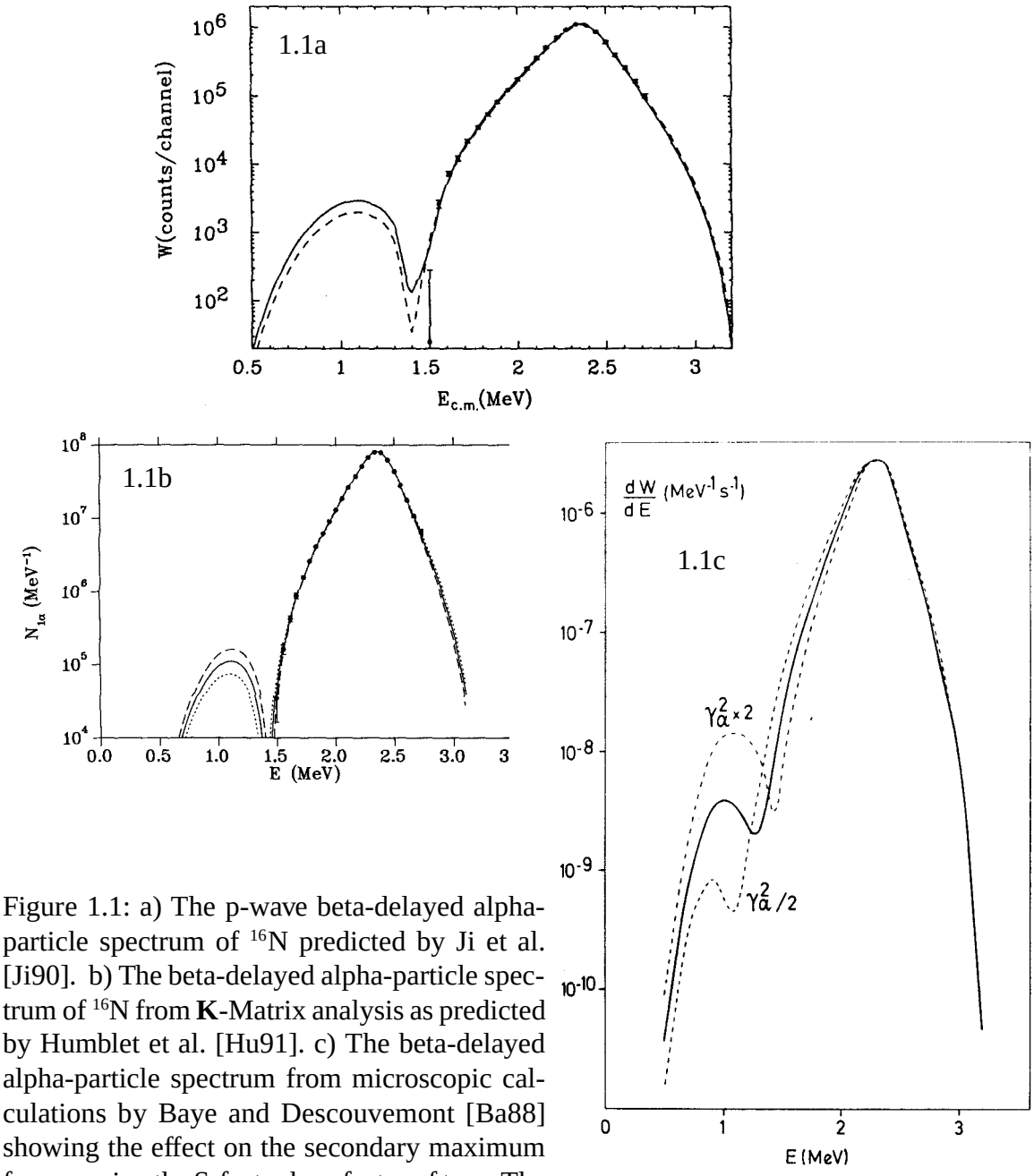

Figure 1.1: a) The p-wave beta-delayed alpha-particle spectrum of ^{16}N predicted by Ji et al. [Ji90]. b) The beta-delayed alpha-particle spectrum of ^{16}N from **K**-Matrix analysis as predicted by Humblet et al. [Hu91]. c) The beta-delayed alpha-particle spectrum from microscopic calculations by Baye and Descouvemont [Ba88] showing the effect on the secondary maximum from varying the S-factor by a factor of two. The secondary maximum is predicted at the extremely low branching ratio of 10^{-9}.

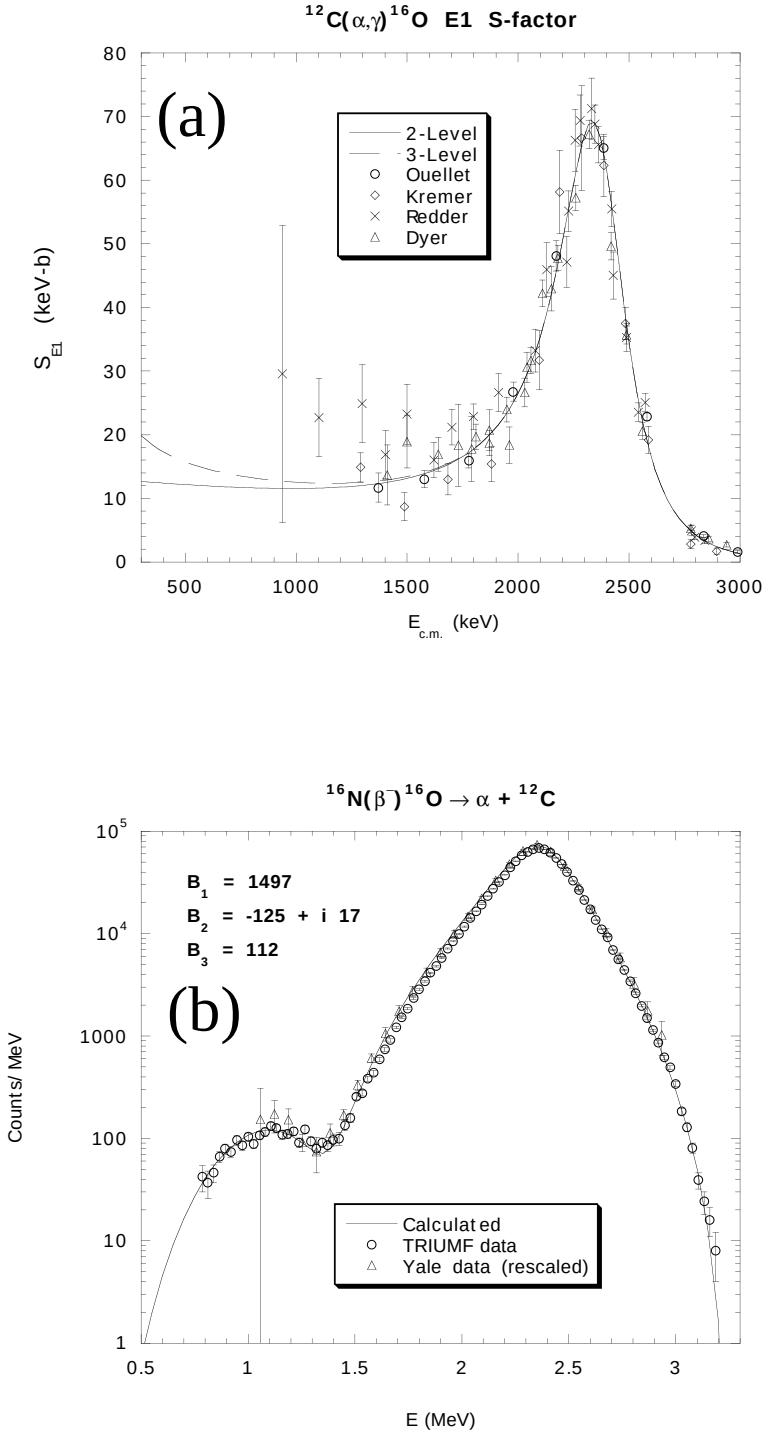

Fig 1.2: Preliminary fits provided by Gerry Hale [Ha96] to (a) direct measurements of $^{12}C(\alpha,\gamma)^{16}O$ and (b) indirect measurements using the beta-delayed alpha-particle emission of ^{16}N. The two data set used in (b) are the original Yale-UConn('93) and the TRIUMF data sets. These fits show that the data sets are consistant with low values of S_{E1}(300 keV) of 20 keVb or smaller.

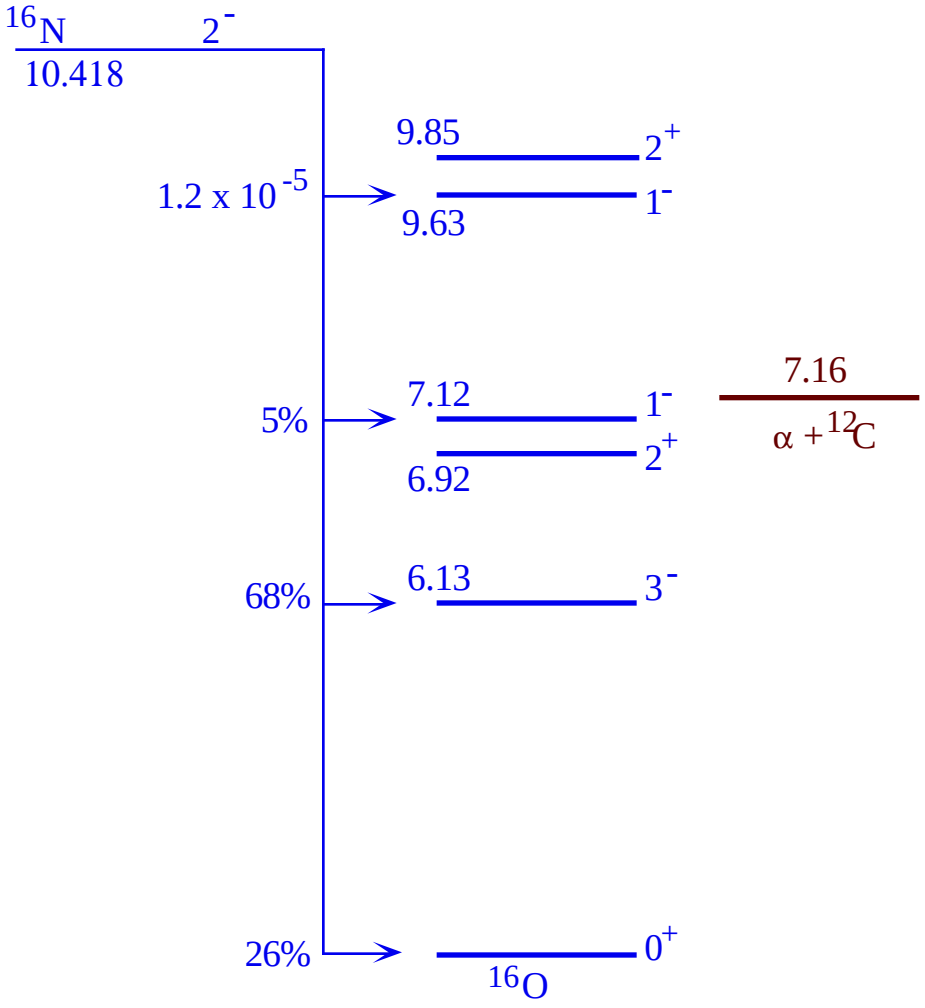

Fig 1.3. Simplified decay scheme for the beta-decay of ^{16}N. The quasibound 1^- state at 9.63 is 400 keV wide and its decay is the source of the primary peak seen in the beta-delayed alpha-particle spectra. The secondary maximum is composed of an admixture of the interference between the quasibound 1^- state at 9.63 MeV and the tail of the just bound 1^- state at 7.12 MeV and the tail of the bound 3^- state at 6.13 MeV.

component of the secondary maximum and subtracting it out is of great importance. The centroid of the primary peak is shifted downwards in energy from 2.47 MeV to 2.35 MeV due to the E^5 energy dependency of beta-decay.

Prior to the experiment reported here, four measurements were made on the beta-delayed alpha-emission spectrum of ^{16}N; three of these are shown in fig. 1.4: the first Yale-UConn experiment by Zhao *et al*. [Zh93a, Zh93b], the Seattle experiment by Zhao *et al*. [Zh95], and the TRIUMF experiment by Buchmann *et al*. [Bu93, Az94]. As is apparent in fig. 1.4, these data sets agree fairly well over most of the spectrum; in particular, they agree over the secondary maximum at 1.1 MeV. However, there is a major discrepancy near the region of the minimum at 1.4 MeV related to discrepancies in the shape of the primary peak centered at 2.35 MeV. In the region of the interference minimum, the Seattle data set is nearly a factor of two higher than the TRIUMF data set. The minimum is of great importance, as it determines the f-wave contribution to the spectrum. For a larger f-wave contribution, the p-wave contributes a smaller fraction of the secondary maximum, and the extracted S-factor is smaller.

The original Yale-UConn experiment had systematic uncertainties and insufficient statistics to determine the depth of the minimum, so a second improved experiment was necessary. In the experiment reported here, we have increased the statistics by more than a factor of five and improved the energy resolution by 20%. We also understand the line shape of both Yale-UConn experiments using known and measured quantities, eliminating the systematic uncertainties resulting from to the problematic unfolding procedures used in our earlier experiment.

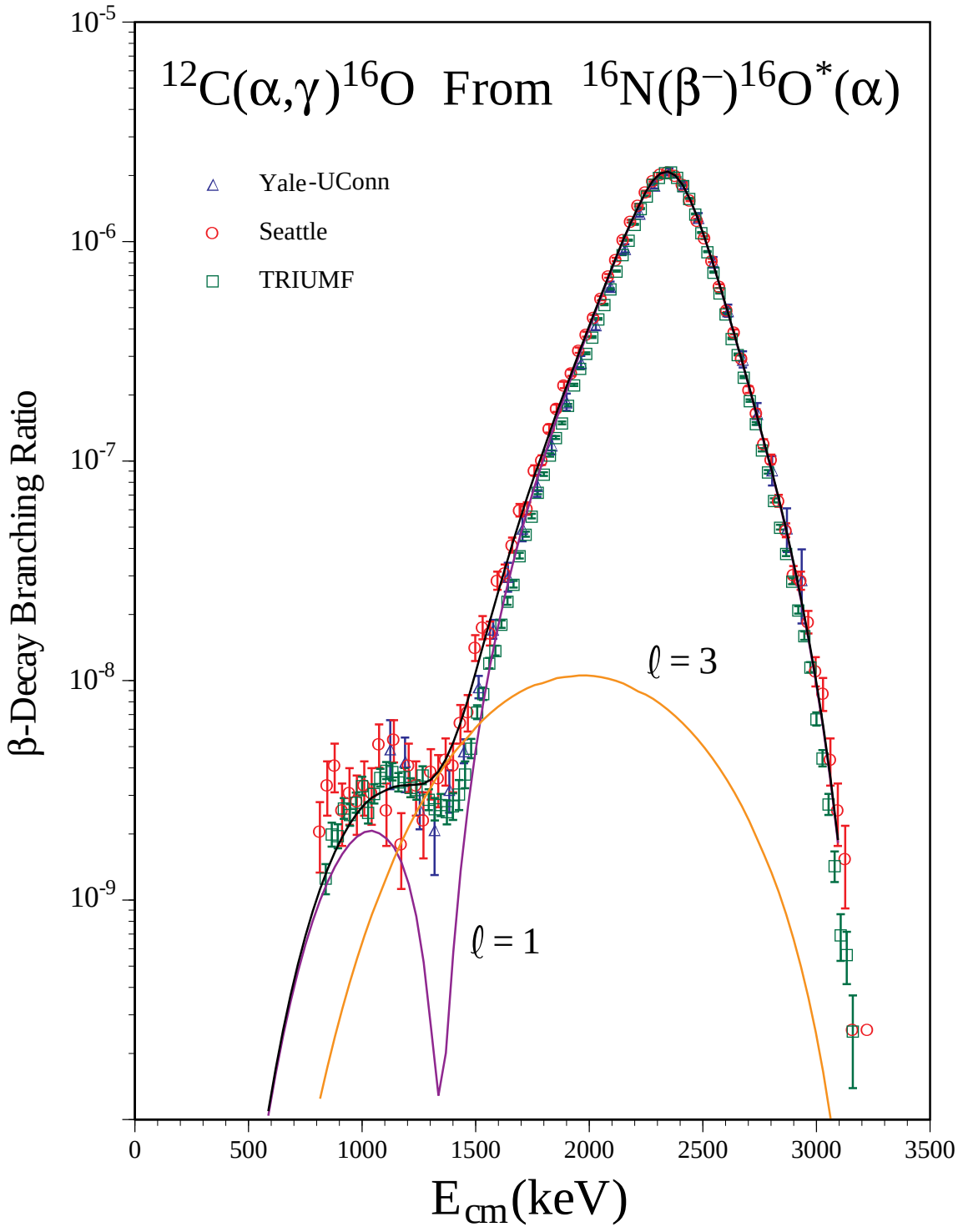

Figure 1.4: The three previous ^{16}N beta-delayed alpha-particle emission spectra covering the region of the secondary maximum and minimum. The principle region of disagreement is the minimum around 1.4 MeV where the Seattle data set [Zh94] exceeds the TRIUMF [Bu93, Az94] data set by about a factor of two related to a disagreement over the width of the priciple peak. The included curve is an **R**-Matrix fit to the Seattle data [Zh94].

II: Nuclear Astrophysics

A. Introduction

Nuclear Astrophysics is the study of nuclear processes that take place naturally throughout the cosmos—processes which have produced all elements heavier than hydrogen and provide the energy source for stars, novae, and some supernovae. Other than the elements lighter than carbon, nearly all nuclei were formed in stars. During their life, and sometimes violently during their deaths, stars expel large amounts of astrated material into space—material which has been enriched in heavy elements ($Z \geq 6$) through stellar processing. Studying the distribution of the isotopes and the nuclear reactions that take place in stars is thus important in understanding stellar evolution and the origin of the elements on Earth.

In 1911 Ejnar Hertzsprung used a diagram to show differences between giant stars and dwarf stars in a star cluster. In 1913 Henry Norris Russell used a similar diagram of all stars with measured parallax [Ga92]. These diagrams, now called Hertzsprung-Russel (HR) diagrams have a logarithmic measure of absolute luminosity on the y-axis, and a measure of temperature (e.g. Blue minus Visual color magnitudes or B-V) on the x-axis (fig 2.1, 2.2). Most stars fall along a diagonal band, the main sequence (fig 2.2), and are burning hydrogen in their cores.

During hydrogen burning, stars are powered by the conversion of protons into alpha-particles [Cl83, Ro88]. After the hydrogen in their cores is consumed, the stars leave the main sequence and proceed along the subgiant and red giant branches (fig 2.2). During this phase of their existence, the stars are powered by hydrogen burning in a thin shell about their core; their outer atmospheres balloon out and become rarified; while, with no nuclear power source within the core itself, the core begins to contract under self gravitation converting gravitational potential energy into thermal energy. Eventually the core becomes hot and dense enough for helium burning to begin.

During Helium burning, stars move onto the Horizontal Branch of the HR-diagram (fig. 2.2) primarily producing ^{16}O and ^{12}C through the combination of alpha-particles via

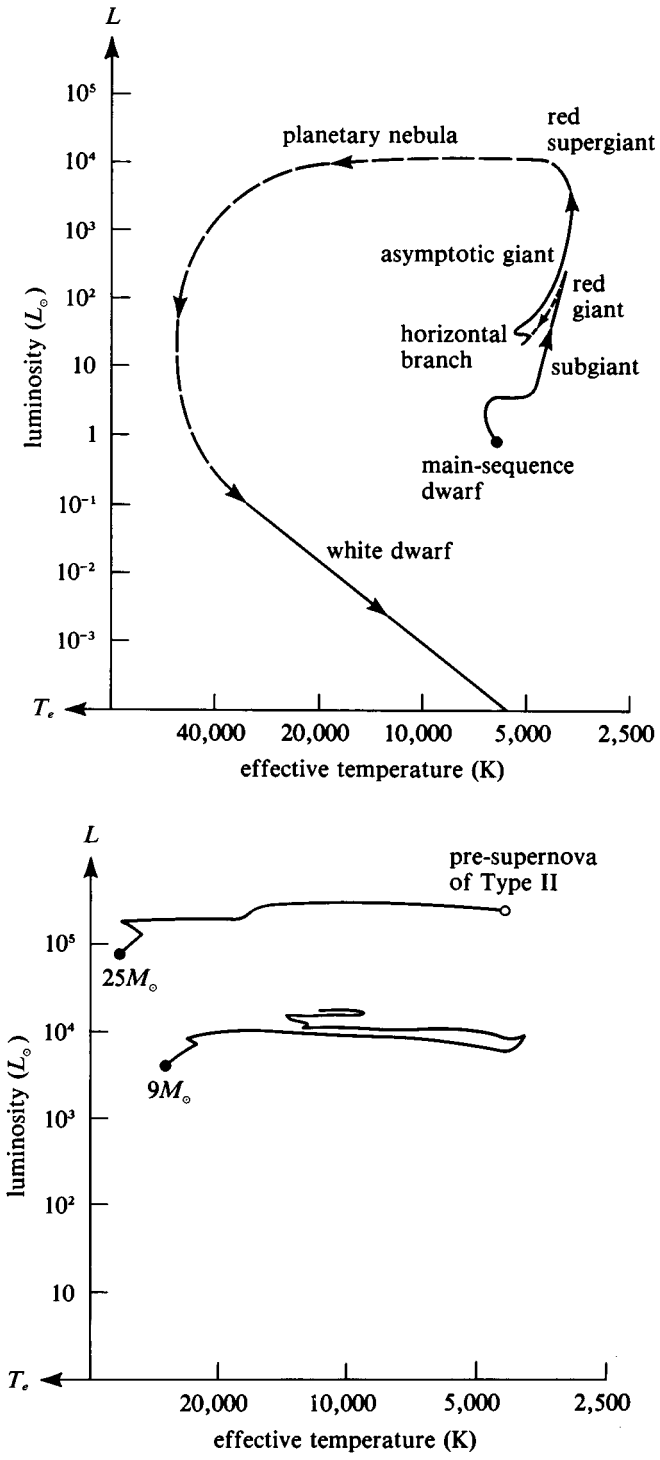

Figure 2.1: Two Hertzprung-Russel diagrams taken from ref [Sh82]. The top shows the evolution of a typical ~1 solar mass star. The lower diagram shows the evolution of heavier 9 and 25 solar mass stars.

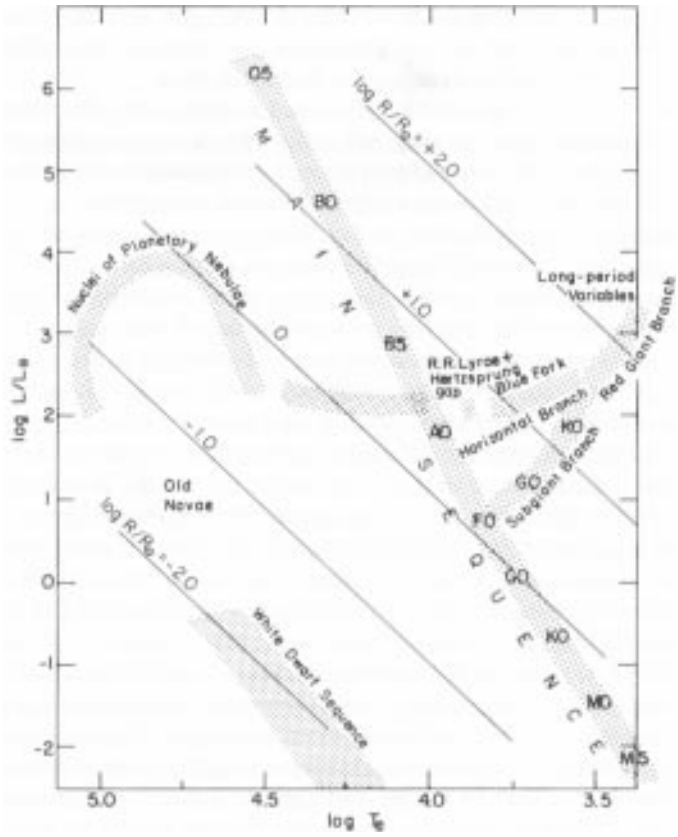

Fig 2.2 Schematic HR diagram taken from [Ha91] showing the main sequence and principal branches. The lines of constant slope represent stars having identical radii.

the triple-alpha process and the $^{12}C(\alpha,\gamma)^{16}O$ reaction (described below). The star will continue on the horizontal branch until the helium in its core has been exhausted. What happens next depends upon the mass of the star. After exhaustion of the helium fuel, the stellar core again contracts converting gravitational energy into thermal energy. For stars which started with mass less than 8 solar masses, the core fails to reach the conditions necessary for carbon burning. After undergoing mass loss these stars end up as Carbon-Oxygen white dwarfs [Ro88]. In stars starting with masses between 8 and 10 solar masses carbon burning does occur. Carbon burning results in oxygen and neon, and, after undergoing mass loss, such stars become Oxygen-Neon white dwarfs.

More massive stars undergo a series of burning stages interspersed with core contraction stages. First carbon burning followed by neon burning, oxygen burning and finally silicon burning [Ro88]. Silicon burning is actually a photodisintegration process where the some heavy nuclei are broken up into lighter particles which combine with silicon and heavier nuclei until highly neutron rich iron group nuclei are produced. The iron group nuclei are unable to provide any further source of nuclear energy as they have the maximum binding energy per nucleon. When the core formed of the iron group nuclei can no longer support itself against gravity via thermal and degeneracy pressure, it collapses and a supernova explosion occurs. The star expels most of its mass, now highly enriched in heavy ($Z \geq 6$) nuclei, and leaves behind either a black hole or a neutron star. Fig. 2.3 shows a schematic cone taken from a 25 solar mass star just before detonation [We86, Br85]. It shows how the various burning shells form about the iron core and the expected durations of each burning phase. Note that the original figure produced by G.E. Brown and H. Bethe [Br85] based upon computer simulations of S. Woosley and T. Weaver [We80, Wo86], as shown here (fig 2.3), had the x-axis incorrectly labeled (by a factor of 10). E.g., while helium burning commences at approximately 200 MK (~20 keV) it was labelled [Br95] at 20 MK.

The detailed structure of the star and the history of its burning stages are highly dependent upon the results of the helium burning process. During the heavy ion burning

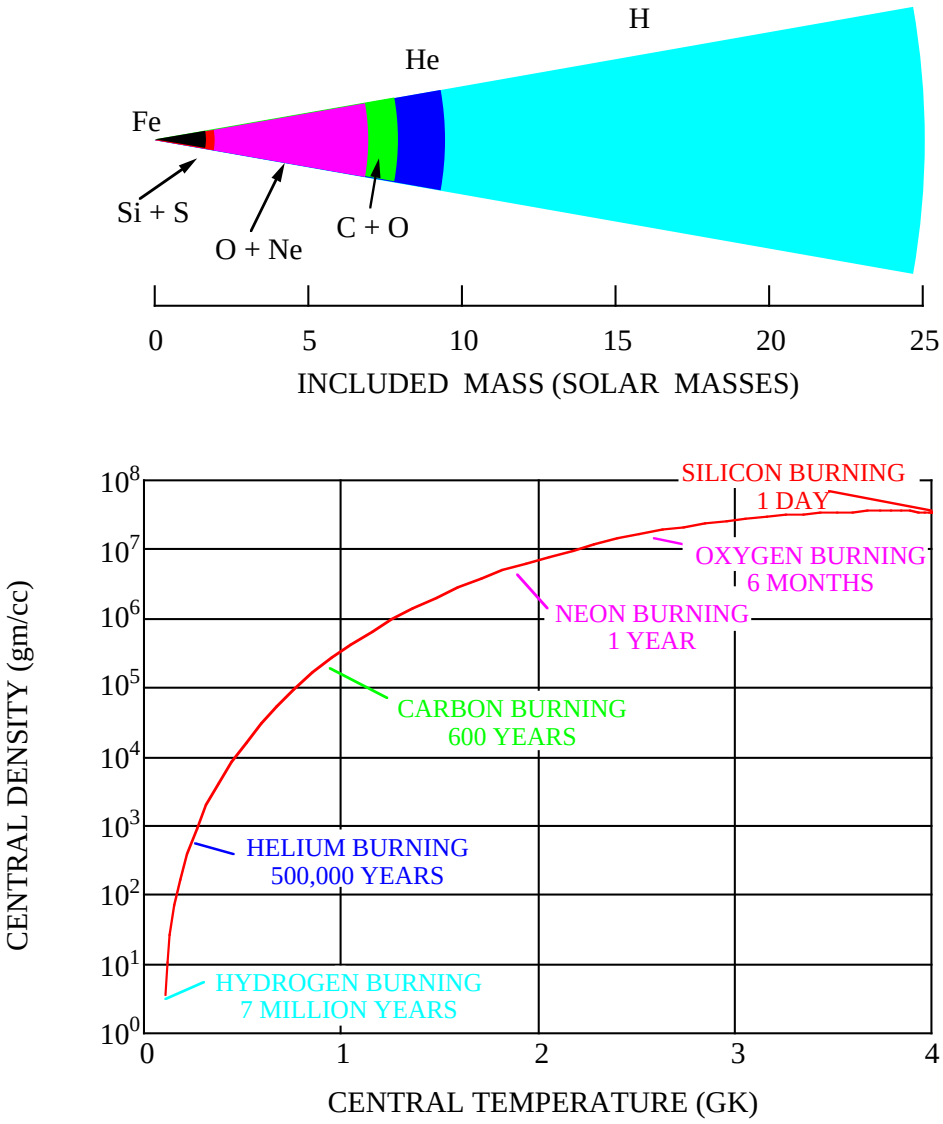

Figure 2.3: The evolution of a 25 solar mass star. The various burning stages produce an onion like structure with shells of different elements surrounding an iron core. (Figure taken from [Be85] with correction as discussed in text)

stages, the core of the star is rapidly cooled (i.e. the core decreases in entropy) through neutrino emission. This decrease in entropy leads to a smaller iron core at the time of collapse. However, if insufficient carbon (<15% carbon in the carbon/oxygen shell for 25 solar mass stars [We93]) is left at the end of helium burning, then the carbon and neon burning stages may be skipped entirely, with the star proceeding directly to oxygen burning. By skipping these stages the resulting iron core is hotter and thus larger and collapses into a black hole.

B. Helium Burning

There exist no stable mass 5 or 8 nuclei. Carbon is produced via the triple-alpha reaction, a double resonance process. First two separated alpha-particles react to produce ^{8}Be in its ground state, which is only unbound by 91.78 keV. Since ^{8}Be has a lifetime of only 7 x 10^{-16} seconds a small concentration of ^{8}Be (~10^{-10} [Ro88]) forms in thermal equilibrium with the ^{4}He in the core. A 0^{+} energy level in ^{12}C was predicted by F. Hoyle [Ho54] to make ^{8}Be(^{4}He,γ)^{12}C into a resonant process. This 0^{+} state at 7.6542 MeV (287.7 keV above threshold) was later discovered at the Kellogg Laboratory of Caltech. The rate of the triple alpha reaction is thus determined by the properties of these two resonances. The nuclear levels involved are shown in figure 2.4. This rate is thought to be understood to within 15% accuracy [Ro88].

The second important reaction taking place during helium burning is the ^{12}C(α,γ)^{16}O reaction. At the most efficient energies in stellar helium burning (~300 keV), this reaction is dominated by the tail of the (as yet unknown) alpha widths of two subthreshold states—a 1^{-} state at 45 keV below and a 2^{+} state at 240 keV below the alpha-particle capture threshold at 7.16 MeV. This work is concerned with measurement of the $l = 1$ (p-wave) contribution. The nuclear levels involved are shown in figures 1.3 and 2.5.

The two most uncertain items that are needed to extract the p-wave component at Helium burning temperatures ($S_{E1}(300)$) are the reduced alpha-width of the bound 1^{-} state

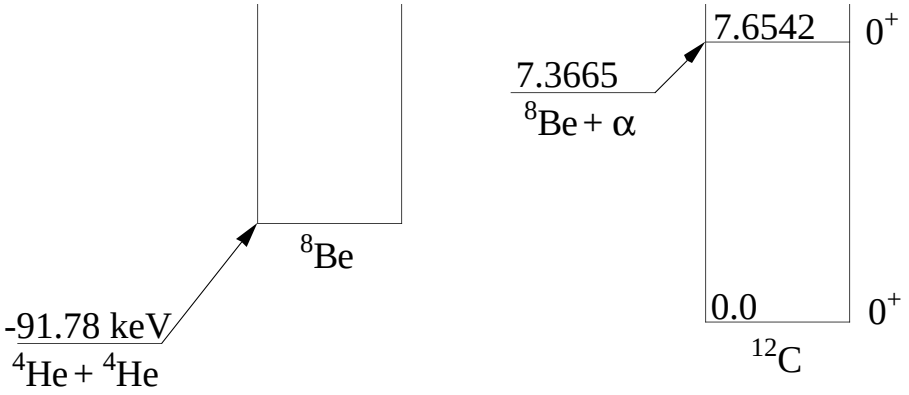

Figure 2.4: Partial level scheme for the triple alpha-particle capture reaction (not drawn to scale).

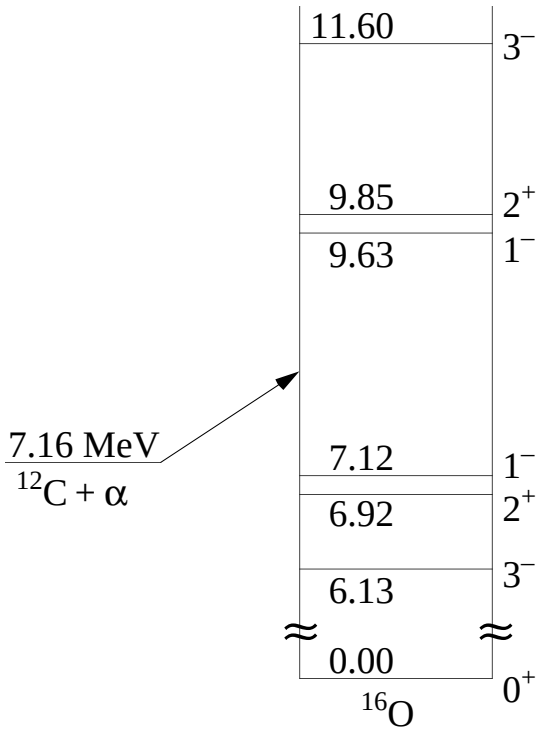

Figure 2.5: Partial level scheme for the $^{12}C(\alpha,\gamma)^{16}O$ reaction (not drawn to scale).

and the sign of the interference between this state and the quasibound broad 1^- state at 9.63 MeV. **R**-Matrix analyses allow constraints to be established on the reduced alpha-width of the bound 1^- state, and for high (~100 keV barns) values of the S-factor can constrain the sign of the above mentioned interference as well.

Since the carbon/oxygen ratio at the conclusion of the helium burning phase determines the final destiny of the star (i.e. black hole or neutron star) for stars of equal mass and varies linearly with the rate of the $^{12}C(\alpha,\gamma)^{16}O$ reaction [We93], this is a crucial rate for understanding stellar evolution for massive stars.

C. S-Factor Parameterization

In stars undergoing helium burning, the average kinetic energy of the nuclei as given by 3kT/2 is small compared to the coulomb barrier. Helium burning occurs at 200 MK. The coulomb barrier is given by:

$$V = \frac{Z_1 Z_2 e^2}{R} \approx \frac{Z_1 Z_2}{\sqrt[3]{A_1} + \sqrt[3]{A_2}}\, MeV \tag{1.1}$$

where Z_1 and Z_2 are the atomic numbers of particles of mass A_1 and A_2 separated by distance R. For the reaction $^{12}C(\alpha,\gamma)^{16}O$, this value, ~3 MeV, is much greater than kT ~ 20 keV. Such reactions are made possible through a combination of penetration through the coulomb barrier and the high energy tail of the Maxwell-Boltzmann energy distribution. The convolution of the Maxwell-Boltzmann distribution with the coulomb penetration term yields a peak [Cl83] at ~300keV. This peak is called the Gamow window and is the effective energy at which the reaction mostly occurs.

At astrophysical energies, Gamow and Bethe suggested parameterization of the cross section as:

$$\sigma = \frac{S(E)}{E} e^{-2\pi\eta} \tag{1.2}$$

$$\eta = \frac{Z_1 Z_2 e^2}{\hbar v} \tag{1.3}$$

where η is the Sommerfeld parameter and S(E) is the astrophysical S-factor. The $e^{-2\pi\eta}$ term comes from the coulomb penetration, and the E^{-1} term is a geometric term: $\pi\lambda^2 \sim E^{-1}$ where λ is the de Broglie wavelength. With these two energy dependencies factored out, the S-factor varies with energy much more slowly than does the cross section itself. Hence extrapolations of the S-factor from laboratory measurements down to astrophysical energies can be performed more transparently than extrapolations of the cross section itself.

Usually this extrapolation is noncontroversial. In the case of the $^{12}C(\alpha,\gamma)^{16}O$ reaction however, uncertainty arises from the sign of the interference [Ji90] between the two 1^- states (at 9.63 MeV and 7.12 MeV see figs. 1.3 and 2.5); experiments prior to the beta-delayed alpha-particle emission experiments did not have the necessary sensitivity at low energies. Several direct capture experiments were performed [Dy74, Ke82, Kr88, Re87, Ou92] as well as a number of elastic scattering experiments [Pl87, Bi54, Jo62]. The extrapolated S-factor ranged from 0 to 300 keVb.

However, if these data are combined with the beta-delayed alpha-particle energy spectrum from ^{16}N, F.C. Barker predicted [Ba71, Ba87] that the E1 S-factor could be well constrained (see chap 3). This method provides several advantages. The beta-decay preferentially feeds the bound 1^- state at 7.12 and low energy continuum, since the beta-decay rate goes as the energy to the fifth power and the matrix element for decay to the bound state is predicted to be much enhanced over the matrix element for decay to the quasibound state at 9.63 MeV [Ba71, Ba87] (figs. 1.3). The problem in performing this experiment is that the portion of the spectrum sensitive to the S-factor is at a branching ratio of order 10^{-9}. Thus, this was originally thought to provide a new tool for the determination of the astrophysically important p-wave S-factor. As we discuss later, this work and that of others raise some difficulties with this suggestion.

III: The R-Matrix Parametrization

The **R**-Matrix formalism, first developed by Wigner and Eisenbud [Wi47, La58], may be used to fit simultaneously the $\alpha + {}^{12}C$ elastic scattering, ${}^{12}C(\alpha,\gamma){}^{16}O$ reaction, and ${}^{16}N(\beta^-){}^{16}O^*(\alpha)$ data sets. This global fit allows one to extract the reduced alpha width of the bound 1^- state and extract the astrophysical S-factor. In this discussion, I will closely follow the texts of Lane and Thomas [La58] and of Barker *et al*. [Ba66, Ba67, Ba68, Ba71, Ba87], starting by using the case of scattering between two nuclei resulting in another pair of nuclei, as an example to define its various portions.

In the **R**-Matrix theory, a set of states of the compound nucleus is defined and cross sections can be expressed in terms of these. In general, however, a set of intermediate quantities are actually used to calculate cross sections. We define $\sigma[c,c'](E)$ to be the cross section for the production of pair c' when the pair c collide at energy E. U[c',c] is an element of the collision matrix **U**, and is the amplitude of the outgoing waves of pair c' given a unit flux of incoming pair c. Hence, $\sigma[c,c']$ is proportional to $|U[c',c]|^2$.

The **R**-Matrix is a nondiagonal matrix which takes into account all the non-coulomb forces involved in the reaction and represents the only unknown quantities. Wigner and Eisenbud [Wi47] have shown that the energy dependence of the elements of **R** is given by:

$$R_{cc'}(E) = \sum_{\lambda} \frac{\gamma_{\lambda c}\gamma_{\lambda c'}}{E_\lambda - E'} \tag{3.1}$$

where λ labels the members of a complete set of basis states; the $\gamma_{\lambda c}$ are the reduced width amplitudes.

Four broad assumptions are made at the outset of R-Matrix theory:

i) Applicability of nonrelativistic quantum mechanics

ii) Absence or unimportance of all processes in which more than two product nuclei are formed.

iii) Absence or unimportance of all processes of creation or destruction. This condition must be relaxed somewhat in the case of photon emission.

iv) The existence, for any pair of nuclei c, of some finite radial distance a_c, beyond which neither nucleus experiences any polarizing field from the other. Generally any value of a_c large enough will do for the formal theory, however the smallest values are usually used and are given the name interaction radii.

The configuration space is divided into two regions called the internal and external regions. The internal region corresponds to the region of physical space where all the nucleons are close enough together for nuclear forces to operate. In the external region, the nucleons are separated into two groups which are separated far enough apart so that they cannot effect each other via nuclear forces.

The external region is divided into channels, each of which represents a different combination of the nucleons into two non-interacting nuclei. A channel surface separates each channel from the internal region. The channel surfaces correspond to the situation in physical space where $r_\alpha = a_\alpha$ where a_α is called the channel radius for channel α. When a_α is the minimum value such that the non-interaction condition is met, it is then referred to as the interaction radius.

This leads to the situation where there are many different channels for a given set of two nucleons. This is not desirable as the nucleons are Fermi-Dirac particles, and thus different combinations must be anti-symmetrized. In all further discussion, a channel of pair *c* will imply summation over the possible neutron and proton permutations possible.

The channel surface $\mathcal{S}$ is defined as the interface between the internal region and a channel in the external region. In physical space it is located where $r_c=a_c$.

From assumption i) we know that the wave function of the system must be given by the standard Schrödinger Equation $H\Psi = E\Psi$. The Hamiltonian, H, is composed of two parts: T, the kinetic energy operator, and V, the potential energy operator. T is of the form:

$$T = \sum_i \frac{\hbar^2}{2m_i} \nabla x_i^2 \tag{3.2}$$

In the external region T may be separated into four parts. The first two correspond to the centroid motion of each of the two nuclei, and the second two to the kinetic energy in internal motion. T now has the form:

$$T = -\frac{\hbar^2}{2M_{\alpha 1}} \nabla_{R_1}^2 + -\frac{\hbar^2}{2M_{\alpha 2}} \nabla_{R_2}^2 + (T_{Int})_{\alpha 1} + (T_{Int})_{\alpha 2} \tag{3.3}$$

The first two terms may be transformed into two other terms, the first representing the kinetic energy of the centroid of the entire system, and the second, the kinetic energy of relative motion:

$$T = -\frac{\hbar^2}{2M} \nabla_R^2 + -\frac{\hbar^2}{2M_\alpha} \nabla_{r_\alpha}^2 + (T_{Int})_{\alpha 1} + (T_{Int})_{\alpha 2} \tag{3.4}$$

Since we are in the external region V may be decomposed into the form:

$$V = (V_{Int})_{\alpha 1} + (V_{Int})_{\alpha 2} + V_c(r_\alpha) \tag{3.5}$$

Thus in the external region, the Hamiltonian is composed of four parts:

$$H = H_0 + H_c + H_{\alpha 1} + H_{\alpha 2} \tag{3.6}$$

where

$$H_0 = -\frac{\hbar^2}{2M} \nabla_R^2 \tag{3.7}$$

$$H_c = -\frac{\hbar^2}{2M_\alpha} \nabla_{r_\alpha}^2 + V_c(r_\alpha) \tag{3.8}$$

$$H_{\alpha 1} = (T_{Int})_{\alpha 1} + (V_{Int})_{\alpha 1} \tag{3.9}$$

$$H_{\alpha 2} = (T_{Int})_{\alpha 2} + (V_{Int})_{\alpha 2} \tag{3.10}$$

This leads to the external wave functions being the product of four parts:

$$\Psi = \Phi(R)\Xi(r_\alpha)\psi_{\alpha 1}(q_{\alpha 1})\psi_{\alpha 2}(q_{\alpha 2}) \tag{3.11}$$

where:

$$H_O\Phi = \varepsilon\Phi \tag{3.12}$$

$$H_c\Xi = \mathfrak{E}\Xi \tag{3.13}$$

$$H_{\alpha 1}\psi_{\alpha 1} = E_{\alpha 1}\psi_{\alpha 1} \tag{3.14}$$

$$H_{\alpha 2}\psi_{\alpha 2} = E_{\alpha 2}\psi_{\alpha 2} \tag{3.15}$$

The wave functions Φ, Ξ, $\psi_{\alpha 1}$, and $\psi_{\alpha 2}$ describe respectively the centroid motion, the relative motion of $\alpha 1$ and $\alpha 2$, and the internal states of $\alpha 1$ and $\alpha 2$, with the appropriate associated energies. For simplicity, the centroid motion can be neglected and ε set to zero; thus, the energy in a given channel is given by $\mathfrak{E} + E_{\alpha 1} + E_{\alpha 2}$.

The wave function of relative motion, Ξ, can be decomposed into a radial and an angular component of the form:

$$\Xi \sim r_\alpha^{-1} u_{\alpha s l}(r_\alpha)(i^l Y_m^l(\Omega_\alpha)) \tag{3.16}$$

The radial functions, $u_{\alpha s l}(r_a)$ are then solutions of the radial Schrödinger equation:

$$\left[\frac{d^2}{dr_\alpha^2} - \frac{l(l+1)}{r_\alpha^2} - \frac{2M_\alpha}{\hbar^2}(V_{\alpha s l} - E_\alpha)\right] u_{\alpha s l}(r_\alpha) = 0 \tag{3.17}$$

Assuming that the potential is restricted to the Coulomb potential this can be rewritten in the form:

$$u''_{\alpha l}(\rho_\alpha) - \left[l(l+1)\rho_\alpha^{-2} + 2\eta_\alpha\rho_\alpha^{-1} \pm 1\right] u_{\alpha l}(\rho_\alpha) = 0 \tag{3.18}$$

The lower sign corresponds to positive energy channels and the upper corresponds to negative energy channels.

For positive energy channels the two solutions correspond to incoming (I^+) and

outgoing (O^+) waves. The superscripts (+) denote positive energy channels. These solutions are complex conjugates of each other and can be written in the form:

$$I_c^+ = (G_c - iF_c)e^{i\omega_c} \tag{3.19}$$

$$O_c^+ = (G_c + iF_c)e^{-i\omega_c} \tag{3.20}$$

F_c and G_c are the regular and irregular Coulomb functions respectively.

For negative-energy channels, only the O-type solution (O^-) exists and it is the real Whittaker function.

It is appropriate at this point to define a number of functions important in **R**-Matrix analysis. The logarithmic derivative of the O type wave function is designated as:

$$L_c = (\rho_c O'_c/O_c)_{r_c = a_c} = S_c + iP_c \tag{3.21}$$

which gives:

$$S_c^+ = \left[\rho_c(F_c F''_c + G_c G'_c)/(F_c^2 + G_c^2)\right]_{r_c = a_c} \tag{3.22}$$

$$P_c^+ = \left[\rho_c/(F_c^2 + G_c^2)\right]_{r_c = a_c} \tag{3.23}$$

$$S_c^- = \left[\rho_c W'_c/W_c\right]_{r_c = a_c} \tag{3.24}$$

$$P_c^- = 0 \tag{3.25}$$

The P functions are referred to as the penetration factors and the S functions as the shift factors. (W_c is the real Whittaker function)

In the internal region the total wave function is composed of wave functions of definite J and M which are eigenfunctions of the internal Hamiltonian. These wave functions can be expanded, in the internal region, in terms of a complete set of orthonormal wavefunctions $X_{\lambda JM}$ which are solutions of the Schrödinger equation with real eigenenergies $E_{\lambda J}$.

Using the **R**-Matrix formalism involves matching the internal and external wave functions on the channel surface $\mathcal{S}$. For this purpose two quantities are introduced:

$$V_c = \left(\frac{\hbar^2}{2M_c a_c}\right)^{\frac{1}{2}} u_c(a_c) \tag{3.26}$$

called the *value quantity*, and

$$D_c = \left(\frac{a_c \hbar^2}{2M_c}\right)^{\frac{1}{2}} \left(\frac{du_c}{dr_c}\right)_{r_c = a_c} \tag{3.27}$$

called the *derivative quantity*. It should be noted that:

$$\frac{D_c}{V_c} = B_c \tag{3.28}$$

which are the energy independent boundary conditions.

Two other relations that are needed are:

$$\Delta_{\lambda\mu c} = -(S_c - B_c)\gamma_{\lambda c}\gamma_{\mu c} \tag{3.29}$$

$$\Gamma_\lambda = iP_\lambda \gamma_\lambda \tag{3.30}$$

From these relations Lane and Thomas [La58] derive the fundamental **R**-Matrix relation:

$$V_{c'} = \sum_c R_{cc'} D_c^0 \quad \text{or} \quad \mathbf{V} = \mathbf{RD}^0 \tag{3.31}$$

and the one level approximation:

$$\sigma_{ab} = \frac{\pi g_J}{k_a^2} \cdot \frac{\Gamma_{1,1a}\Gamma_{1,1b}}{(E_1 + \Delta_{1,1} - E)^2 + (\frac{1}{2}\Gamma_{1,1})^2} \tag{3.32}$$

Barker *et al*. [Ba67, Ba68] made a generalization to the one level approximation to allow for the interference of multiple levels:

$$\sigma_\alpha \sim P_l \sum_x \left| \frac{\sum_{\lambda=1}^{q} \left\{ G_{\lambda x}^{1/2} \gamma_{\lambda l} / (E_{\lambda l} - E) \right\}}{1 - (S_l - B_l + iP_l) \sum_{\lambda=1}^{q} \left\{ \gamma_{\lambda l}^2 / (E_{\lambda l} - E) \right\}} \right|^2 \tag{3.33}$$

Later Barker [Ba69] further developed the theory to include β-decay. This leads to a general spectrum of beta-delayed alpha particles as:

$$W(E) = C^2 f_\beta P_l \frac{\left| \sum_{\lambda=1}^{q} \left\{ g_{\lambda F} \gamma_\lambda / (E_{\lambda l} - E) \right\} \right|^2 + \left| \sum_{\lambda=1}^{q} \left\{ g_{\lambda G} \gamma_\lambda / (E_{\lambda l} - E) \right\} \right|^2}{\left| 1 - (S_l - B_l + iP_l) \sum_{\lambda=1}^{q} \left\{ \gamma_{\lambda l}^2 / (E_{\lambda l} - E) \right\} \right|^2} \tag{3.34}$$

In this case the feeding factor $G_{\lambda x}$ is replaced by two terms $g^2_{\lambda x} f_\beta$, where x = F or G for Fermi and Gamow-Teller transitions. The f_β is the integrated Fermi function. In the case of the beta-delayed alpha-particle emission of ^{16}N there is no Fermi transition ($\Delta J = \pm 1$), since such a transition leads to the parity violating alpha-decay of a 2^- state [Ne74]; thus that term goes to zero. In 1971 Barker further developed this theory and specialized it to the case of ^{16}N [Ba71]. This results in the alpha-particle energy spectrum of:

$$W(E) = f_\beta \sum_{l=1,3} P_l \left(\frac{\left| \sum_{\lambda}^{q_l} \{ A_{\lambda l} / (E_{\lambda l} - E) \} \right|^2}{\left| 1 - (S_l - B_l + iP_l) \sum_{\lambda=1}^{q_l} \left\{ \gamma_{\lambda l}^2 / (E_{\lambda l} - E) \right\} \right|^2} \right) \tag{3.35}$$

Where:

$$A^2_{\lambda l} = \frac{N \cdot Y_{\lambda l} \cdot \gamma^2_{l\alpha} \cdot (1 - \gamma^2_{l\alpha} \cdot \frac{dS}{dE_{E_i}})}{\pi \cdot Y(9.63)} \tag{3.36}$$

Where N is the total number of alpha-particles in the spectrum and $Y_{\lambda l}$ are the measured beta-decay branching ratios. Thus the reduced alpha widths depend upon the fitted values of the $A_{\lambda l}$ parameters. S_{E1} is parametrized in **R**-Matrix theory as:

$$S_{E1} = E \cdot e^{2\pi\eta} \cdot \frac{6\pi}{k_\alpha^2} P_l \left| \frac{\sum_{\lambda}^{q_l} \left[\frac{\gamma_{i\alpha} \Gamma_{i\gamma}^{1/2}}{(E_i - E)} \right]}{1 - (S_l - B_l + iP_l) \sum_{\lambda=1}^{q_l} \left\{ \gamma_{\lambda l}^2 / (E_{\lambda l} - E) \right\}} \right|^2 \tag{3.37}$$

which depends upon the reduced alpha widths.

In a full analysis to determine $S_{E1}(300)$, the beta-delayed alpha-particle energy spectrum is fit concurrently with direct alpha-particle capture data and elastic scattering data of alpha-particles on ^{12}C. One major unknown at present is the sign of the interference of the tails of the two 1^- (-40 keV and 2.35 MeV) states. A destructive interference will result in a small S-factor. That the beta decay of ^{16}N cannot, in principle, determine the sign of the interference was demonstrated by Zhao *et al.* in her analysis at Seattle [Zh95].

Originally, the value of the S-factor was thought to be well determined by the relative size of the secondary maximum [Hu91, Ji90, Ba88] (see fig 1.1), with analysis giving values for the S-factor between 80 to 95 keVb [Zh93, Az94, Ha96]. However, recent preliminary reanalyses of the original Yale-UConn and of the TRIUMF data sets by G.M. Hale [Ha96] as presented at the Fourth International Conference on Nuclei in the Cosmos (NIC '96) have found solutions consistent with low values of the S-factor around 10-20 keVb, with only a small contribution from the subthreshold state. G.M. Hale also suggests that the secondary maximum may indeed be due to a shadow pole of the primary maximum at 2.75 MeV rather than an interference effect at all [Ha96]. Thus, Dr. Hale concludes that the ^{16}N data is incapable of ruling out a small S-factor solution. An important caveat is that Hale's results must be considered as preliminary since considerable work remains to be done in his analysis [Ha96]; however, he reports that he does not expect his results on the reduced alpha-particle width to change by much more than 20% [Ha96]. Until this theoretical disagreement is resolved, the beta-delayed alpha-particle spectra cannot be considered to constrain the S-factor to within the desired accuracy.

IV: Experimental Procedures

The experiments were performed using a 150-250 pnA 70 MeV ^{15}N beam from the Yale tandem van de Graff accelerator and a ^{2}H gas target to produce ^{16}N, which escaped from the gas target and was stopped in aluminum catcher foils. These foils were then rotated into a counting area to detect the decays of the ^{16}N.

This experiment is an improvement of the original Yale-UConn experiment [Zh93a, Zh93b]. In the original experiment a low energy ^{2}H beam and a solid Ti^{15}N target were used. Because of the low recoil energy and lack of kinematic focussing of the resulting ^{16}N, it was necessary for the target acted as the catcher foil as well. This limited the available yield, as the thickness of the catcher foil determines the energy resolution of the experiment.

In the experiment reported on here, the kinematics were reversed. A heavy ^{15}N beam and a light $^{2}H_2$ gas target were used. The produced ^{16}N was kinematically focussed into a forward cone of ~ 7°.

A: Overview

In this experiment the beta-delayed alpha-particle emission from the ground state of ^{16}N was studied. The ^{16}N was produced via the $^{2}H(^{15}N,^{16}N)^{1}H$ reaction. The forward scattered ^{16}N is produced primarily in two excited states—a 1^- state at 0.397 MeV with a 4.5 ps lifetime and a 3^- state at 0.121 MeV with a 5.3 μs lifetime. Additionally a few percent of the ^{16}N are produced in a short lived 3^- state at 0.297 MeV and in the 2^- ground state [Bo72]. After the ^{16}N is produced, these excited states are allowed to decay via electromagnetic transitions. The time period between the cessation of production of ^{16}N and the onset of data acquisition is approximately 3 s—more than 5×10^5 lifetimes of the longest lived excited state in ^{16}N.

The ^{16}N comes out of the target (described below) and is implanted in a thin aluminum catcher foil (described below) that is tilted to 7° with respect to the beam, by which we increase the effective thickness of the foil for stopping the ^{16}N by about a factor of 8. The

catcher foils are located at the ends of a ~1 m long arm which rotates about its center. After approximately one lifetime of ^{16}N, the arm is rotated 180°. The rotation takes three seconds (during which the excited states in ^{16}N all decay via electromagnetic transitions), and the catcher foil is placed between two detector arrays (discussed below). The ^{16}N beta-decays into excited ^{16}O which then promptly alpha-decays (~10^{-20} s), and the beta-particles and alpha-particles are detected in the separate arrays in coincidence. The timing between the two arrays is used to eliminate background in the alpha-array to produce the final spectrum.

B: ^{15}N Beam

Nitrogen is a fairly difficult beam to produce in a tandem Van de Graff accelerator, since the negative nitrogen ion is not bound and a tandem accelerator requires a beam of negative ions from its ion source. At the ESTU accelerator the ion source used was an 860 Cesium sputter source. It works by sputtering material off a copper cone with a beam of ionized Cesium producing negative ions via charge exchange reactions of the sputtered surfaces. The material one wishes to accelerate is placed in the center of the copper cone, which is attached to a cathode kept at high voltage relative to the rest of the source. A gas cathode was used for this experiment. In the gas cathode a small (<1mm diameter) hole is drilled through the cone and the cathode, allowing gas into the source. The procedure followed was originally developed to produce a magnesium beam. Thus the cone is filled with magnesium metal, which reacts with the Cesium and ammonia gas to give NH^- and NH_2^- ions.

The Yale ESTU tandem Van de Graff accelerator was used to accelerate the negative NH_x^- ions, with the terminal voltage at just under 12 MV. A tandem Van de Graff accelerator works by accelerating a negative ion beam towards its positive terminal; within the terminal the beam passes through a thin Carbon foil, which strips off electrons with orbital velocities comparable to or less than the ion's velocity. This produces a positive beam which is then accelerated away from the positive terminal.

This high energy positive beam (in this case $^{15}N^{5+}$) is deflected through 90° by a precision analyzer magnet producing a pure beam. The magnetic field for the analyzer magnet is set to the desired energy and charge state for the beam, and controls the accelerator terminal voltage via a feedback circuit.

C: Deuterium Target

One key goal of this experiment was to maximize the amount of ^{16}N caught by the catcher foils, while retaining a useful energy resolution. In the original Yale-UConn experiment [Zh93a], the target and backing were the catcher foil. Since a thick target is needed for significant yield yet a thin catcher foil is needed for energy resolution, a compromise was necessary. In this experiment the target was separated from the catcher foil in an attempt to improve both statistics and resolution.

At first, target designs involving metal deuteride were discussed. There were several problems associated with these target designs. Only a small proportion of their mass is composed of deuterium, and they are fairly sensitive to temperature and partial hydrogen pressure. At high temperatures and low hydrogen partial pressures metal deuterides dissociate, releasing deuterium gas. The metals which are useful tend to have high atomic numbers (high Z) creating the problem of ^{16}N multiple scattering. As the targets were intended to be used in a vacuum and to have about 70 watts deposited into them, we used a gas target [Th49, Hu52, Sp61, Le67, Sh67].

This gas target is a copper cylinder about 7.5 cm long and 1.9 cm in diameter with 0.3 cm walls. It was cooled with an alcohol cooling system to -40°C. Thin beryllium pressure foils (25 μm) were attached with Araldite AW 106/HV 953 epoxy from CIBA-GEIGY, which is good to liquid nitrogen temperatures [Zh93e] to the ends of the cylinder. To reduce plural scattering, beryllium was chosen for the pressure windows as it has a low Z (Z=4) and serves as a secondary target material. The gas target was designed to get as close to the catcher foil as possible with its exit window 7.5 cm from the catcher foil. The

target was kept filled with 1200 to 1300 torr of D_2 gas during the experiment with the gas slowly diffusing out through the pressure foils. The gas target was refilled to 1300 torr when its pressure had dropped to 1200 torr. The time interval between fillings varied from about a day to a few hours depending on the amount of ^{15}N beam on target and the condition of the pressure windows. After a few weeks of running it became necessary to replace the rear pressure foil.

D: Vacuum System

In low energy nuclear physics it is necessary for all operations involving charged particles to be done under vacuum. This experiment took place within a 1 m x 1 m x 17 cm aluminum chamber with 3.8 cm thick walls and its side chambers (shown schematically in fig 4.1a, a picture of the chamber shown in fig 4.1b). Off the end of the large chamber is a smaller side chamber containing the detector arrays. The system was typically at ~10^{-6} torr. This chamber was originally designed and built for the Yale-UConn('93) experiment of Zhao *et al*. In the original design, the detector arrays were in the forward angle resulting in radiation damage to the alpha-array (described below); thus, we rotated and flipped the chamber from the position shown in fig 4.1a.

E: Catcher Foils

The catcher foils are critical in this experiment as their thickness determines the energy resolution of the experiment. The catcher foil was tilted at 7° with respect to the ^{15}N beam axis so as to maximize the collection of ^{16}N nuclei while allowing the use of a thin foil. The ^{16}N emerge from the target with a broad energy distribution (of order 7 MeV) of which we collect the lowest 1 MeV portion.

The foils were attached to aluminum catcher frames with 5-minute epoxy. The open area of the catcher frames was about 5cm x 20cm. Inside the chamber (see fig 4.1a) a tantalum shield was positioned to block ^{16}N from hitting the catcher foil frame. When the

Experimental Setup

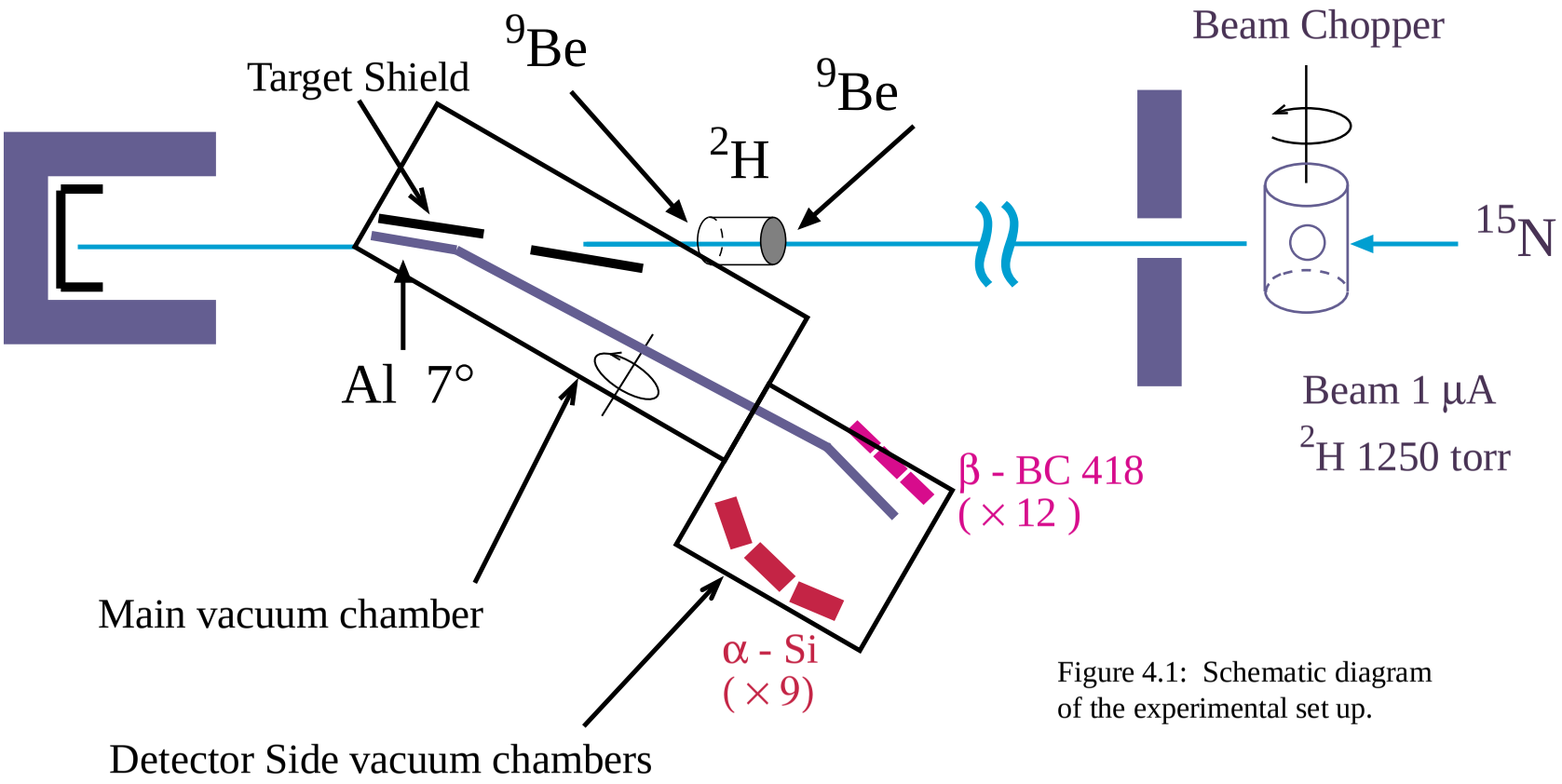

Figure 4.1: Schematic diagram of the experimental set up.

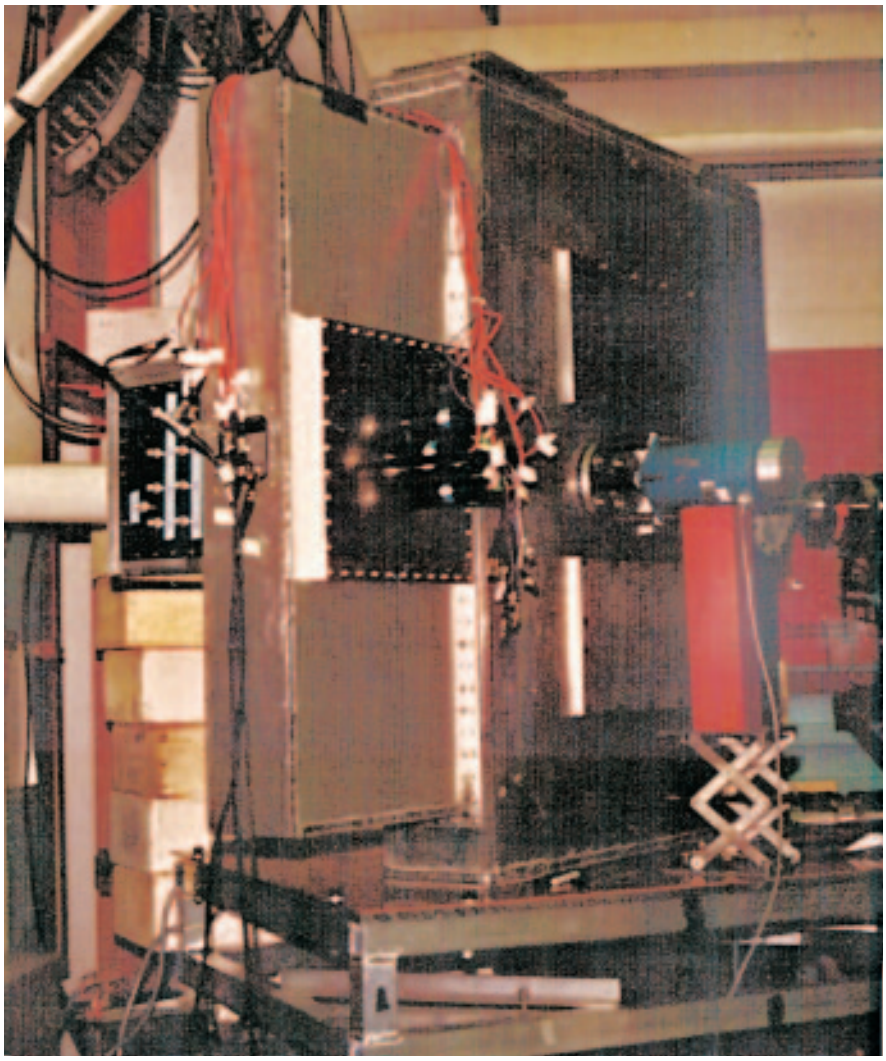

Fig 4.1b: Photograph of the main vacuum chamber in its original orientation with the detector side chamber facing the camera. The blue motor on the right operates the rotating arm. On the far left side of the chamber one can see part of the side chamber which holds the alpha array. The phototubes of the beta array are visible near the center of the picture. In the final experiments, the chamber was flipped and rotated and the detector arrays were reversed in position..

chamber is under vacuum, the shield is less than 1 mm from the frame. In another experiment, to measure the branching ratio of the first forbidden rank one beta decay of ^{20}F, using most of the same apparatus, the shield was tested under significantly more stringent conditions than necessary for this experiment [Wi96]. The energy thickness of the foils for 3.18 MeV alpha-particles was directly measured *in situ* using a ^{148}Gd alpha-particle source to have an effective thickness of190 ± 5 $\mu g/cm^2$.

F: Alignment

Very precise alignment of each part of the system is necessary for the ^{16}N to be stopped in the catcher foils and not elsewhere, where ^{16}N would be a source of background..

Because of the large area of the sides of the vacuum chamber containing the rotating arm (about 1m x 1m), significant flexing occurs during evacuation. The effect of this flexing is further magnified by the acute angles to the beam at which the catcher foil (7°) and the chamber itself (30°) lie and due to the fact that the arm axis was necessarily attached to the approximate center of the chamber wall. It was not possible to brace the chamber as any internal bracing would have prevented rotation of the arm. External stiffening of the 3.8 cm thick aluminum walls was impractical due to the locations of necessary access ports on the chamber sides and the difficulties of welding such supports to the aluminum of the chamber.

It was necessary to align each element of the system while the entire system was under vacuum. The alignment system was comprised of one set of slits located several meters upbeam, one set of slits located about a meter upbeam, two tantalum collimators, the gas target, the tantalum shield, and the catcher foil frames. The upstream slits were only used in steering the beam to the beamdump. After that was accomplished, the downstream slits and the two collimators kept the beam in a straight line through the target and foil frames. While the slits and, to a lesser extent, the collimators could be adjusted from outside the chamber, the foil frames and shield had to be adjusted with the chamber open.

G: Arm Rotation

The experiment was run in 21 second cycles. The first ten seconds of each cycle was the collection period. During this time, the ^{15}N beam impinged on the target, producing ^{16}N, which was collected on the catcher foil. At the end of this collection time, a tantalum beam chopper blocked the beam far upstream, and the arm carrying the catcher foil was rotated 180°. The rotation took a little less than three seconds. Three seconds after the rotation began, the data acquisition system was activated. Data were collected for eight seconds, after which the cycle was repeated. In order to protect the catcher foil frames from the beam, the position of the beam chopper was read back into the control room and the arm was not put into rotation until the beam chopper was fully in place. Due to ^{8}Li's shorter lifetime, this cycle was modified—the collection and counting times were reduced to one second each—for the Li calibration runs described later. The arm rotation time remained three seconds, as this was the fastest it could safely be rotated. Fig. 4.2 shows explicitly the time structure of ^{16}N and ^{8}Li cycles.

H: The Detectors

The principal detectors in this experiment were nine Silicon Surface Barrier (SSB) detectors in a square array (the alpha array, see fig 4.3a). Each detector has an active area of 450mm^2 and a 50 μm thick active region to minimize deposition of energy from beta-particles in the alpha array. Canberra 2003B preamps which had been modified to match the detectors high capacitance were used. The detectors had an energy resolution of ~55 keV. The array was positioned 70 mm from the catcher foil. SSB detectors are based upon a reverse biased diode. An energetic charged particle deposits energy in the silicon by exciting electrons into the conduction band, producing electrons and associated holes, which are collected and produce an electronic pulse.

One crucial improvement over the previous Yale-UConn experiment was the positioning of the alpha array. In the previous experiment the alpha array was located at a

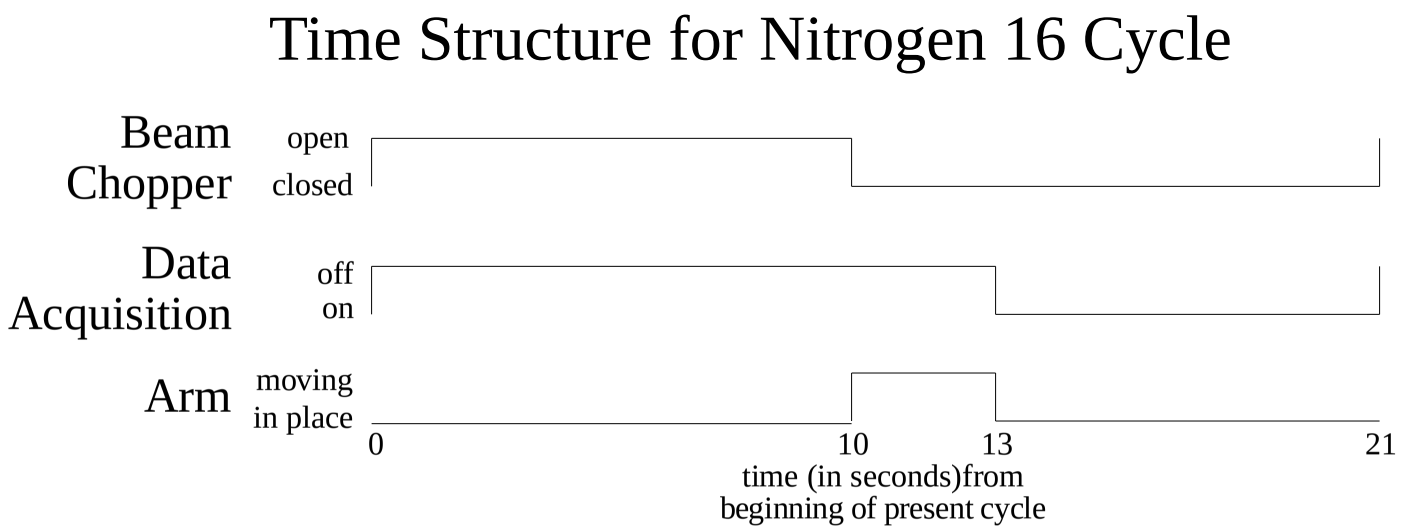

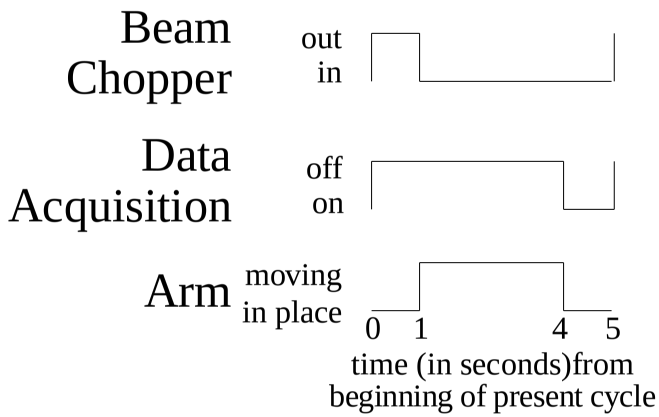

Figure 4.2: Time structure of the ^{16}N experiment and the ^{8}Li calibration runs (described in section IV.K). These diagrams show the three phases of each cycle. First the radionuclide is collected, then the arm is rotated, and finally the data acquisition phase takes place.

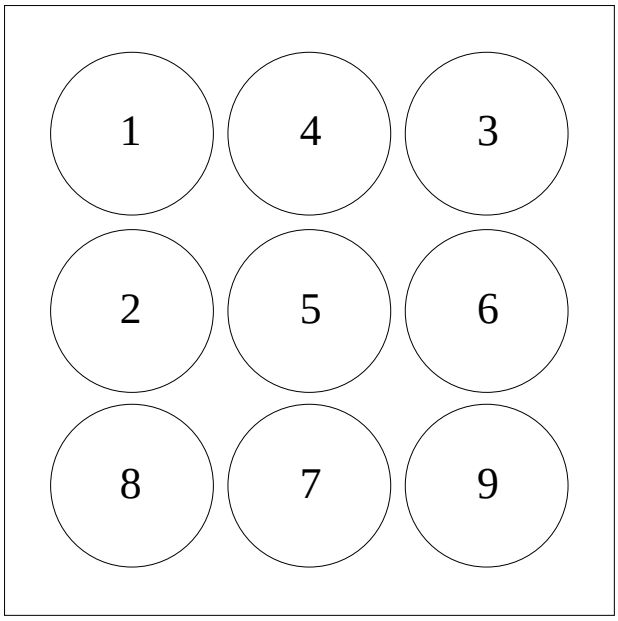

Figure 4.3a: layout of the Alpha-Array.

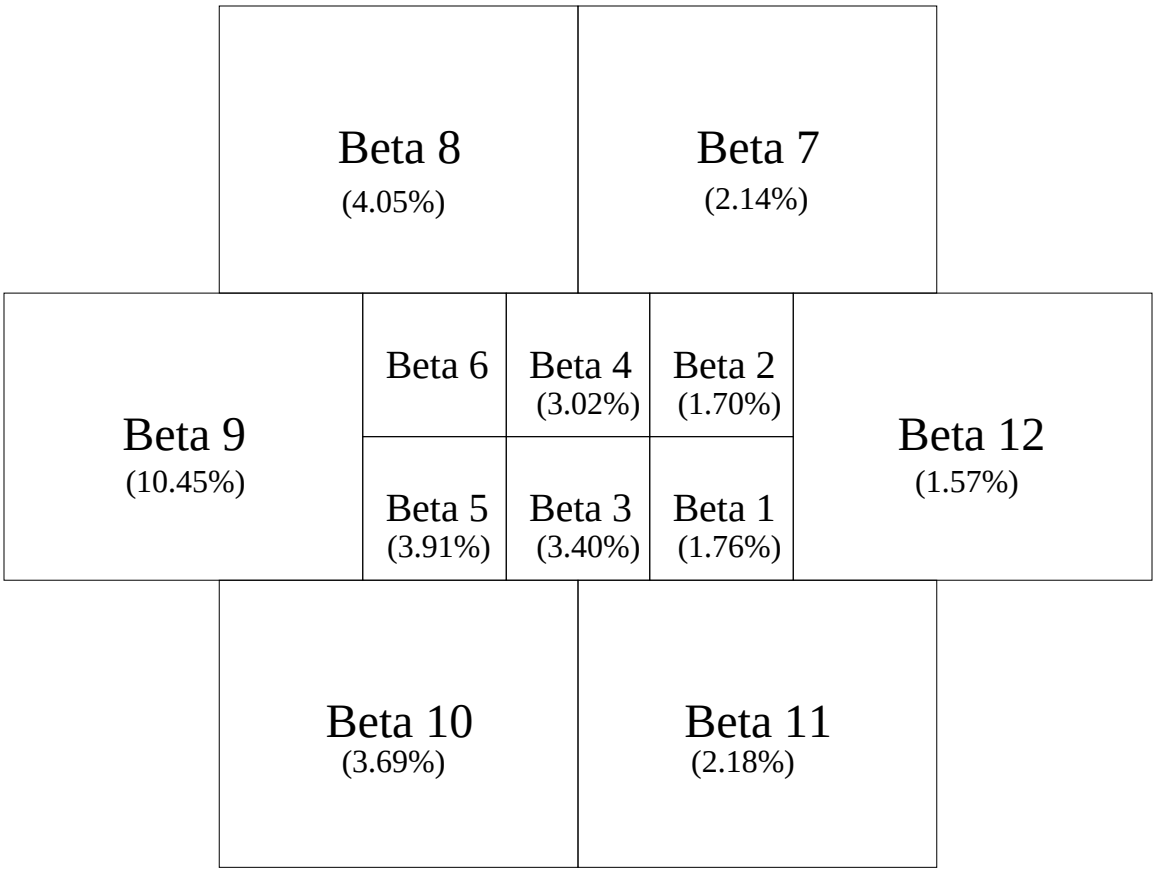

Figure 4.3b: Layout of the Beta-Array. Detector Beta 6 was not operational during the final experimental runs. The on-line estimated absolute efficiency of each detector is given in parenthesis.

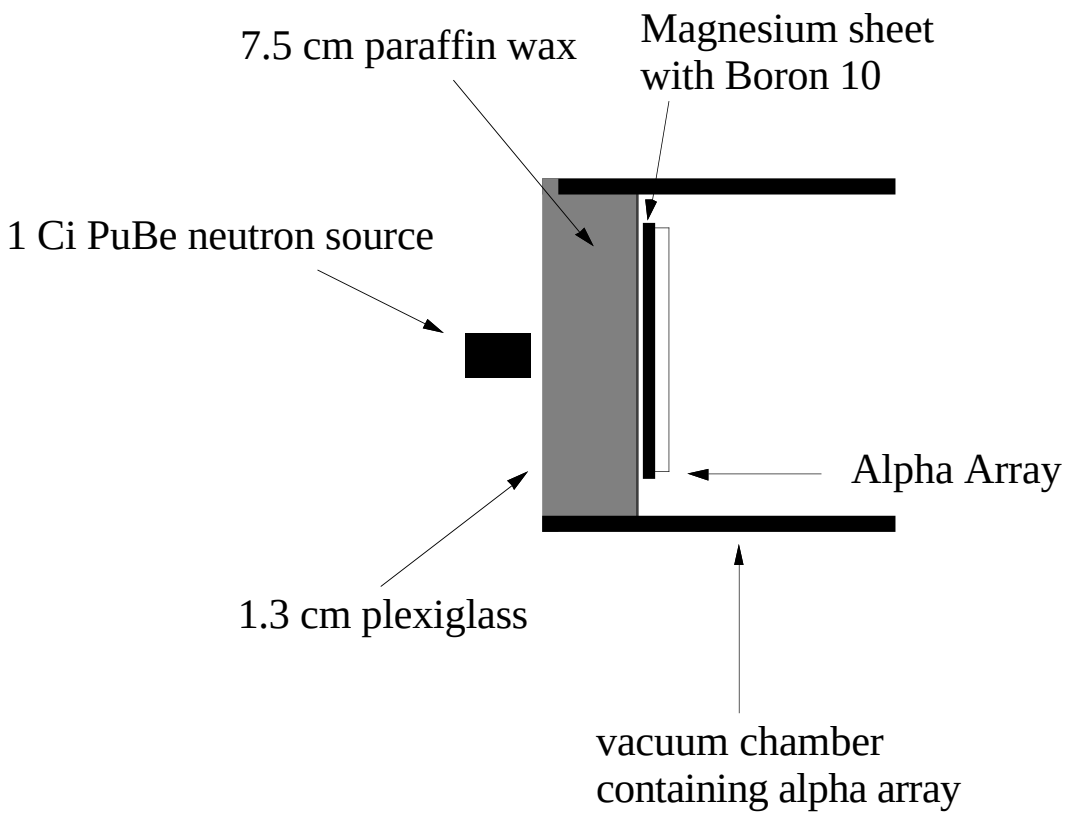

Figure 4.3c: Layout during $^{10}B(n,\alpha)^{7}Li$ calibration runs.

forward angle with respect to the beam and suffered considerable radiation damage from neutrons emitted in forward angles. This was detected in the form of increased leakage currents, making it necessary to cool the alpha array to -40°C using an alcohol cooling system. In this experiment, the target chamber was flipped and rotated (compared to the earlier experiment) so that the alpha array could be placed at a backward angle. The leakage currents remained nearly constant over up to four weeks of continuous running under these conditions, and no cooling was necessary.

The secondary set of detectors in this experiment was an array of twelve plastic scintillation detectors (the beta array, see fig 4.3b) made from BC418 plastic scintillator and Hamamatsu H3165 and H3171 photomultipliers. The central six were 2.5 x 2.5 x 0.6 cm; the outer six were 5 x 5 x 0.6 cm. The detectors were optically isolated from one another and were covered by a ~0.02 mm mylar film to prevent the detection of alpha-particles or ^{12}C recoils. During the experiment, the catcher foils were approximately than 0.5 cm from the beta array. The alpha-beta timing resolution at 1.75 MeV, during actual running conditions, was 2.4 nsec, comparable to the previous Yale-UConn experiment and sufficient to separate out background due to beta-gamma coincidences and partial charge collection in the SSB's.

Due to the wall of the vacuum chamber (described above) flexing under atmospheric pressure, during evacuation of the chamber the catcher foil moved towards the beta array and away from the alpha array by approximately 0.5 cm. Due to the reuse and flipping of the original chamber, the ^{16}N on the catcher foils was not well centered with respect to the detector arrays, and thus, beta-9 had a significantly higher count rate than the other detectors in the beta arrays, while alpha-2 had a slightly higher rate than the other detectors in the alpha array. Beta-9 in particular accounted for up to 40% of the usable data collected. A new mounting plate for the beta array was made to minimize this problem, resulting in the ^{16}N on the catcher foil being centered between beta detectors 5 and 6 (see fig. 4.3b). We wished to spread the beta-particle detections amongst the detectors as evenly as possible to

minimize the count rate—and hence random coincidences—in each detector. Fig. 4.1a is a schematic of the experimental setup.

I: Data Acquisition

Data were stored in event by event format onto 8mm video tapes using a Concurrent 3230 computer. The information recorded onto tape for each event included the alpha particle energy as measured by the SSB detectors, the timing difference between the SSB detectors and each of the plastic scintillation detectors, the position of the rotating arm, and a bit pattern showing which SSB had fired, thus creating the timing event. A bit pattern for the beta array was not needed since timing was taken for each beta detector. No energy information was taken from the beta array. Figs 4.4a-f are diagrams of the various electronic subsystems used to take data.

The beam chopper was located in the laboratory's high energy vault containing the accelerator, about 20 meters and two shielded walls away from the target area. A control signal was fed to the beam chopper, and two position sensors fed signals back to the control room. [See fig 4.4a]

In the target room (TRII) there were three sets of independent electronics. The first was the linear electronics associated with the alpha array. The nine SSB's were each connected to Canberra 2003B Preamps. The energy output of each preamp was then fed directly to the control room. The timing output was fed into an Ortec VT120 Fast Preamp and then into a Philips 715 Constant Fraction Discriminator (CFD). A delay time of 14 nsec had been determined in earlier experiments. The two outputs of the CFD were fed into the control room. Coming from the control room, was the output of a precision pulser, which was routed through a linear fan-in/fan-out. These signals were fed into the pulser input of the Canberra preamps for use as energy calibrations. Due to problems with noise from the linear fan-in/fan-out, the alpha array was subdivided into three sections for the pulser calibration runs. [See fig 4.4b]

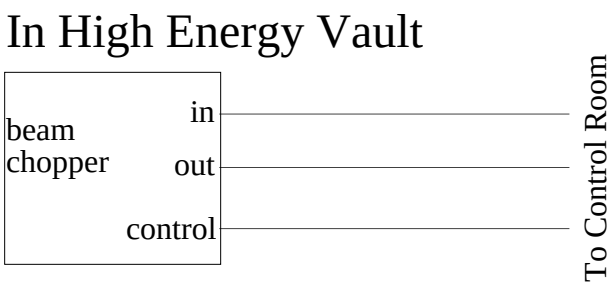

Figure 4.4a: Schematic of electronics located in the High Energy Vault which controlled the beam chopper and relayed back the chopper's condition.

Figure 4.4b: Schematic of electronics located in target room II.

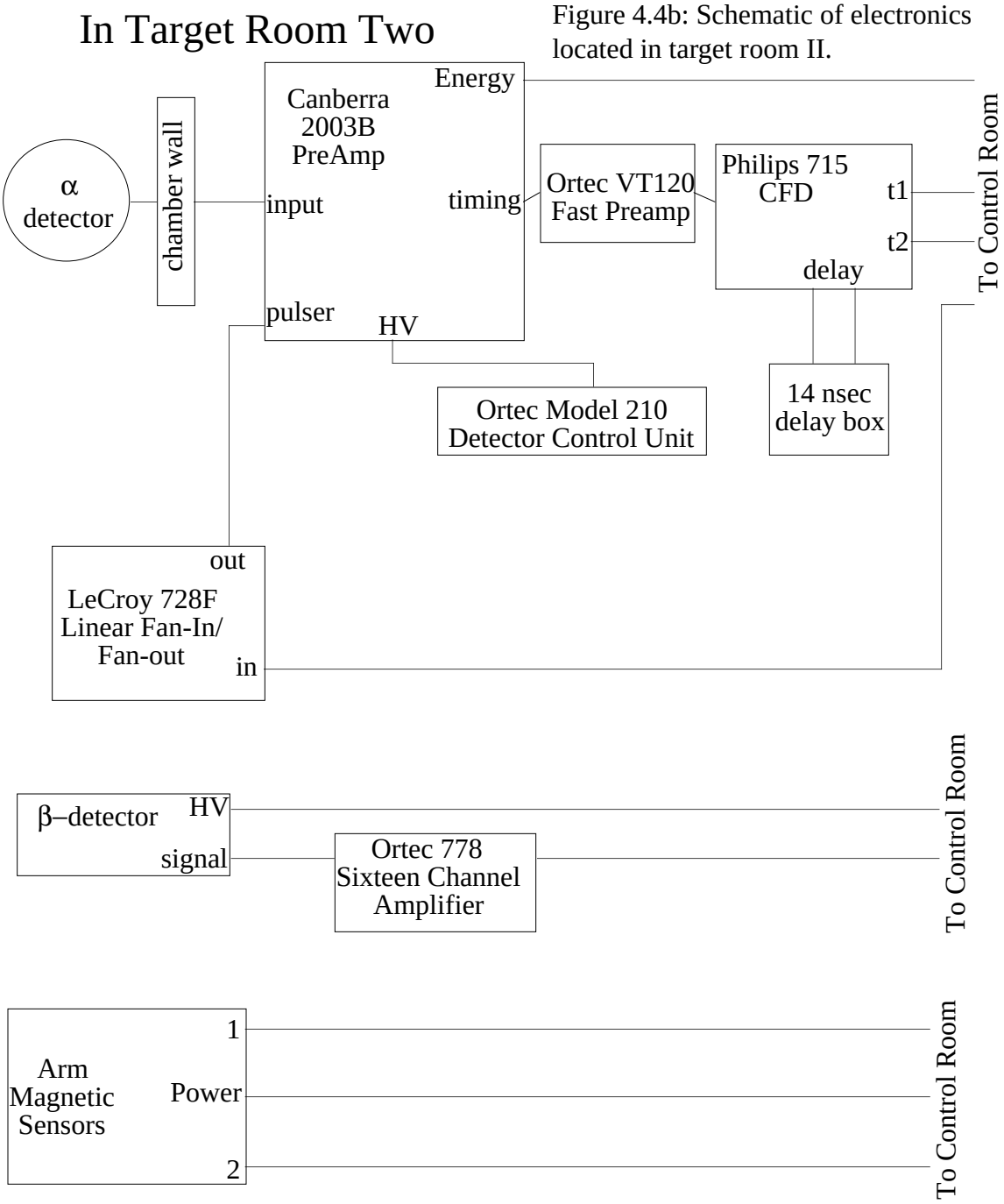

The second set of electronics in TRII was the linear electronics associated with the beta array. Each photomultiplier tube was connected to a high voltage line fed into TRII from the control room. The signal outputs of each of the twelve detectors were amplified by an Ortec 778 Amplifier and then fed into the control room. [See fig 4.4b]

The final set of electronics in TRII was the arm sensor array. This was a set of magnetic sensors which determines the position of the arm. They fed back this information to the control room, from which they received power [See fig 4.4b] and were used by the trigger logic.

In the control room itself there were four sets of electronics. The first of these was the alpha array linear electronics. The energy signals from TRII were fed into Ortec 693 Spectroscopy amplifiers; the outputs of which were fed into Ortec AD811 ADC CAMAC modules. These were gated by the trigger logic electronics. [See fig 4.4c]

The second set was the linear time of flight electronics. Each of the signals from the beta array was fed through a Philips 715 CFD. The outputs were delayed by approximately 63 nsec and were used as stop signals in LeCroy 2228A TDC CAMAC modules. One set of timing signals from the alpha array was fed into a LeCroy 429A Logic Fan-In/Fan-Out in 1 x 16 mode. The output of this module, essentially a logical or of the alpha array, was used as a common start for the TDC's. [See fig 4.4d]

The third set involved the other set of linear alpha array timing outputs and was called alpha timing 1. These outputs were fed into Ortec GG8000 Gate and delay generators. One set of outputs from these GG8000's was logically combined together in a Philips 757 mixed logic Fan-In/Fan-Out set up as a logical or gate. The output of this module went into a LeCroy 429A Logic Fan-In/Fan-Out. This second Fan-In/Fan-Out was used in early experiments and in the ^{20}F experiments [Wi96] to allow easy insertion of gamma-ray detectors into the event electronics, as its output was fed into the trigger logic. [See fig 4.4e]

The other set of outputs from the GG8000's went through another set of GG8000's, whose outputs were fed into a LeCroy 4616 ECL-NIM-ECL Converter. The ECL output of

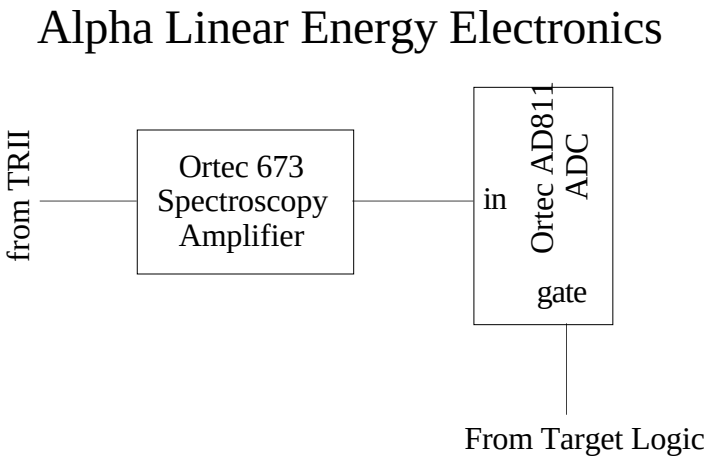

Figure 4.4c: Schematic of the SSB detector energy electronics.

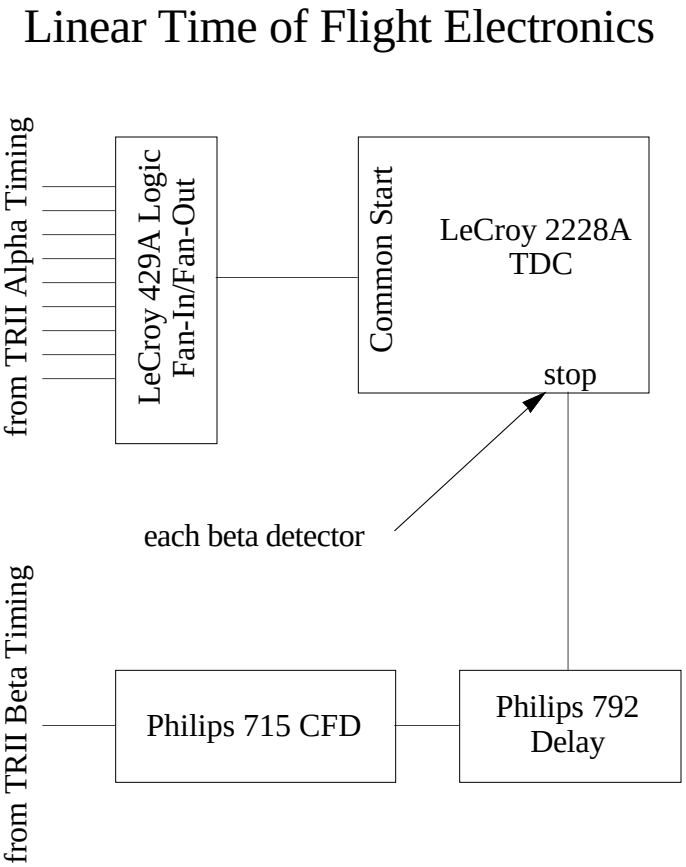

Figure 4.4d: Schematic of the time of flight electronics.

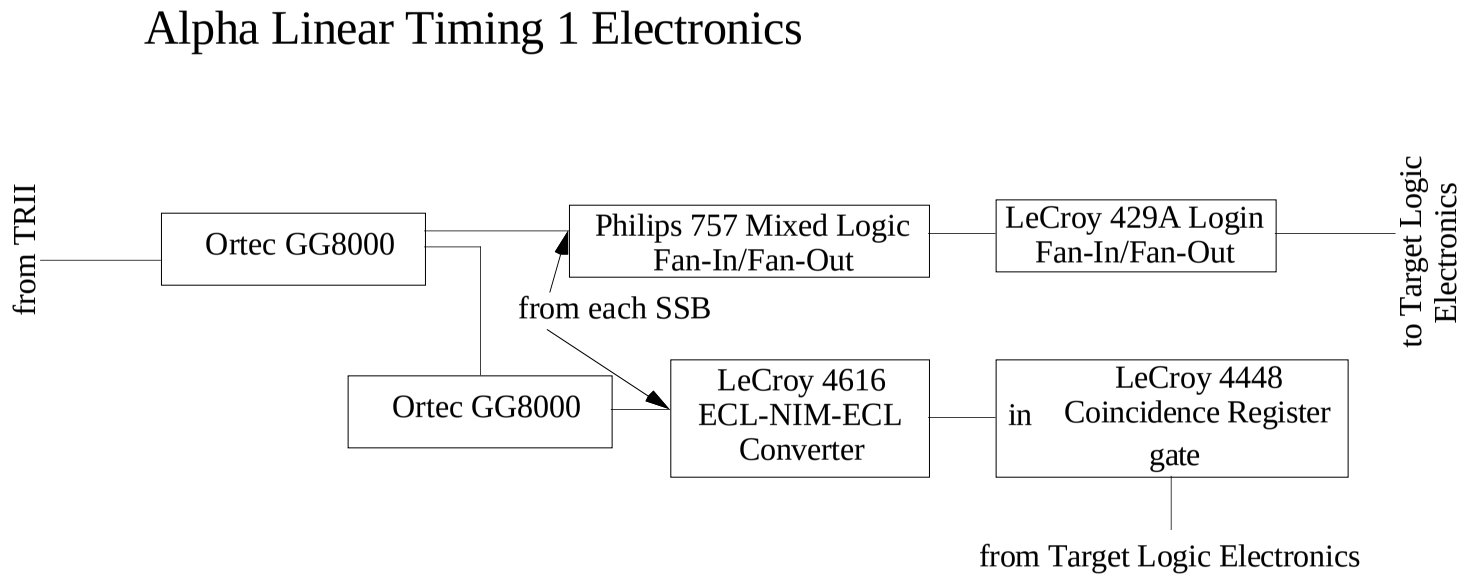

Figure 4.4e: Schematic of Alpha Timing 1 electonics. This set of electronics provides the coincidence register information as well as the timing signal for use by the event logic electronics

this module was the input for a LeCroy 4448 Coincidence Register, which provided the bit pattern, telling which of the SSB's had fired. The 4448 was gated by a signal from the trigger logic.

The final set of electronics provided the trigger logic. The experimental cycle of 21 seconds was controlled by the Barker Cycle Timer (BCT). The BCT is a programmable CAMAC module with two states: open and closed, designed and built specifically for our experimental apparatus. The length of each state is controlled from the Concurrent computer. The CAMAC module also has two TTL outputs, one for each state. The open output was fed into the high energy vault as the control signal for the beam chopper; the closed output was fed into a LeCroy 688AL TTL-NIM level adapter, and then into a Philips 748 Octal Linear Fan-In/Fan-Out. Three outputs of the Philips 748 were used. [See fig 4.4f]

The first was fed into channel 7 of the event handler module and read directly by the event routine software. The second was fed into one input of a LeCroy 465 Coincidence Unit. The third was used to trigger a Philips 794 Gate and Delay Generator. This module was set to a three second delay, long enough for the arm to complete its rotation. The Delay Out output of this module was fed into a second input of the aforementioned LeCroy 465 Coincidence Unit. The third input to the Coincidence Unit came from the alpha timing 1 electronics mentioned earlier.

This coincidence unit is the heart of the trigger logic electronics. The first input produces the requirement that the beam chopper be closed for a valid event to occur. The second input produces the requirement that the arm be finished rotating for a valid event to occur. The third input produces the requirement that an SSB fire for a valid event to occur. The output of the coincidence unit was fed into a LeCroy 429A Logic Fan-In/Fan-Out. The outputs of this LeCroy 429A were then used to strobe the event handler, provide the gate for the Coincidence Register, and trigger an Ortec 416 Gate and Delay generator, which was used to gate the two AD811 ADC's and an Ortec 449 Log/Lin ratemeter.

The position of the arm and the beam chopper were read into the event handler. In

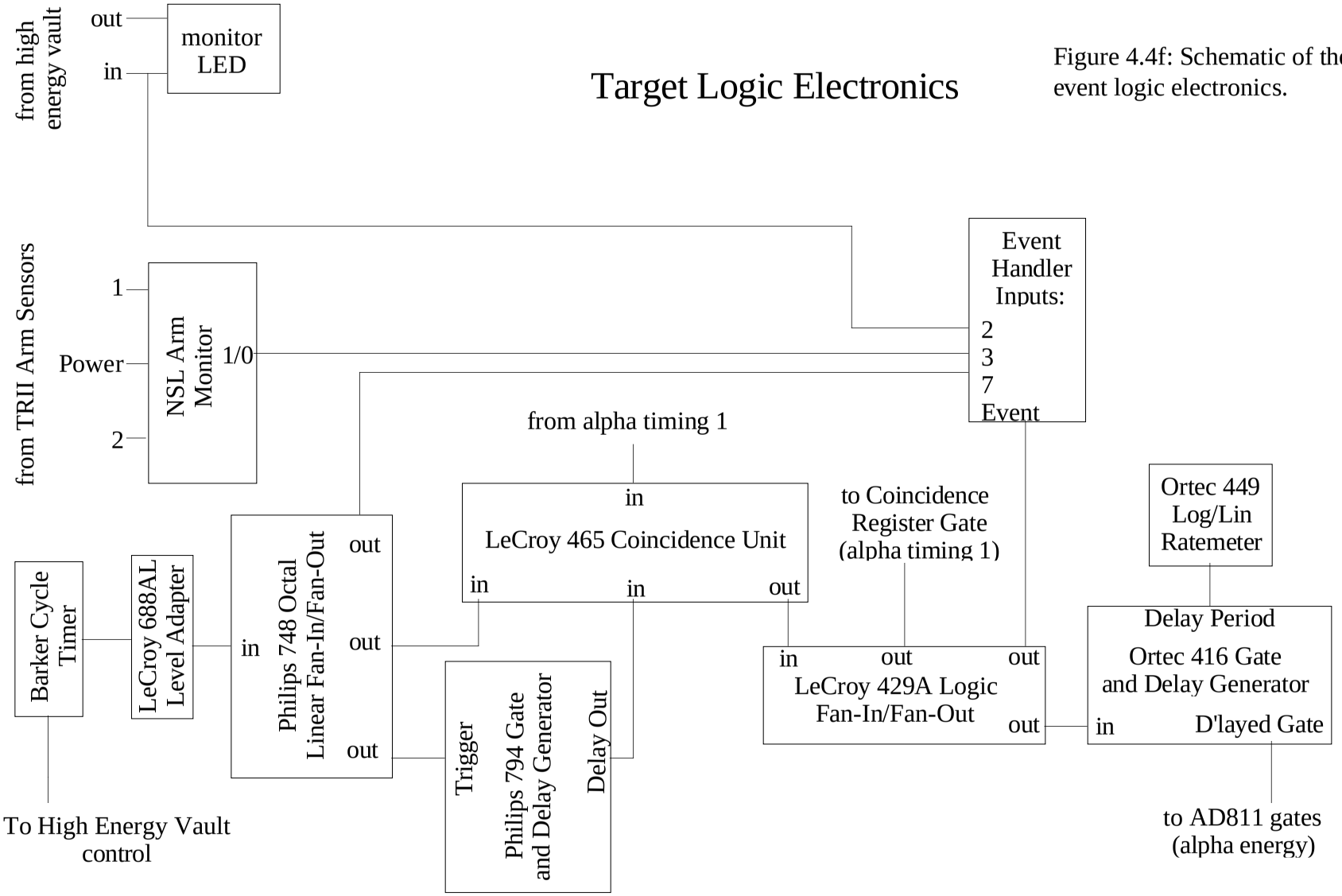

Figure 4.4f: Schematic of the event logic electronics.

software, the data acquisition and arm movement were disabled when the beam chopper was not fully in place, thus providing both hardware and software protection against data acquisition or arm movement while beam was on target.

J: Energy Calibrations

Extensive energy calibrations were performed both to gain-match the alpha array and to check for gain shifts throughout the experiments. The principle alpha-particle emitting sources used were ^{148}Gd (3.1828 MeV), ^{241}Am (5.48 MeV), and ^{208,209}Po (5.116 MeV and 4.8798 MeV respectively). Belatedly, it was discovered that the Polonium source had a sufficiently thick gold coating (~60 keV) to render it useless for direct calibration purposes. Calibration runs using all three sources were performed at the beginning of each of the two week runs, as well as at the end of the first two week run. The Gadolinium source was also run in the middle of the first run. Fig 4.5 shows a typical spectrum obtained.

Each weekend (i.e. at the beginning, end, and middle of each two week run) the alpha detector array was calibrated using the ^{10}B(n,α)^{7}Li reaction. A thin layer of $^{10}B_2O_3$ (~10 μg/cm^2) was deposited on a sheet of magnesium metal. This was placed directly on the alpha array. Approximately 7.5 cm of paraffin wax was placed between the magnesium and the outside of the vacuum chamber, where a 1 Ci PuBe neutron source was placed. As the chamber wall is composed of 1.3 cm thick plexiglass at this point, the neutron source was approximately 9 cm from the ^{10}B (see fig 4.3c). The paraffin thermalized the neutrons which were then absorbed by the ^{10}B emitting ^{7}Li and alpha-particles. The ^{7}Li and alpha-particles formed a spectrum with four peaks. ^{7}Li lines were at 0.841 MeV and 1.014 MeV, and alpha-particle lines were at 1.471 MeV and 1.775 MeV. The ^{7}Li was not used for energy calibration due to the unknown pulse height deficiency for low energy ^{7}Li in SSB.

To produce the $^{10}B_2O_3$ one starts with ortho-boric acid made with isotopically pure ^{10}B. This material is placed within an evaporator bell jar which is then evacuated to a rough vacuum of a few x 10^{-3} Torr. The ortho-boric acid is then heated to undergo the following

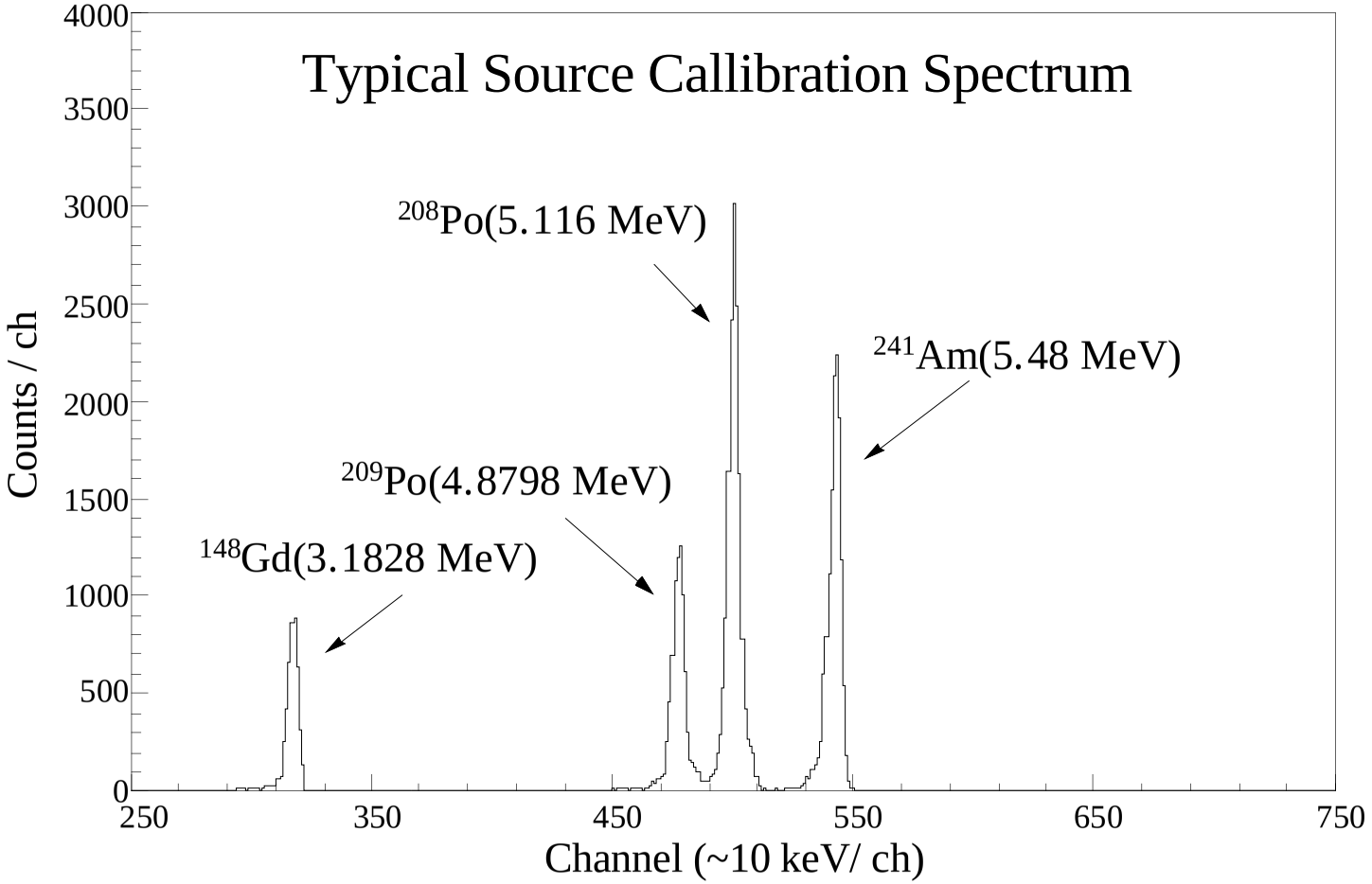

Figure 4.5: Typical Source Spectrum from ^{148}Gd, ^{208,209}Po, and ^{241}Am, exhibiting energy resolution FWHM = 55 keV at 3.2 MeV and signal to background ratio of better than 500:1.

reactions:

$$H_3BO_3 \rightarrow HBO_2 + H_2O \qquad (\sim 170^\circ C)$$

$$2\ HBO_2 \rightarrow B_2O_3 + H_2O \qquad (\sim 236^\circ C)$$

The B_2O_3 is then evaporated onto the magnesium—after pumping the system down to a high vacuum (~10^{-5} Torr)—at ~1600°C. Each stage in the process is marked by changes in the physical state of the material and the pressure indicated in the evaporation system. During the first stage, the translucent white ortho-boric acid becomes opaque white. During the second stage the opaque white HBO_2 becomes opaque black boron oxide. During both transitions large amounts of water vapor were produced, and the pressure often would approach a few hundred millitorr.

Once the boron oxide target was complete, it necessarily was stored in vacuum, and then transported quickly to the target chamber, as it is very hygroscopic. The absorption of water has the effect of changing the thickness of the boron oxide layer, thus affecting the energy resolution of the escaping ^{7}Li and alpha particles. Fig 4.6 shows a typical energy spectrum.

During the timing calibrations, discussed below, an ^{227}Ac source was used. Both this source and the ^{208,209}Po source contaminated the alpha array, providing a series of lines from 4 to 7 MeV which were collected on line with the data. Due to their high energy and timing characteristics these lines do not create any background in the experiment, but they do provide a constant check on the energy calibrations. A typical contaminant spectrum is shown in fig 4.7, and the identified lines are tabulated in Table 4.1.

K: Coincidence Calibration

After the alpha array had been gain matched, it was necessary to match each of the 108 alpha-beta pairs in time. The first step in this process was to make certain that the 100 nsec range of the TDC's included the timing region of interest. To do this an ^{227}Ac source

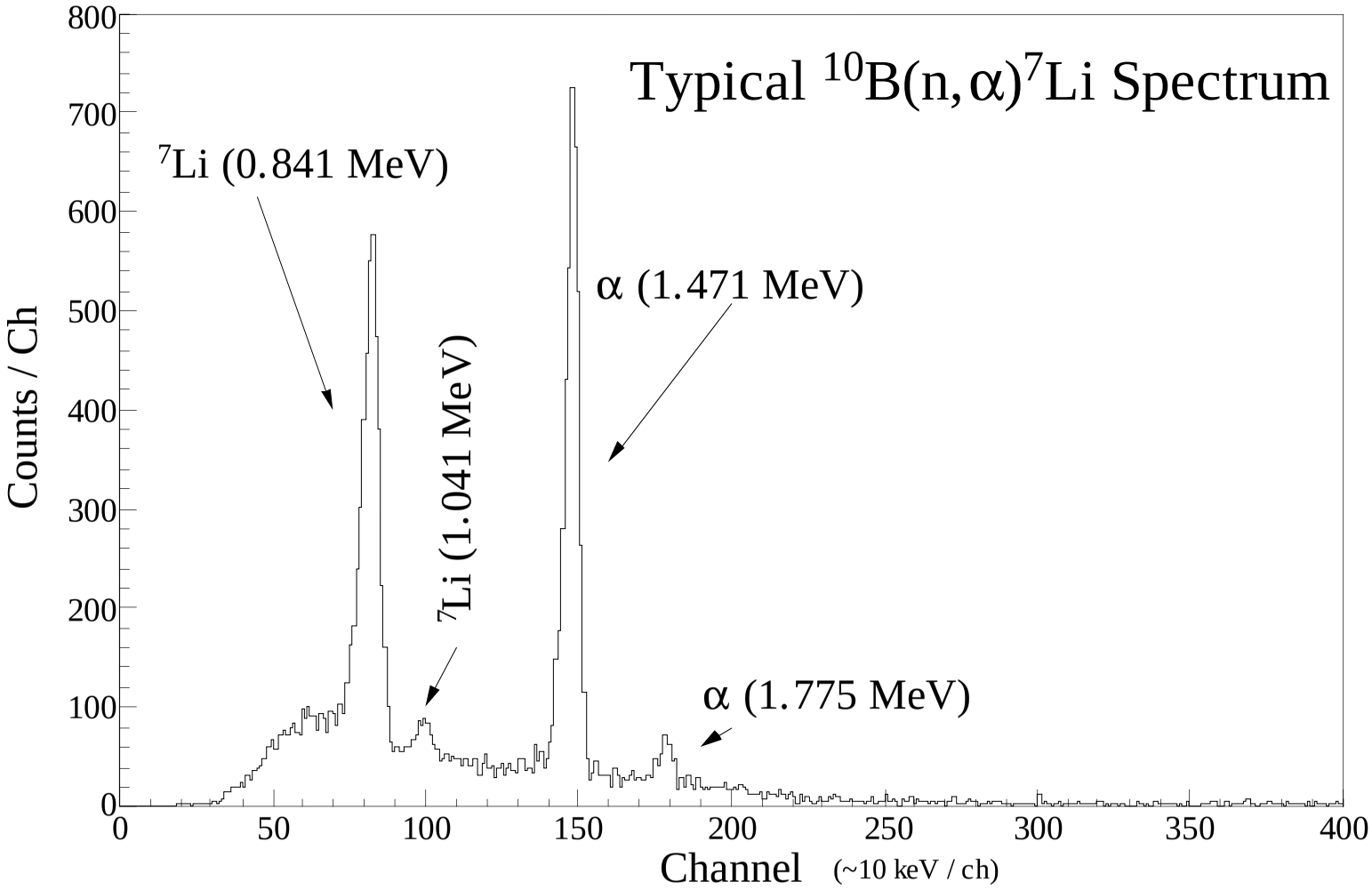

Figure 4.6: Typical Spectrum from the $^{10}B(n,\alpha)^{7}Li$ Reaction used to calibrate our alpha array at low energies exhibiting energy resolution of FWHM = 55 keV at 1.5 MeV.

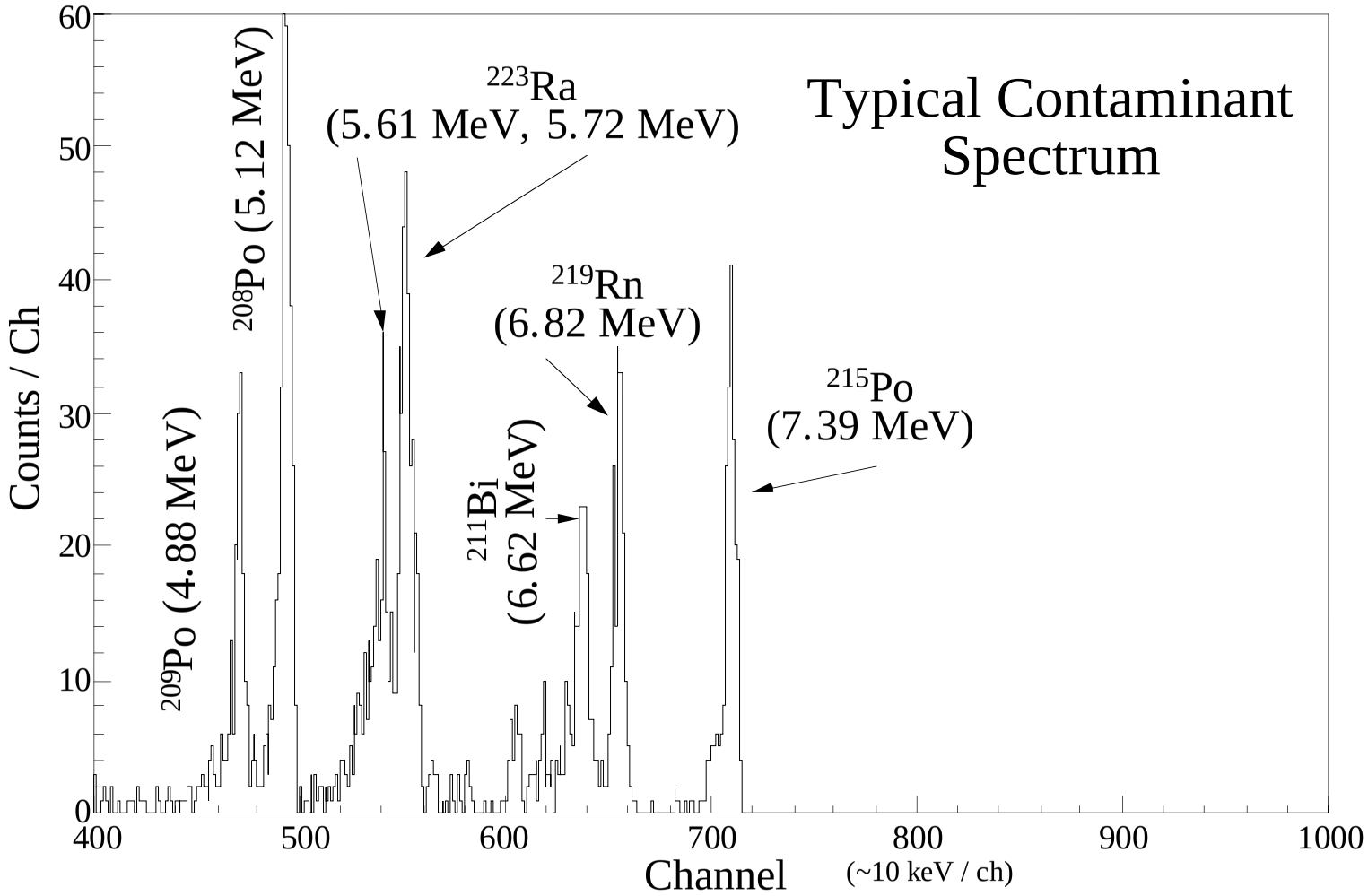

Figure 4.7: Typical Contaminant Spectrum taken concurrently with ^{16}N data over more than a day of running allowing for an online check of the energy calibration. The narrowness of these lines (FWHM = 55 keV at 5 MeV) demonstrates the stability of the energy calibration.

Contaminant	Energy	Halflife	Origin
^{209}Po	4.880 MeV	102(5) years	^{208,209}Po Sorce
^{208}Po	5.116 MeV	2.898(2) years	^{208,209}Po Sorce
^{223}Ra	5.608 MeV	11.43(2) days	^{227}Ac Source
^{223}Ra	5.716 MeV	11.43(2) days	^{227}Ac Source
^{211}Bi	6.623 MeV	2.14(2) minutes	^{227}Ac Source
^{219}Rn	6.819 MeV	3.96(5) seconds	^{227}Ac Source
^{215}Po	7.386 MeV	1.780(4) ms	^{227}Ac Source

Table 4.1: Identified contaminant lines seen during data collection runs. The ^{223}Ra is a daughter of ^{227}Ac. The short lived isotopes seen (halflife < 1 week) are in the decay chain of ^{223}Ra. These lines were used to help calibate the alpha array, as well as to check for any gain shifts occurring during data collection. A typical spectrum can be seen in fig. 4.7.

was used. This source produces beta-delayed alpha-particles of several MeV. Because this source had a tendency to contaminate its surroundings, it had been coated with a very thick layer of gold, making the direct source unusable for energy calibration (see fig 4.8). (However, the contamination was useful as mentioned above.) A typical time spectrum from ^{227}Ac is shown in fig 4.9.

Once the rough timing had set, a 22 MeV ^{7}Li beam was used to produce ^{8}Li via the ^{2}H(^{7}Li,^{8}Li)^{1}H reaction. The ^{8}Li was collected on the same catcher foils used for the ^{16}N. The beta-decay of ^{8}Li proceeds via a broad excited state of ^{8}Be at 2.94 MeV into two alpha-particles. A typical alpha-particle spectrum from this decay is shown in fig 4.10. Because of the short lifetime of ^{8}Li (~844 ms), the experimental cycle was shortened during the Lithium runs by reprogramming the BCT. See fig. 4.2.

The ^{8}Li events were plotted in 108 two-dimensional histograms (one for each alpha-beta detector pair) with time as the x-axis and detected alpha-particle energy as the y-axis (see fig 4.11). Each histogram was then cut into sixteen 100 keV wide slices which were projected on the time axis. The resulting 1728 spectra were each fit using the Oak Ridge data analysis program SAMGR with skewed gaussians, to find the centroid. These values were then fit as a function of energy:

$$Time\ Channel = \frac{A}{\sqrt{Energy}} + B \tag{4.1}$$

where

$$A \sim \sqrt{m_{\alpha}} \cdot d \tag{4.2}$$

where d is the distance from the catcher foil to the alpha-detector and B determines the zero-point.

After these fits were done, as a cross check, the distance from the catcher foil (d in eqn 4.2) was calculated using the fitted values. With the exception of the fits involving beta-6, the distances were all within 30% of the actual distance (~8.3 cm). As the fits for beta-6 were poor, this detector

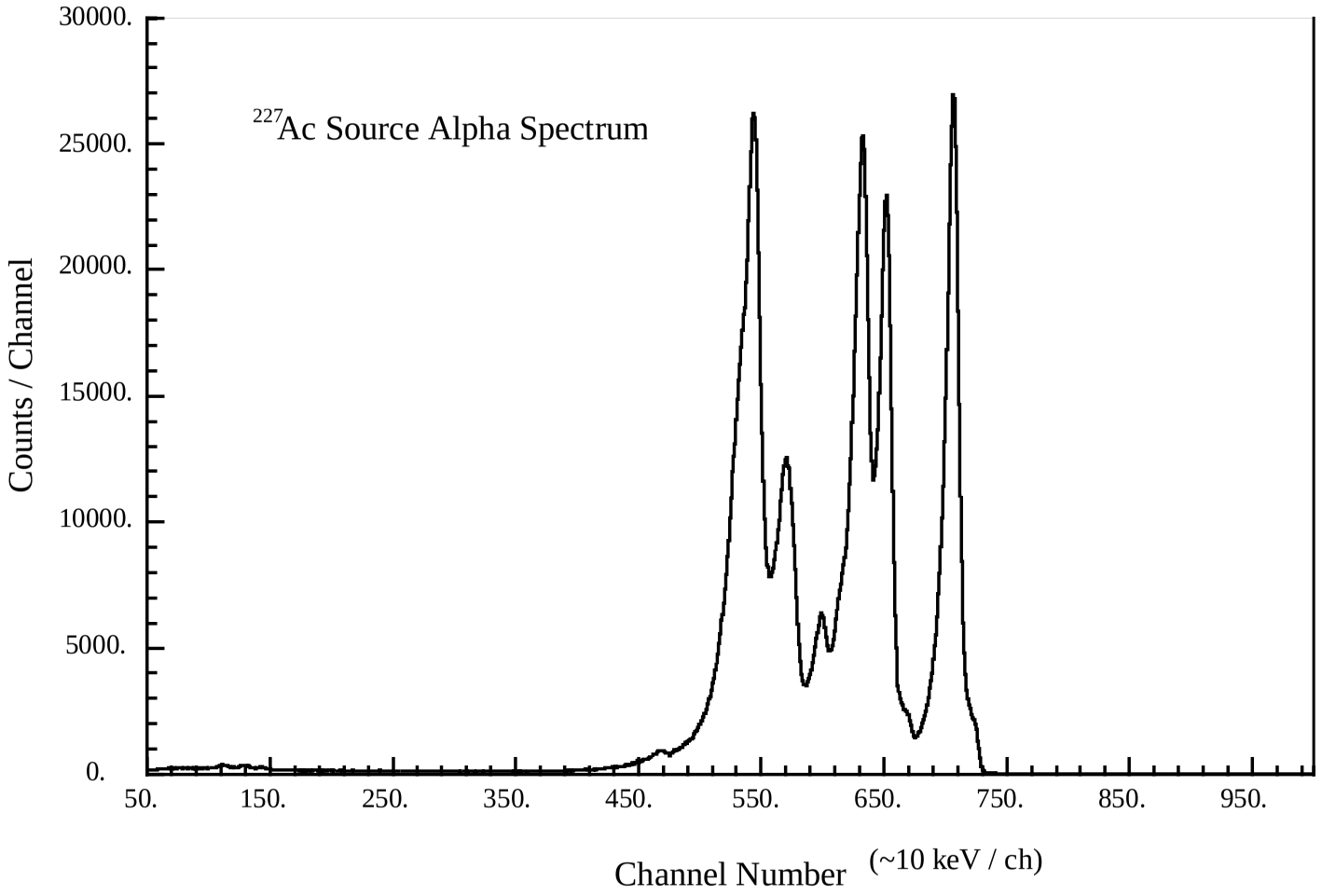

Figure 4.8: Typical Source Energy Spectrum from ^{227}Ac. Because of the thick gold layer covering the source, it was not useful for energy calibration purposes but was used for calibration of the beta-alpha timing.

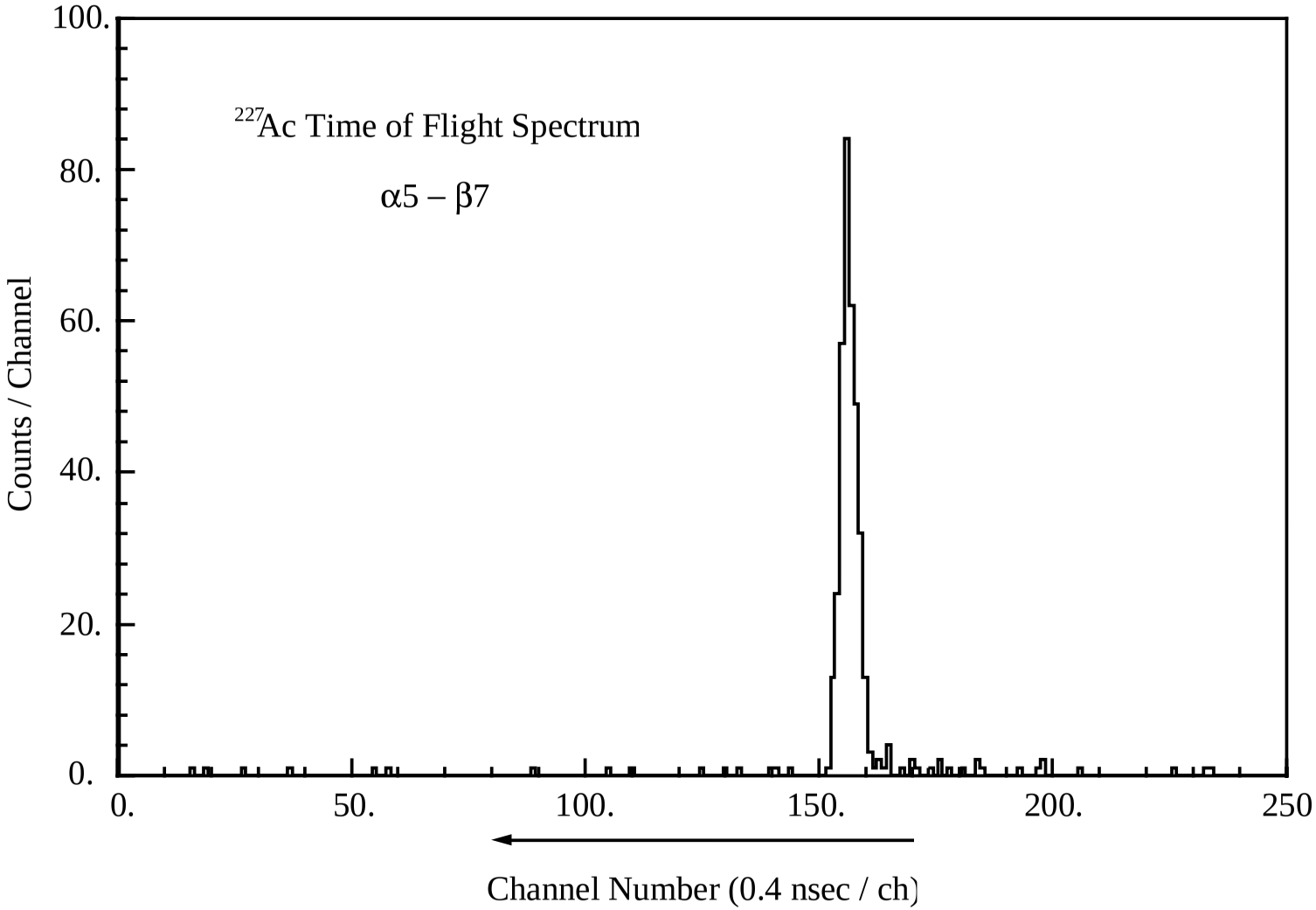

Figure 4.9: Typical Timing Spectrum from ^{227}Ac exhibiting time resolution FWHM = 1.6 nsec at 5 to 7 MeV and signal to background ratio of better than 100:1.

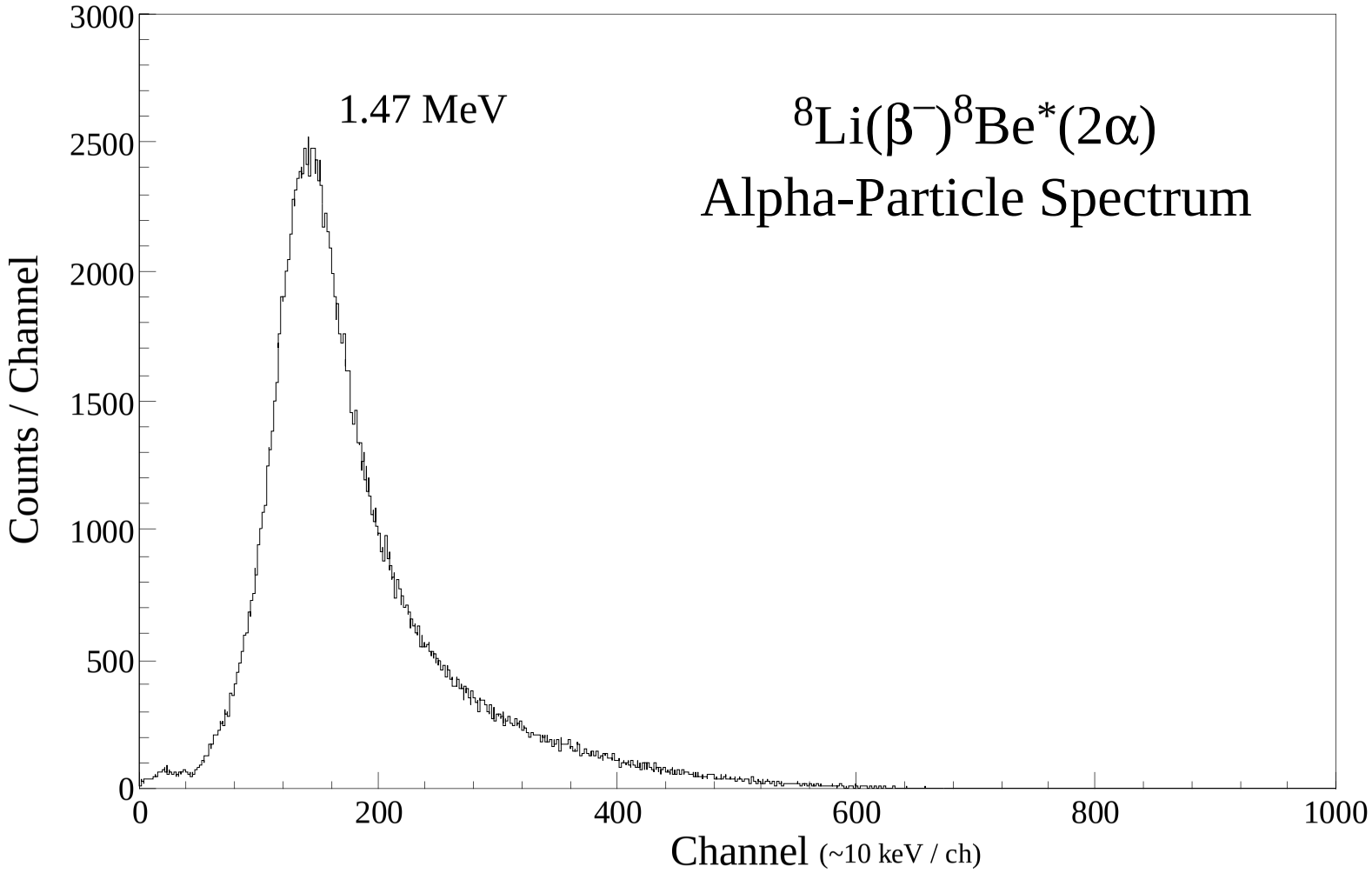

Figure 4.10: Typical ^{8}Li Beta-Delayed Alpha-Particle energy Spectrum.

was not used in further analysis. These fits were used as a transform each two dimensional histogram into one with a standard value for the constants A and B.

Using these fits the remaining 99 two dimensional histograms (excluding those of beta-6) were summed together (see fig 4.11). When sliced in 50 keV wide energy bins, the ^{8}Li provides an accurate measurement of the TOF line shape (centroid, width and asymmetry) of the ^{16}N data, as shown in fig 5.3 in the following chapter. Due to the higher beta-particle energy in the ^{8}Li decay, we observe a systematic shift of one to two channels in the ^{16}N decay TOF spectra.

L: Detector Efficiency

In our experiment the efficiency of the SSB detectors is independent of energy for alpha-particles over the range from 500 keV to more than 8 MeV since all such alpha-particles are stopped completely in the active region of the detector. The low energy limit of 500 keV comes from thresholds in the electronics.

The threshold for our beta array was set at approximately 120 keV using a ^{137}Cs source, which is high enough to cut into the lower energy beta-particles which accompany our higher energy alpha-particles. This effect is only important for detected alpha-particle energies in excess of 1600 keV (corresponding to a beta-particle endpoint of 900 keV), and was measured by comparing the alpha-particle singles spectrum to the alpha-particle coincidence spectrum over this energy range. Below alpha-particle energies of 1200 keV (corresponding to a beta-particle endpoint of 1.5 MeV) no correction was necessary at all, with a constant efficiency confirmed using ^{8}Li data, which has much higher beta-particle energies, up to a beta-particle endpoint of 12 MeV. A systematic error of 5% was included for all data points at energies greater than 1200 keV from this correction (as seen in fig 5.6 of the next chapter).

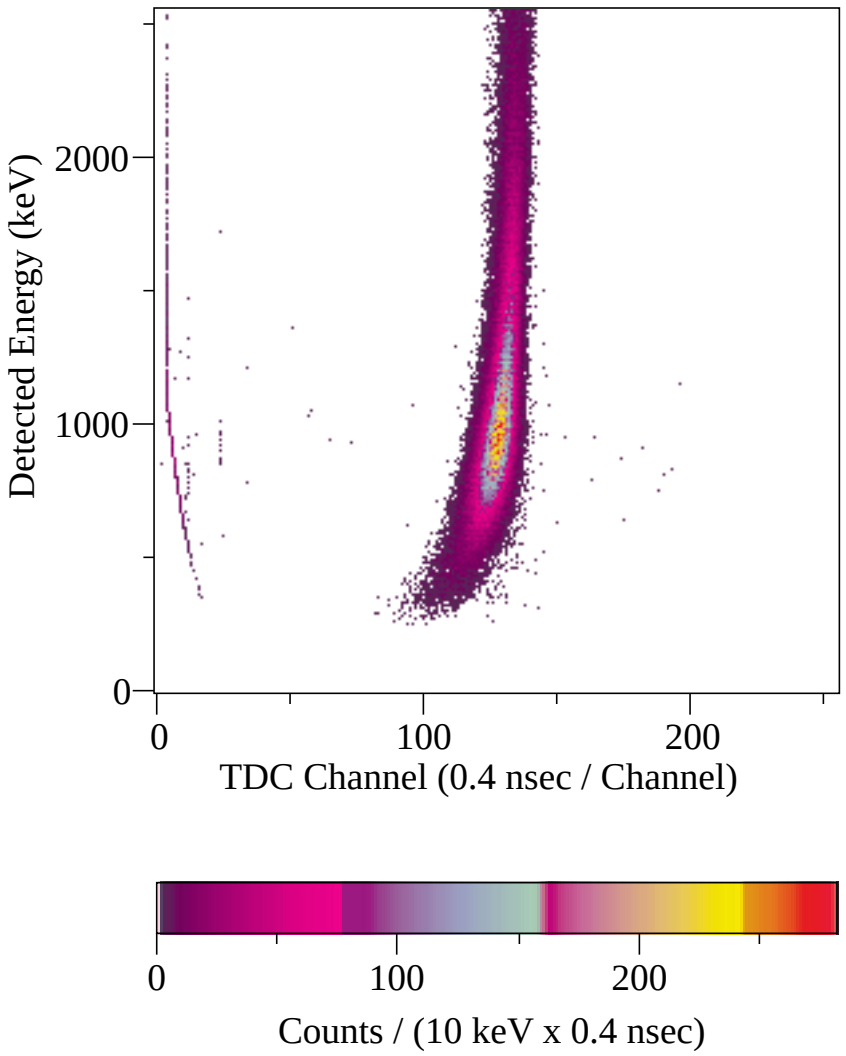

Figure 4.11: Summed 2D timing vs alpha-particle energy plot for beta-delayed alpha-particles from ^{8}Li.

V: Experimental Results and Data Analysis

A: Alpha-Particles in Singles

Our final experimental runs took place during June and July of 1995. Over four weeks approximately 1.3 million alpha-particles were detected in the main peak (see fig 5.1); approximately two days of this period were dedicated to Lithium calibration runs.

B: Alpha-Particles in Coincidence

Using the ^{8}Li fits described previously, the two dimensional ^{16}N histograms were summed together using the Oak Ridge program TDX. Approximately one third of the detector, those located furthest from each other, had significantly worse time resolution than the others due solely to geometric effects. We did not use these detectors in further analysis.

The summed two dimensional spectrum (see fig 5.2) was then cut into 50 keV wide energy slices; typical 50 keV ^{8}Li and ^{16}N slices are shown in figure 5.3. The shapes of the alpha-beta coincidence peaks for ^{16}N data match those of the ^{8}Li calibration data with the peak centroids of the ^{8}Li data shifted to slightly lower channels due to the higher energy beta-particles in the lithium decay. Figure 5.3 also shows the actual fits for the 820 keV slice for ^{16}N. These slices were fitted using SAMGR and the resulting peak areas are plotted in fig. 5.4. Fig 5.5 shows our spectrum after correction for the coincidence efficiency of the beta-array (see previous chapter).

C: Background

The two primary sources of background in the low energy coincidence data are beta-gamma coincidences (i.e. the detection of a beta-particle in an alpha detector and a gamma-ray in a beta detector) and partial charge collection in the alpha detectors. The alpha-beta coincidence peak is well separated from the beta-gamma peak where the majority

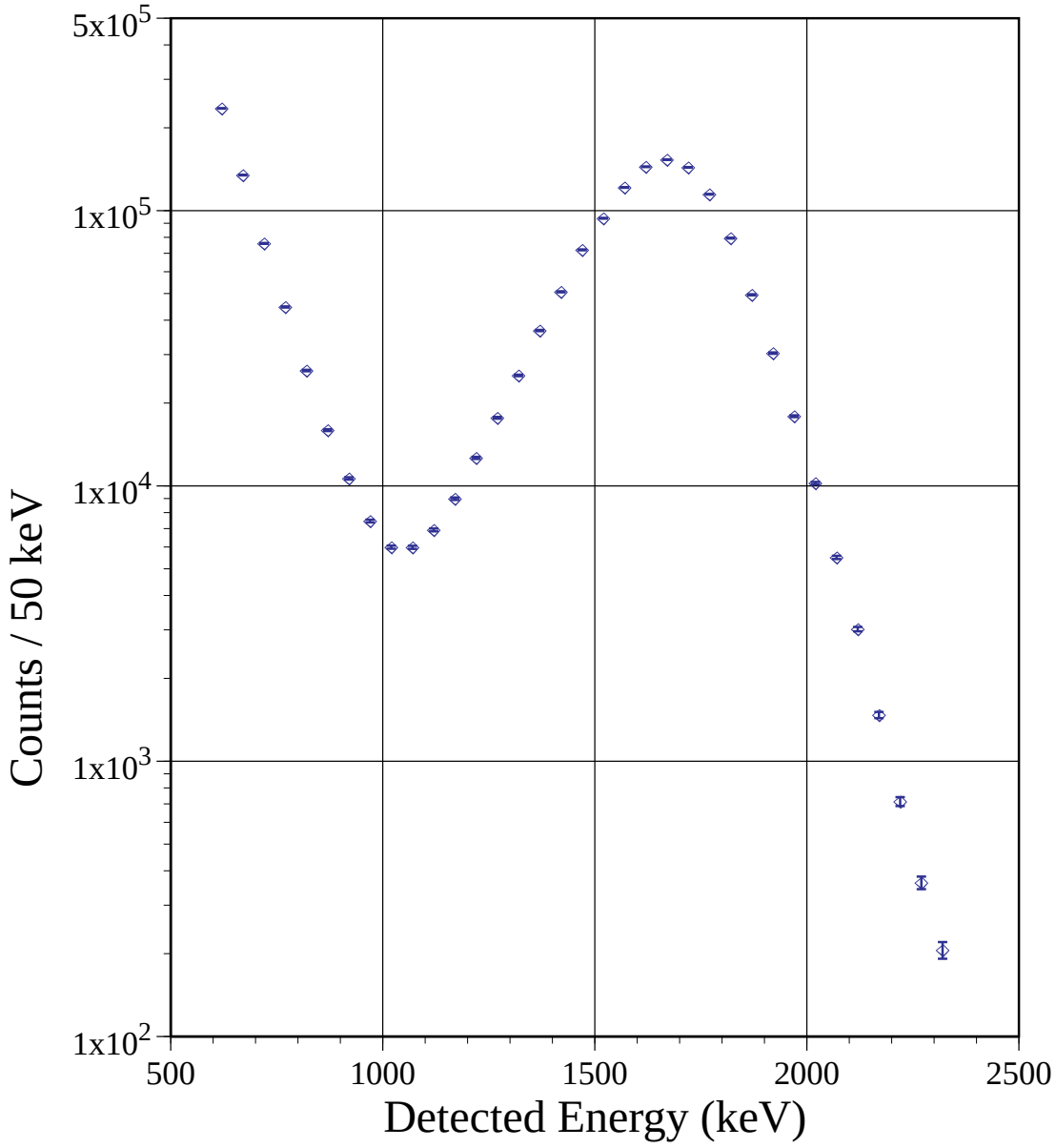

Figure 5.1: Alpha-particle spectrum measured in singles. The high number of low energy counts are from beta-particles and are removed through coincidence requirements and measurement of alpha-beta time differences.

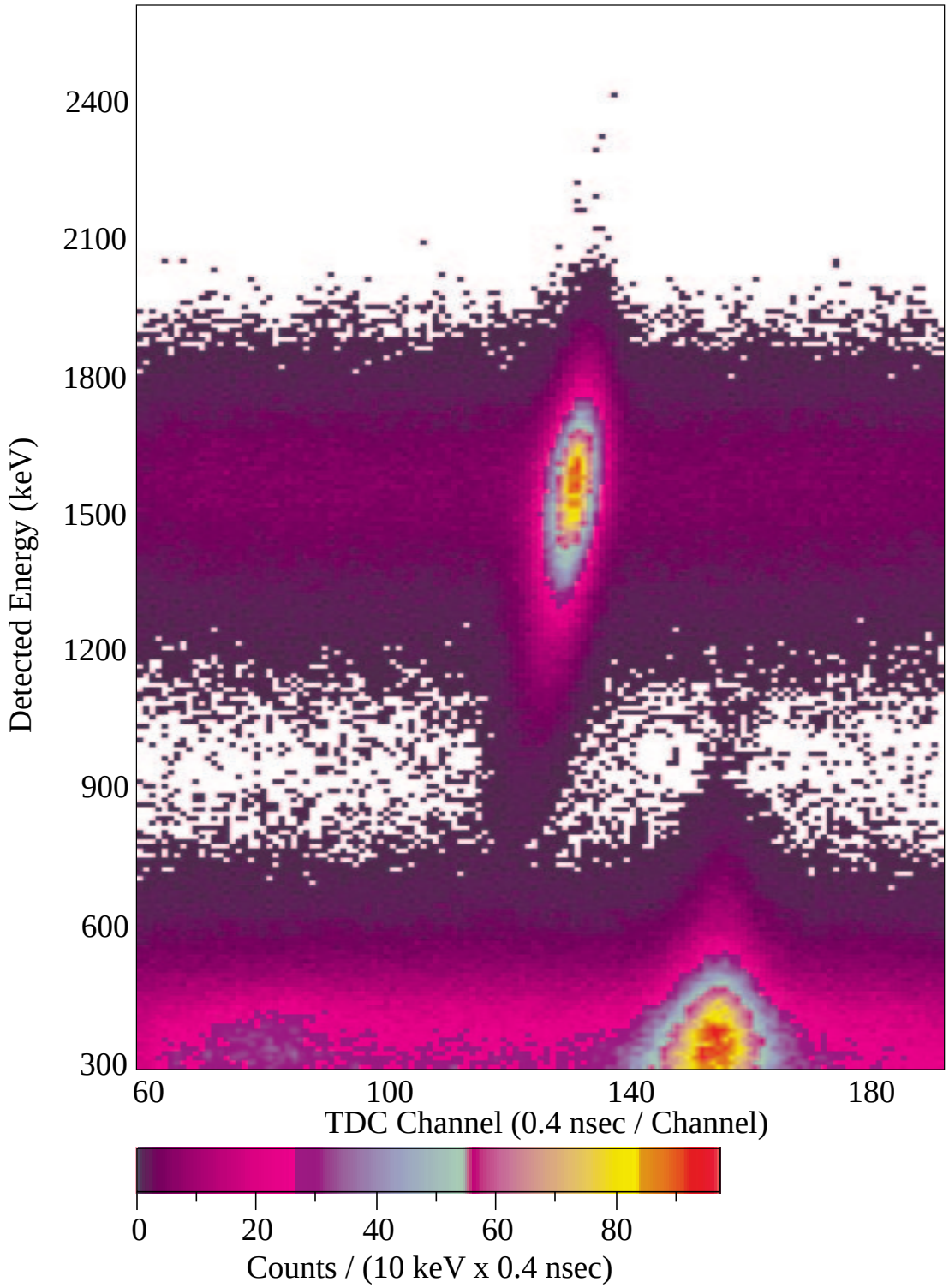

Figure 5.2: Summed ^{16}N data in 2 dimensional timing vs energy plot. This represents data from the June portion of the final experimental runs.

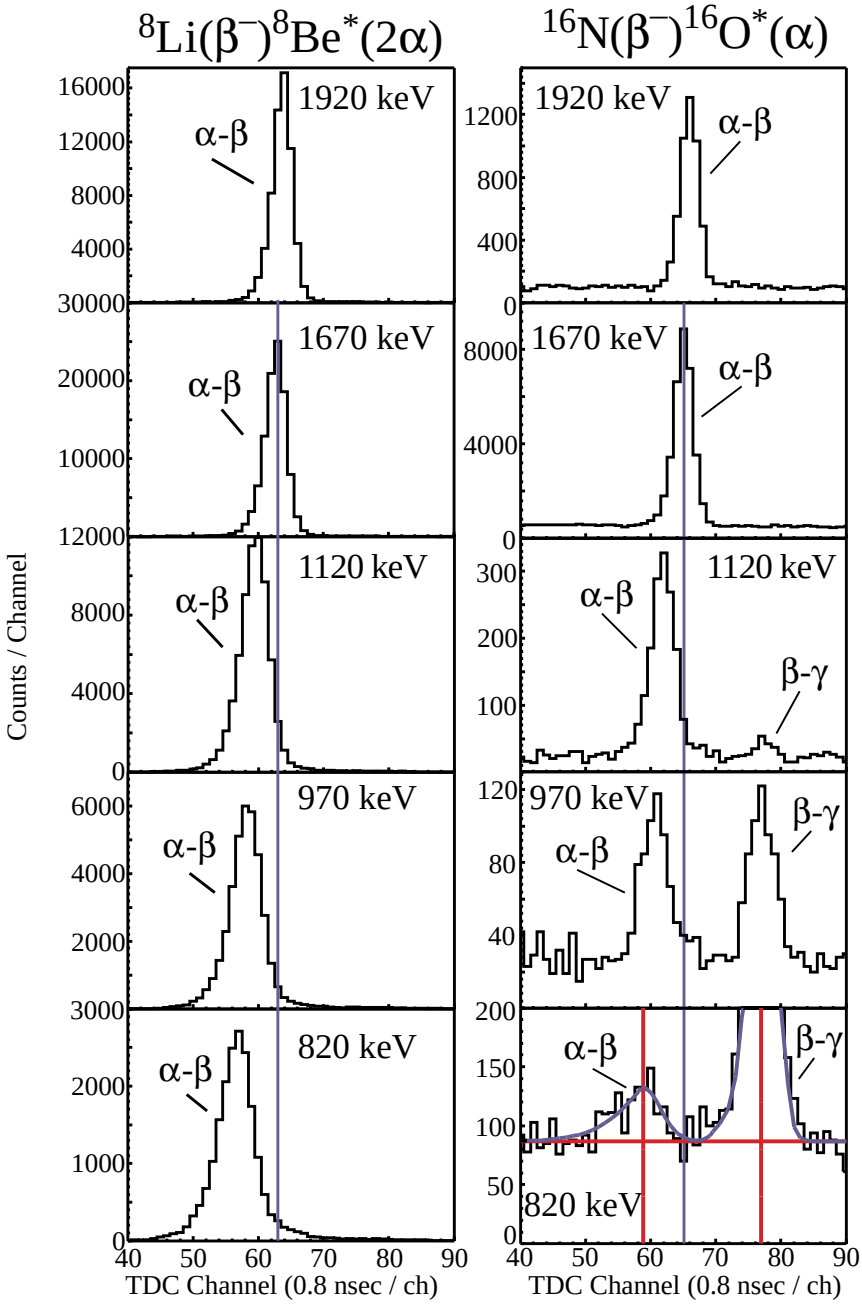

Figure 5.3: Typical 50 keV wide slices from the 2 dimensional ^{8}Li and ^{16}N time vs energy plots projected upon the time axis. These were used to calibrate the 99 working detector pairs in time. Beta-detector 6 was not operational during the final experimental runs. Notice that the width of the alpha-beta coincidence peak increases greatly at low alpha-particle energies. The alpha-beta coincidence peak is well separated from the beta-gamma peak at low energies, and due to the kinematics, is also distinguishable from signals caused by partial charge collection in the alpha detector. The 1670 keV slice is at the central peak for ^{16}N and the line drawn through it is clearly separated from the alpha-beta coincidence peak at lower energies. The ^{8}Li slices are located at slightly lower channels due to the higher energy beta-particles in the Lithium decay.

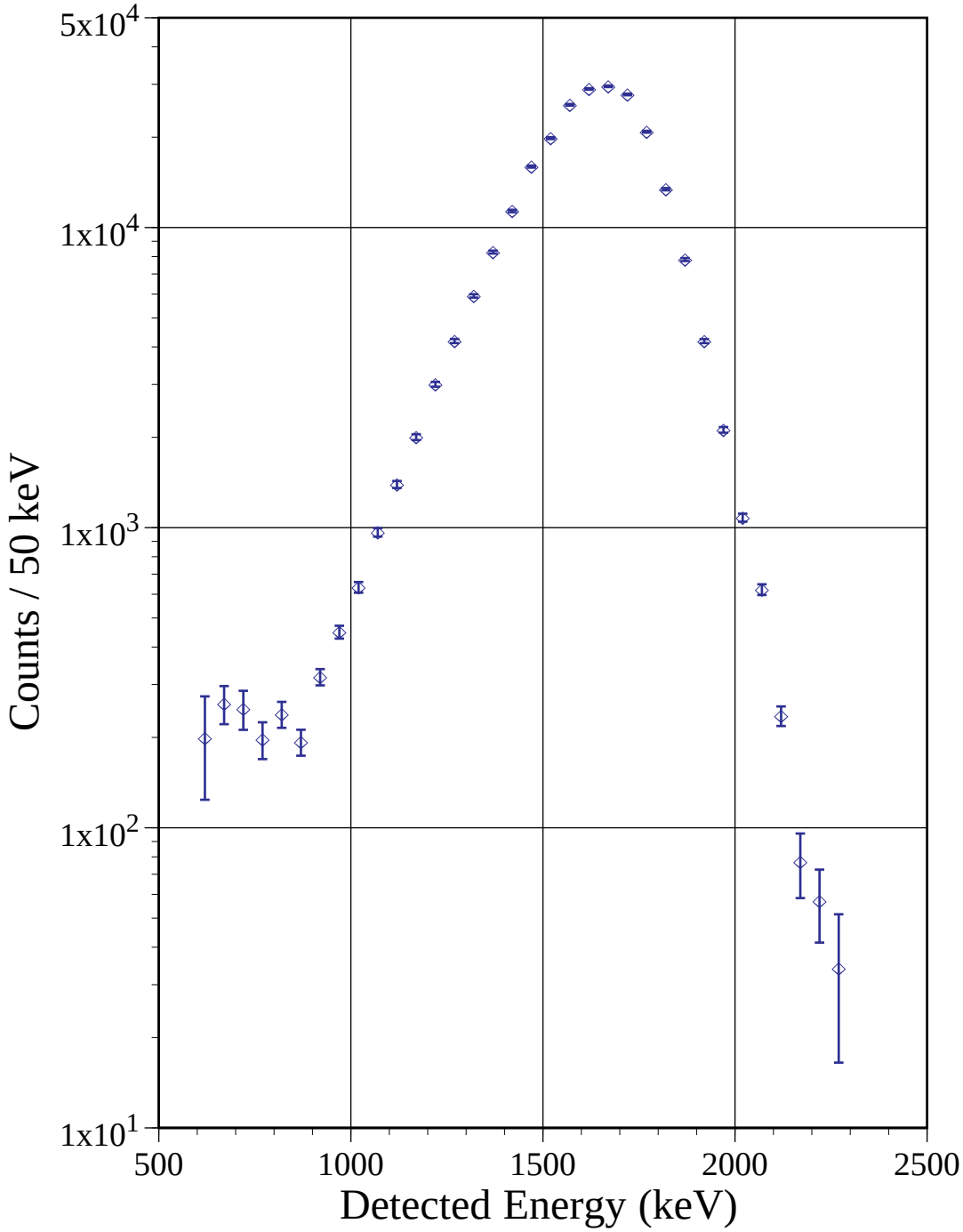

Figure 5.4: Uncorrected Beta-delayed alpha-particle spectrum of ^{16}N

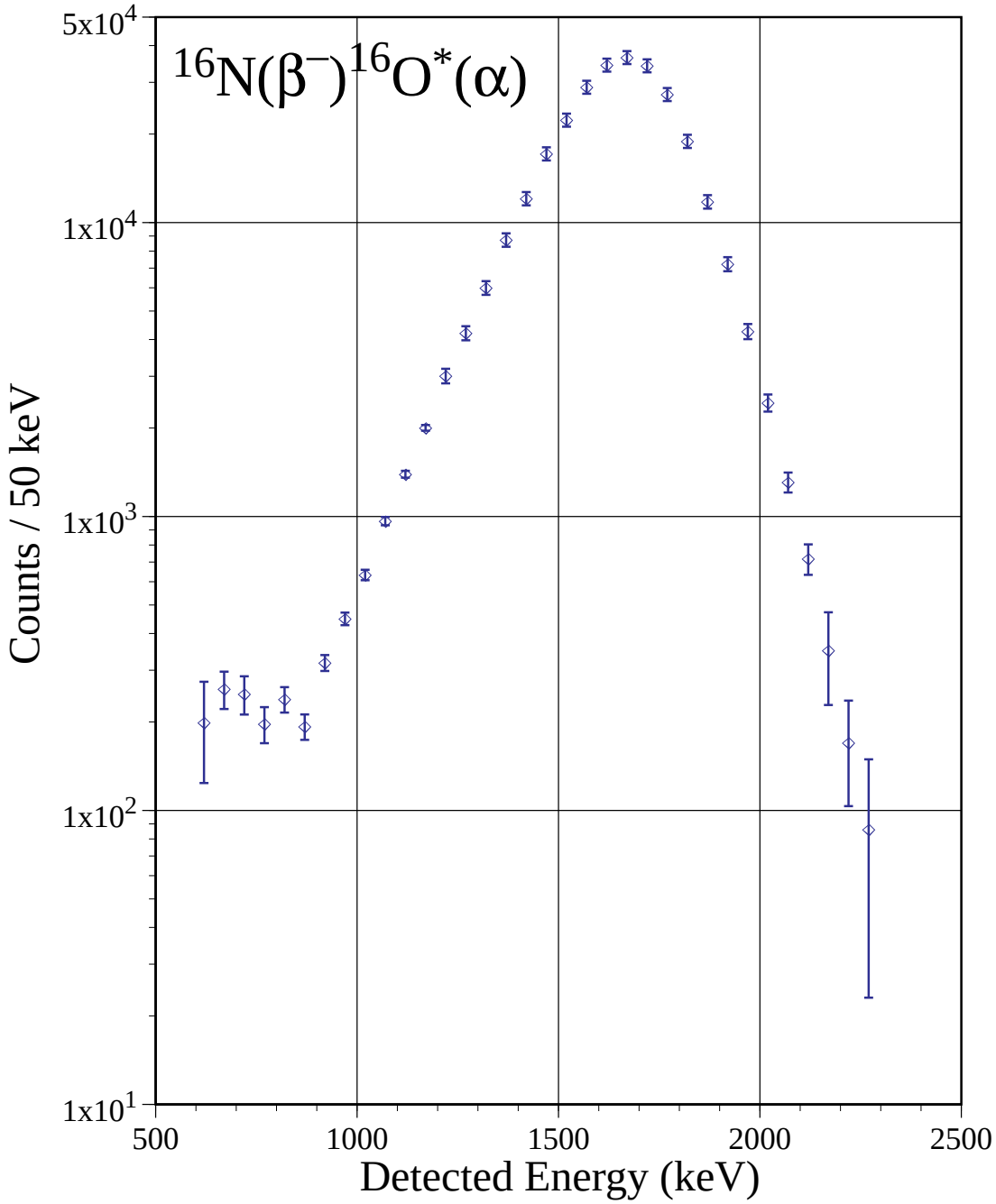

Figure 5.5: Spectrum of beta-delayed alpha-particles from ^{16}N corrected for beta array coincidence efficiency.

of the beta-gamma coincidences occur, and is kinematically shifted in time with respect to signals caused by partial charge collection.

The beta-gamma coincidences come from two primary sources. First, the beta-delayed alpha-particle emission branch of ^{16}N decay accounts for only ~10^{-5} of the ^{16}N decays; approximately 74% decay via beta-delayed gamma-ray emission. Second, in the gas target the reaction ^{1}H(^{15}N,^{16}O)n has a similar cross section to the production of ^{16}N. The ^{16}O so produced is not a source of background; however, the neutrons activate the catcher foils producing significant amounts of ^{28}Al (with a lifetime of 2.24 minutes) which decays via beta-delayed gamma-ray emission. Due to the high rate of beta-gamma coincidences there is a significant level of random coincidences at lower alpha detector energies. As these are random events, this background is flat.

Two additional possible sources of background are true ^{12}C-beta coincidences (i.e. a recoiling ^{12}C ion in an alpha-detector and its corresponding beta-particle in a beta detector) and other nuclei with beta-delayed alpha emission. During the breakup of the ^{16}O* the alpha-particle takes away 75% of the available energy and the recoiling ^{12}C takes away only 25%. Additionally, it is known [Az94] that low energy ^{12}C has a significant pulse height deficiency in surface barrier detectors. The ^{12}C-beta coincidence peak can be seen in fig. 5.2 around TDC channel 80 below 450 keV in detected energy. Above 500 keV it is negligible.

The other nuclei with beta-delayed alpha lines which could be produced in our experiment are ^{8}Li and daughters of ^{227}Ac. Both of these would produce significant effects at higher energies (>2.1 MeV detected energy) that are not seen if they were affecting the measurements at low energy.

Additionally, other, unknown, sources of background in our apparatus were searched for both in this experiment and in the search for rank-one first forbidden beta-decay of ^{20}F [Wi96] that used the same apparatus, and none were found. Tests included the using of

empty gas targets (with pressure foils intact), empty catcher foil frames, and the full system running with the arm 90° out of phase.

D: Correction for Energy Shifts

The centroid of the alpha-particle detected energy peak was shifted downward due to the energy loss of the alpha-particles escaping from the catcher foils. Since the energy loss of alpha-particles is energy dependent, the shift for each of our 50 keV bins was calculated independently using the formulae of Ziegler [Zi77] and cross checked with the tables of Northcliffe and Schilling [No70] and the Monte Carlo code TRIM '92 [Zi92]. After this energy dependent shift was complete, all future spectra were plotted using the center of mass energy whereas the detected alpha-particle energy was used earlier.

E: Correction of Line Shape

As can be clearly seen in fig 5.6, the two Yale-UConn experiments agree fairly well. In particular, it is clear that the two experiments have the same line shape. At the time of the original Yale-UConn experiment this line shape was erroneously thought to include a low energy tail in the data. However, this was incorrect, and, as we demonstrate below, is a manifestation of the correction due to the TOF line shape.

If one has a spectrum constant in energy, the yield measured at each point in that spectrum is directly proportional to the energy integration interval. The same is also true with a spectrum in any physical variable. In the case of this experiment, the data are integrated over both time and energy with the integration intervals being the time and energy resolutions. The fact that these vary considerably over the energy range of the measurements is the cause of the distorted line shape. The energy resolution of our experiment is determined by the thickness of the catcher foils, as this is significantly greater than the inherent resolution of the alpha detectors themselves.

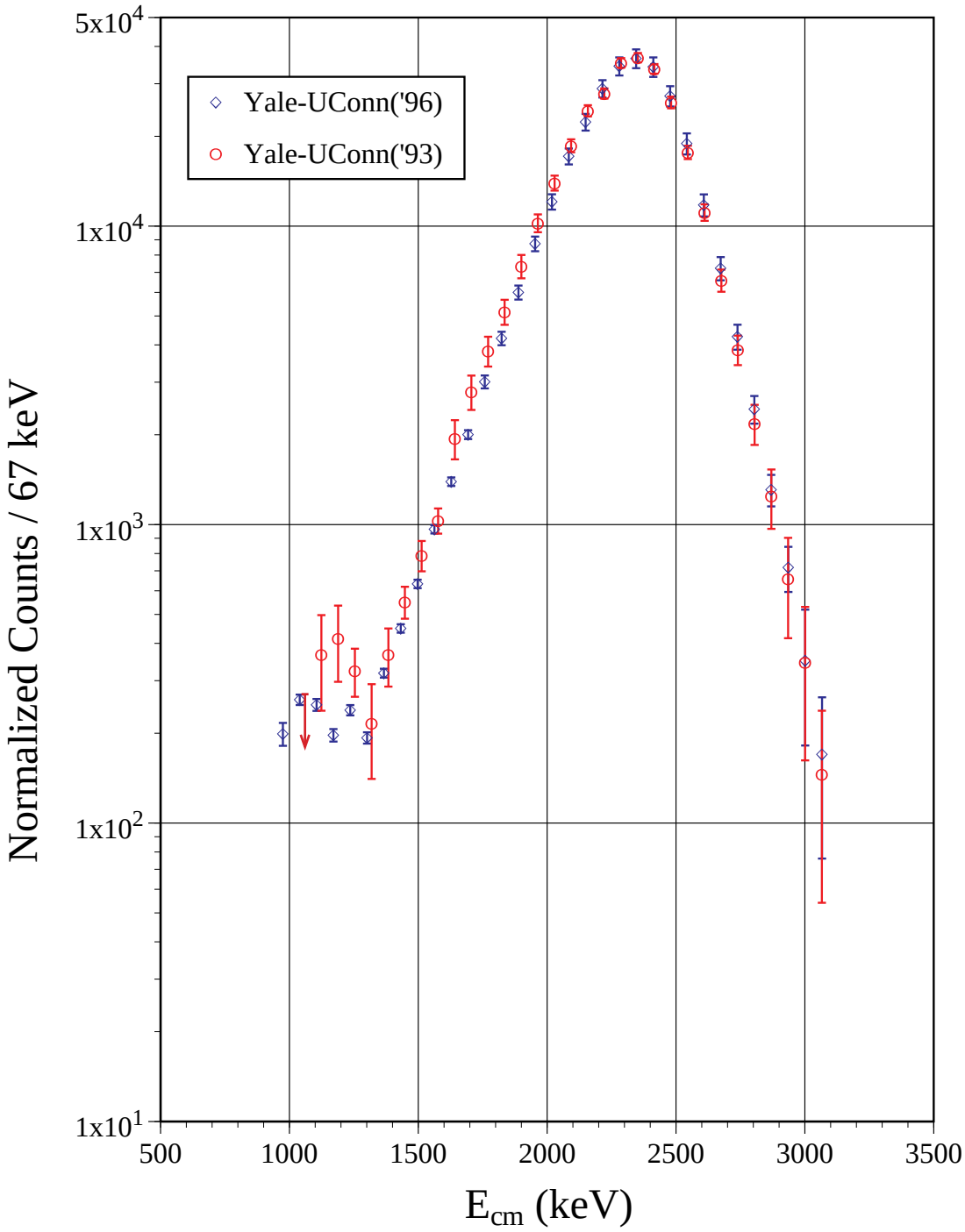

Figure 5.6: Beta-delayed alpha-particle spectra from both Yale-UConn experiments showing the same line shape. Both spectra have been corrected for beta array coincidence efficiency and energy shifts.

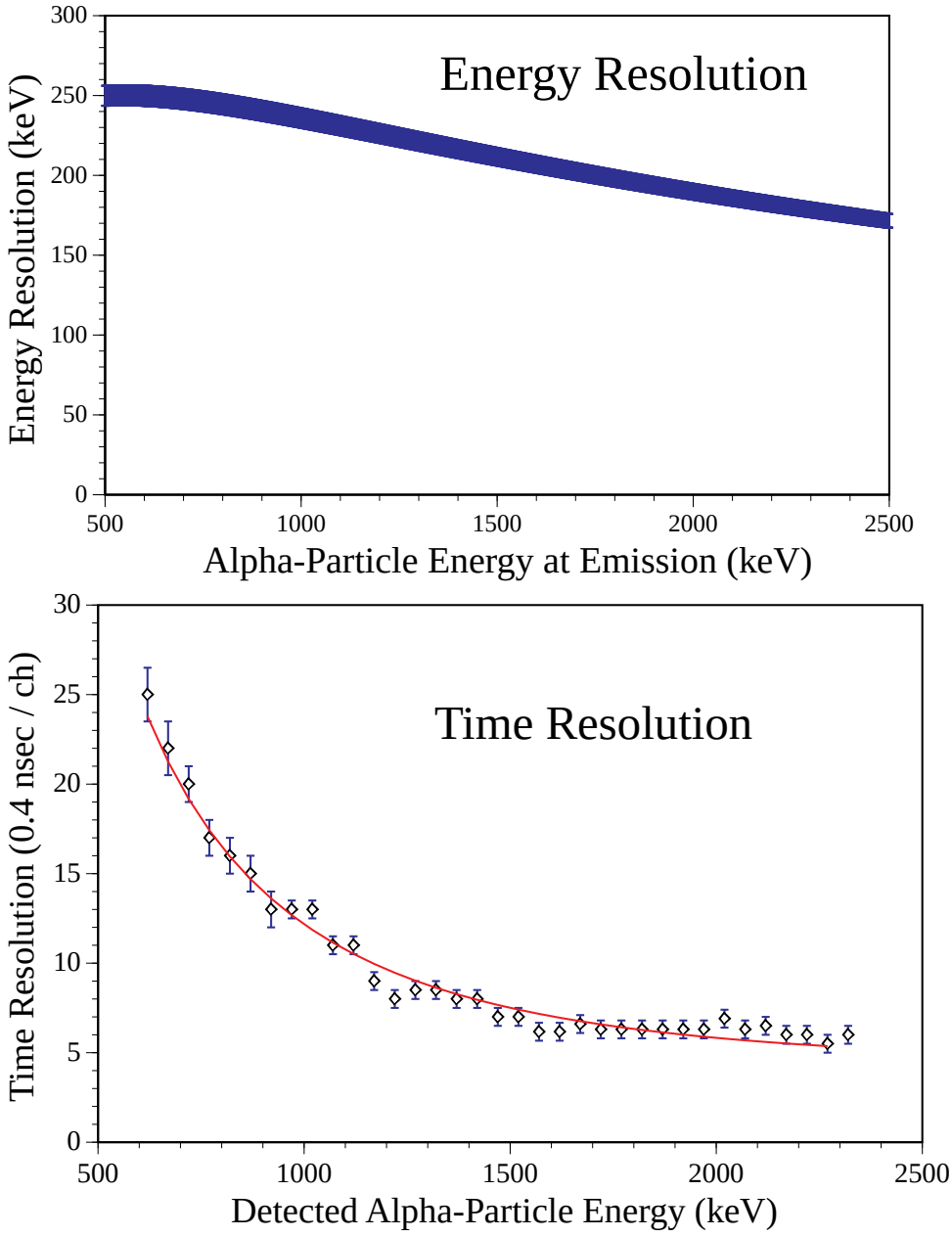

Figure 5.7: The energy and time resolution of the Yale-UConn('96) experiment as a function of energy. Both of these are FWHM. The energy resolution comes from the thickness of the aluminum catcher foil in which the ^{16}N is embedded. It is determined by using Ziegler's formulae upon the known effective thickness measured *in situ* using a ^{148}Gd source. The time resolution is based on measurements from the ^{8}Li calibration spectra fitted to a curve described in the text.

The resolutions are shown in fig 5.7. The energy resolution is calculated using Ziegler [Zi77] based upon the measured catcher foil thickness, and cross checked using Northcliffe and Schilling [No70] and TRIM '92 [Zi92]. The time resolution was measured using the ^{8}Li calibration data and fit to the function:

$$\Delta t = \sqrt{\left(\frac{A}{E^{3/2}}\right)^2 + B^2} \tag{5.1}$$

Of the two terms added in quadrature here, the first comes from the kinematics and has a fitted value of 11.4 MeV$^{(3/2)}$ nsec, and the second comes from the electronics and has a fitted value of 4.2 nsec.

The data points in the time resolution plot are highly correlated since each corresponds to a 50 keV slice—significantly smaller than the actual energy resolution as can be seen in the accompanying energy resolution plot.

After dividing out the time and energy resolutions shown in fig 5.7, and normalizing the primary peak height, the final corrected Yale-UConn('96) data are shown in fig. 5.8. It should be emphasized that this correction comes solely from well known and measured quantities unlike the correction done in the original Yale-UConn experiment [Zh93a].

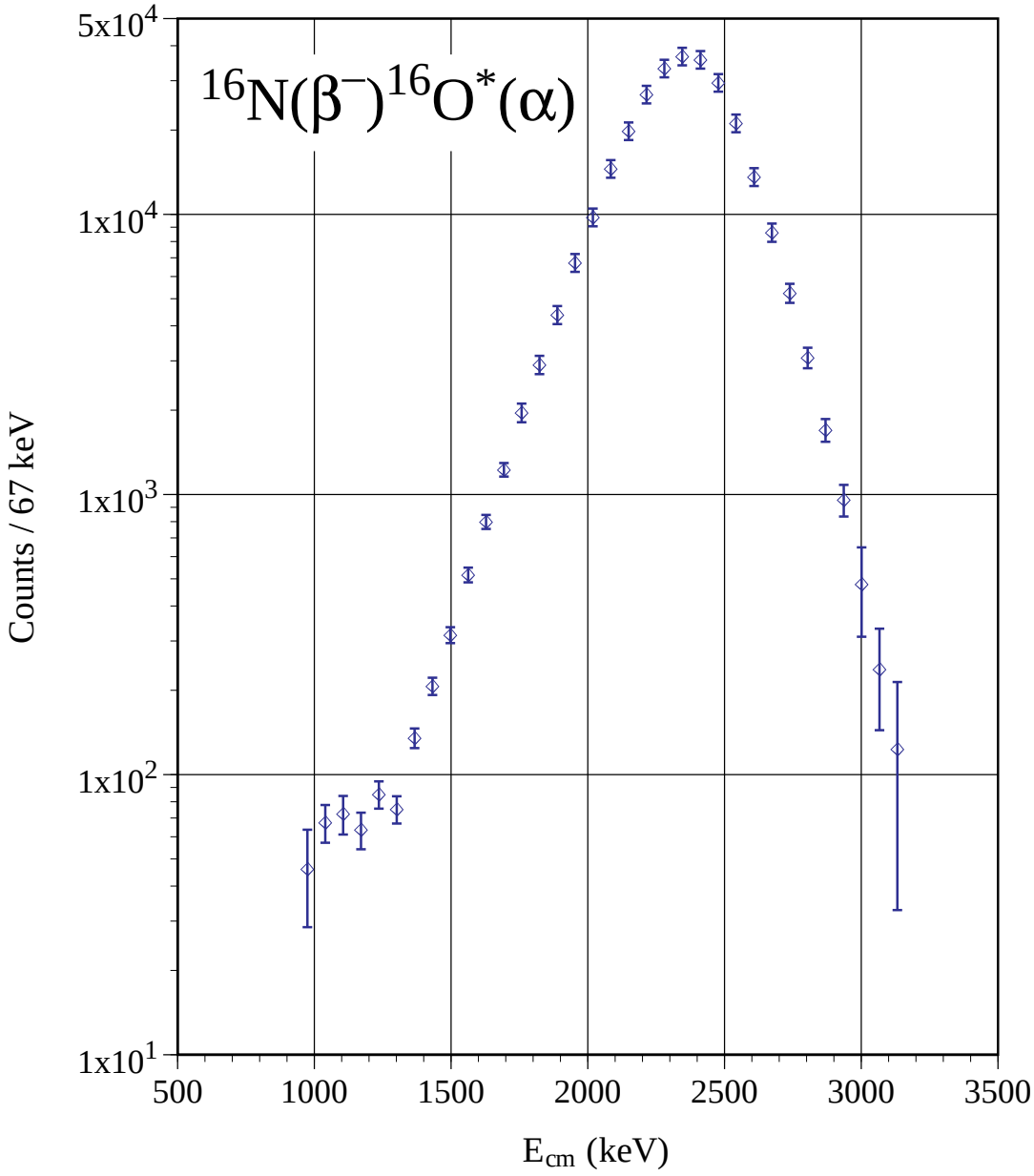

Figure 5.8: Final beta-delayed alpha-particle spectrum fully corrected for beta array coincidence efficiency and variable resolution induced line shape distortions.

VI: DISCUSSION

In addition to that from our experiment there are three high-statistics data sets for the beta-delayed alpha-emission of ^{16}N. The first was taken in Mainz, Germany by K. Neubeck *et al.* [Ne74], in a successful attempt to measure the 1.2825 MeV alpha particles resulting from the parity violating alpha-particle decay of the 8.8719 MeV 2^- state in ^{16}O. This line was observed at 1.282 MeV [Ne74], within 0.5 keV of the value of 1.2825 MeV extracted from high resolution gamma-ray measurements [Ti93]. For their energy calibration Neubeck *et al.* also used the ^{10}B(n,α)^{7}Li method to achieve a highly accurate energy calibration [Ne74]. In addition, the energy of the maximum of the principle peak in the Mainz('71) data set agrees with that of all the other data sets [see Appendix A]. In this Mainz experiment a 3 MeV Deuterium beam and a ^{15}N gas cell target were used to produce the ^{16}N. The activated gas was placed into small (2 cm^3) counting chambers which were viewed by four SSB detectors each with a depletion depth of 35 μm [Ne74]. The alpha-particle spectrum was taken in singles only. Additionally a beta-particle spectrum was taken in order to subtract out the beta-particle background at lower energies. Of the very high statistics spectrum taken only a small portion containing a little more than 3 x 10^7 events is available for this analysis [Ne74, Ba96]. See Appendices A and B. This portion of the data set comes from the original letter sent to F.C. Barker on 5 Feb. 1971. A copy of this letter is in Appendix B. The Mainz '71 data set, including the effects of the beta-particle background subtraction, is shown in fig 6.1.

The second data set was taken at TRIUMF in Canada and analyzed by J.D. Powell *et al.* using both **R**-Matrix and **K**-Matrix methods [Po95, Az94, Bu93] and contains approximately 1.25 x 10^6 events. In this experiment the ^{16}N was produced using a 500 MeV proton beam and a target of thick zeolite. From the target a low energy molecular beam was produced and deposited on a thin (10 μg/cm^2) carbon foil. The collection foils were rotated 90° every three seconds to sit between three different pairs of very thin (10-15 μm) SSB

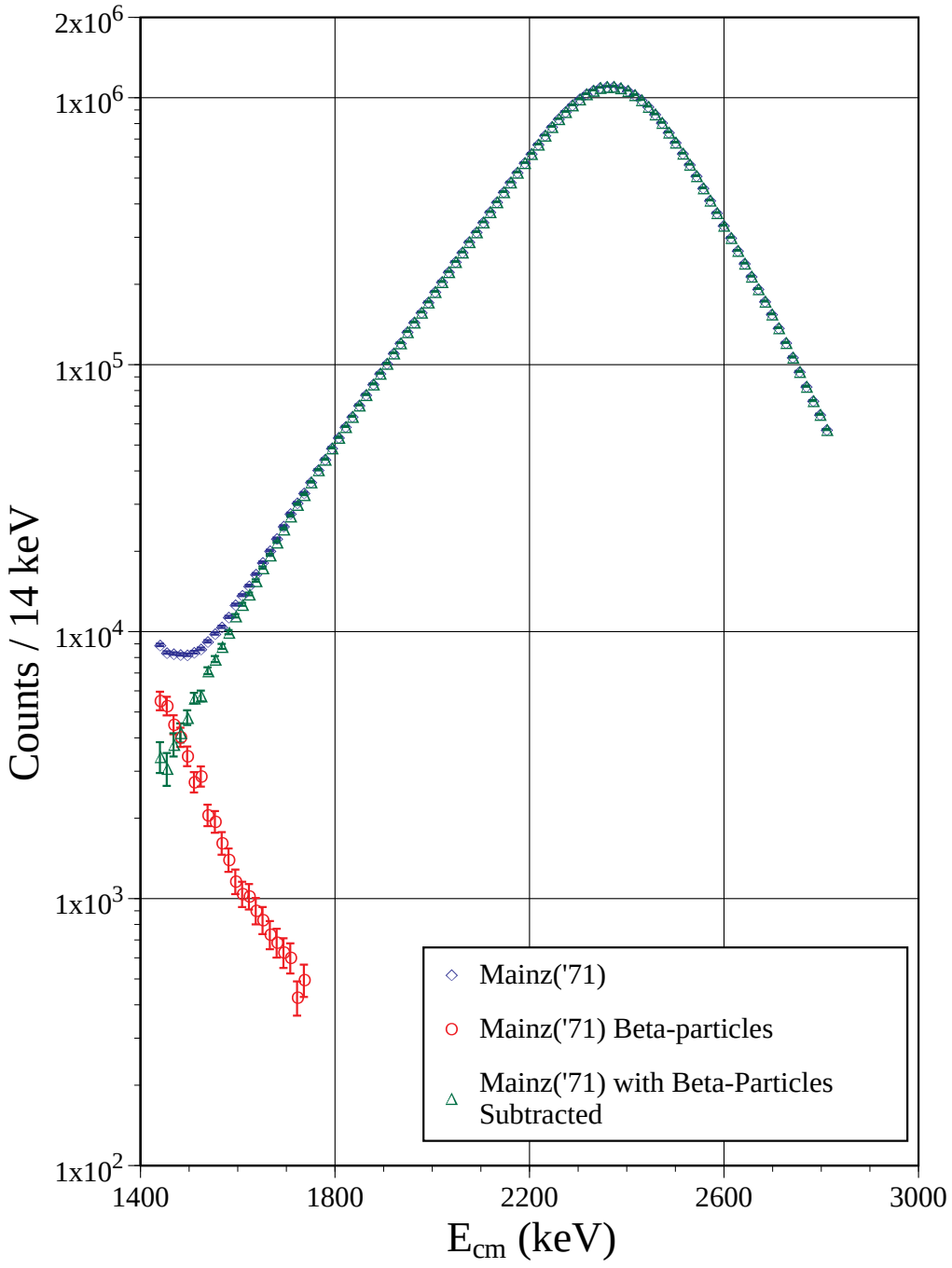

Figure 6.1: Mainz('71) beta-delayed alpha-particle spectrum from ^{16}N. This spectrum contains more than 32 million events. Shown here are the directly measured spectrum, the measured beta-particle spectrum, and the alpha-particle spectrum with beta-particle background subtracted out.

detectors. The alpha-particle spectrum was taken both in singles and in coincidence with the recoiling ^{12}C ions in the detector pairs. The multiple sets of detector pairs were necessary due to radioactive contaminants (in particular ^{17}N and ^{18}N) in the molecular beam. The TRIUMF group was able to subtract these contaminants by use of associated gamma-ray emission. A coincidence method was used to counteract the effects of partial charge collection in the SSB detectors and the alpha-particle straggling in the collection foils. [Po95, Bu93, Az94]. Two different data sets were published by the TRIUMF collaboration reflecting an energy recalibration [Po96, Bu93, Az94]. The two sets are listed in Appendix A and the **R**-Matrix fitted curve From Azuma *et al*. [Az94] is listed in Appendix C.

The third high statistics data set was taken and analyzed using the **R**-Matrix method by Z. Zhao *et al.* [Zh95] at Seattle and contains approximately 10^5 events. In this experiment the ^{16}N was created using a low energy Deuterium beam and a $Ti^{15}N$ target. The ^{16}N was collected on 15 $\mu g/cm^2$ carbon foils. The same alpha-particle ^{12}C ion coincidence method as that used by the TRIUMF collaboration was used. The Seattle data set is listed in Appendix A and the **R**-Matrix fitted curve is listed in Appendix C. [Zh95].

Fig. 6.2 shows a comparison of the reported Seattle(‘95) [Zh95] and TRIUMF(‘94) [Az94] **R**-Matrix fitted curves. The TRIUMF fitted curve used is the later, corrected curve, from the paper by R.E. Azuma *et al*. [Az94]. The two fitted curves are in fairly good agreement over most of the spectrum; however, there are significant disagreements in the width of the primary peak, with the greatest disagreements in the region of the interference minimum. Fig 6.3 shows a comparison of the Seattle(‘95) and TRIUMF(‘94) fitted curves to the Mainz(‘71) data set. The Mainz set contains the highest statistics yet fails to cover the region of the p-wave interference minimum. The Seattle fitted curve is in very good agreement with the Mainz(‘71) data set but the TRIUMF(‘94) fitted curve is not . At 1700 keV the TRIUMF(‘94) fitted curve already deviates from the Mainz(‘71) data by more than 20%. At this energy the number of counts are approximately 2% of the maximum at 2360 keV. If, in fact, the Mainz(‘71) singles spectrum includes a large contribution from partial

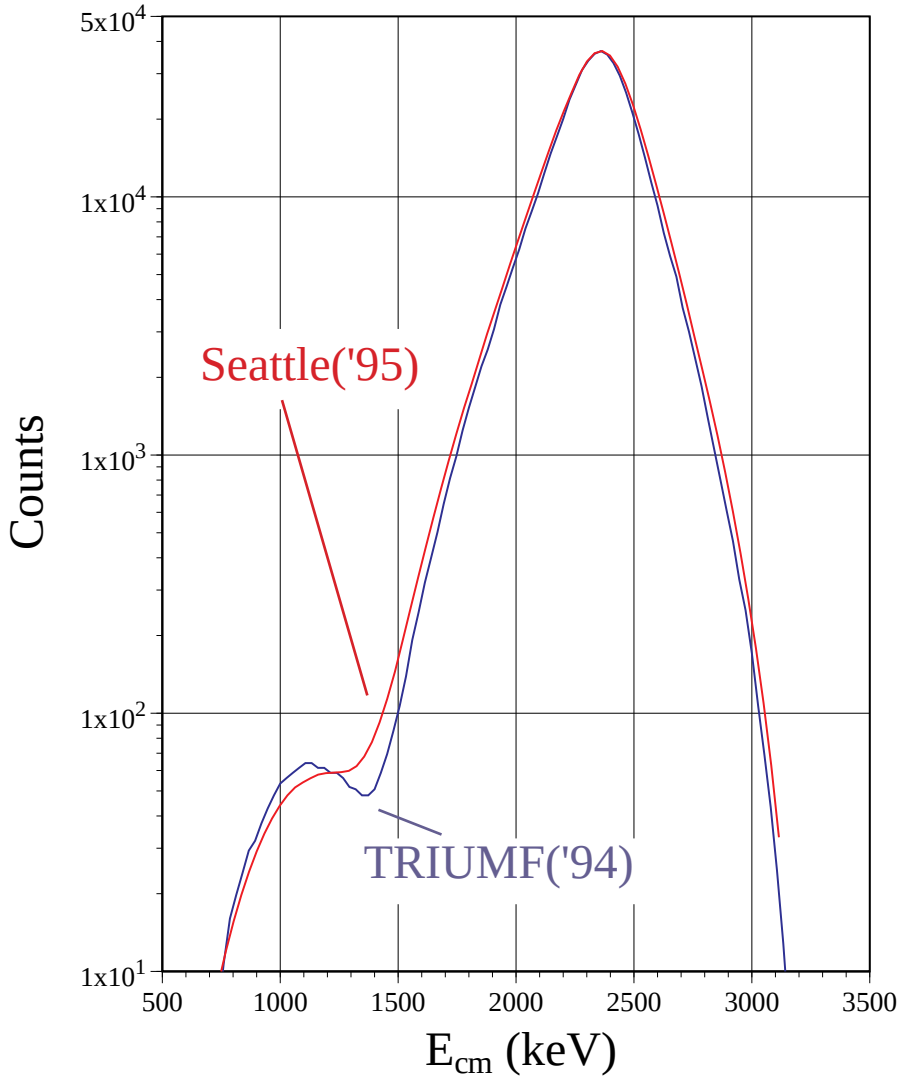

Figure 6.2: TRIUMF(‘94) **R**-Matrix fitted curve compared with Seattle(‘95) **R**-Matrix fitted curve. Notice in particular the differences between the two curves around the p-wave interference minimum at about 1400 keV and at high energies above 2500 keV.

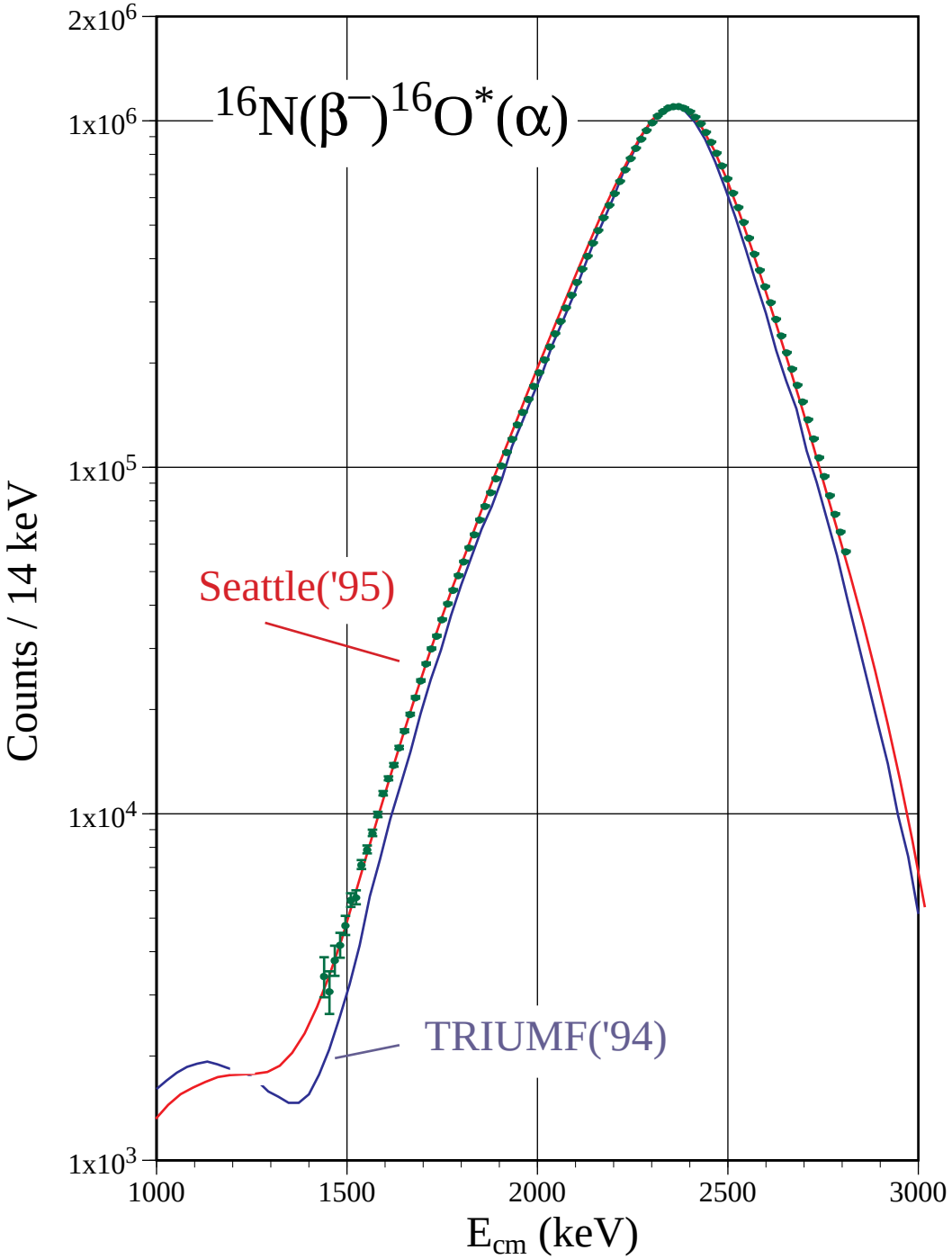

Figure 6.3: TRIUMF(‘93) and Seattle(‘95) **R**-Matrix fitted curves compared with Mainz(‘71) data.

charge collection etc., as suggested by Azuma *et al*. [Az94], it would imply that the Mainz('71) detectors were particularly bad, with signal to background ratios of order 50:1. This should be compared to a more common signal to background ratio of 500:1 as demonstrated in the Yale-UConn('96) experiment (see fig. 4.5). The Yale-UConn detectors were 50 μm thick while the Mainz detectors were 35 μm thick. In addition, the Seattle('95) data was collected using the same coincidence method [Zh95] as used by the TRIUMF collaboration and is in very good agreement with the Mainz('71) singles data. In a direct comparison of the three data sets, the χ^2 per data point of TRIUMF compared with Seattle is 11.4, TRIUMF compared with Mainz is 123 and Seattle compared with Mainz is 2.5.

The χ^2 per data point of two data sets a and b is defined as:

$$\chi^2 = \frac{\sum_{i=1}^{n} \left(\frac{(a_i - b_i)^2}{\sigma_{ai}^2 + \sigma_{bi}^2} \right)}{n} \tag{6.1}$$

with members a_i and b_i where the data sets are normalized at the primary maximum.

In order to compare the Yale-UConn('96) data set with the previous experiments it is necessary to average the results of the previous experiments over the variable energy resolution of the Yale-UConn('96) experiment (see fig. 5.8 and appendix C). Fig. 6.4 shows a comparison of the Seattle('95) [Zh94] and TRIUMF('94) [Az94] fitted curves averaged over the Yale-UConn('96) experimental resolution. In the averaging procedure the fitted curves were used rather than the data sets directly in order to minimize edge effects, and both fitted curves provide good representations of the respective data sets. As can clearly be seen, the Yale-UConn('96) experimental energy resolution is quite sufficient to distinguish between the two fitted curves. The Yale-UConn('96) data set and the two fitted curves, both before and after averaging over the Yale-UConn energy resolution are listed in Appendix C.

In fig. 6.5 the new Yale-UConn('96) data set is shown overlaying the averaged fitted curves of TRIUMF [Az94] and Seattle [Zh95] shown in fig 6.4. The Seattle **R**-Matrix fitted curve is confirmed by the Yale-UConn data set with a χ^2 per data point of 1.4; however, the Yale-UConn('96) data set does have slightly wider tails than the Seattle results do.

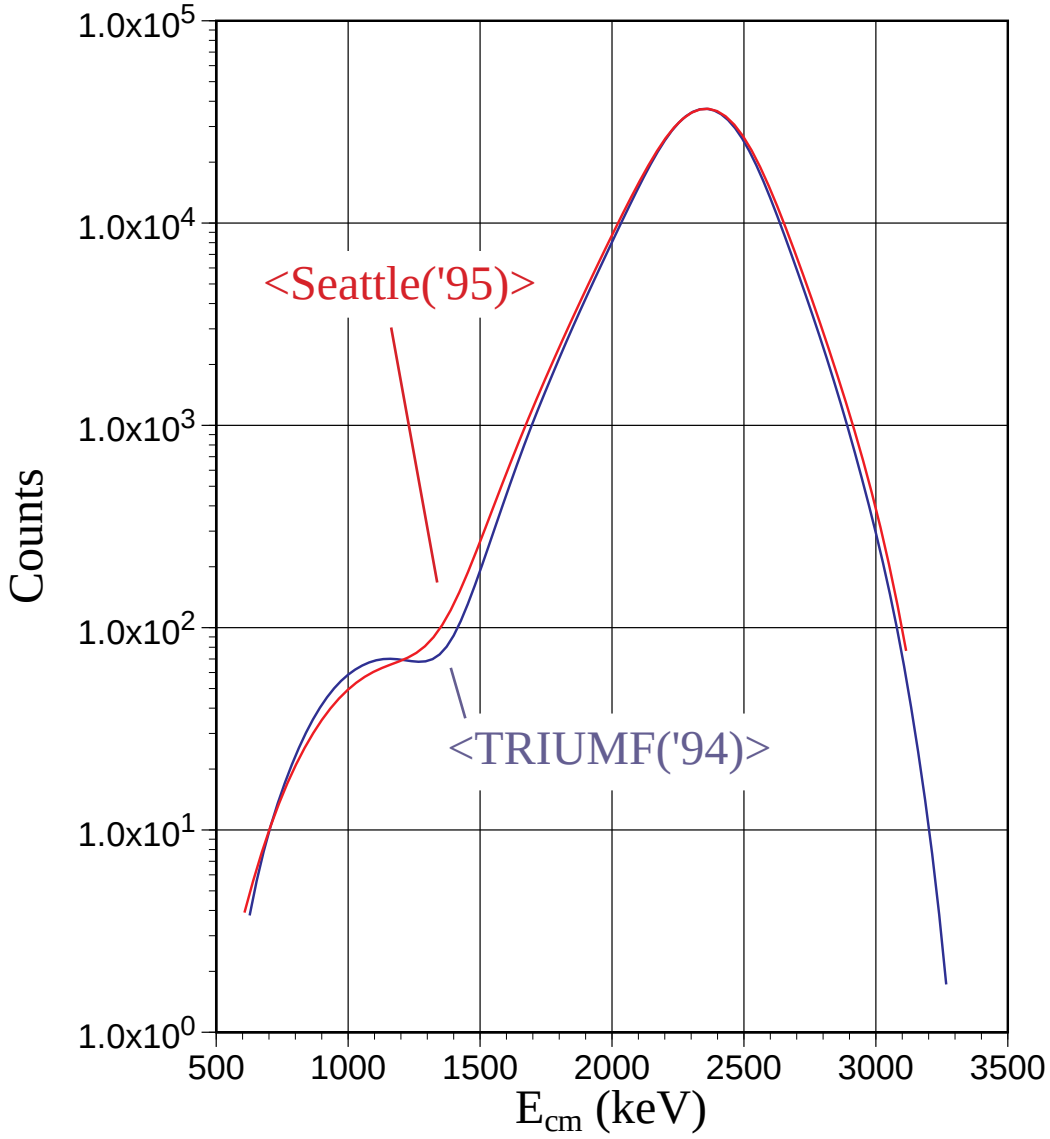

Figure 6.4: The TRIUMF(‘94) **R**-Matrix fitted curve averaged over the Yale-UConn(‘96) experimental resolution compared with the Seattle(‘95) **R**-Matrix fitted curve averaged over the Yale-UConn(‘96) experimental resolution. Because the primary features of the spectrum are hundreds of keV wide, the Yale-UConn(‘96) experiment, in principle, retains sensitivity to distinguishing between the two **R**-Matrix fitted curves.

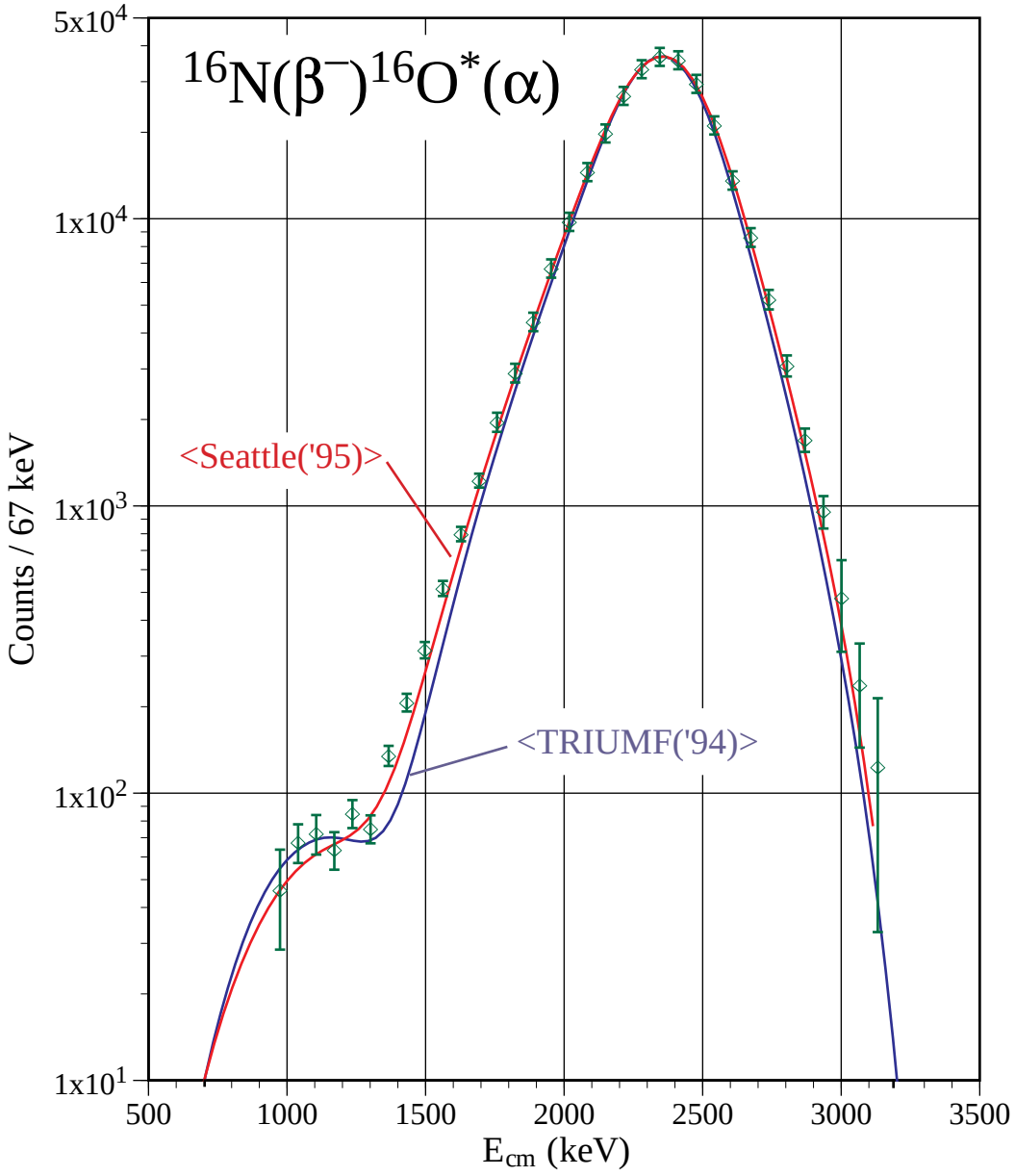

Figure 6.5: The TRIUMF(‘94) and Seattle(‘95) **R**-Matrix fitted curves compared with theYale-UConn(‘96) data, corrected for line shape. The **R**-Matrix fitted curves are averaged over the experimental resolution as shown in fig. 6.4.

The TRIUMF **R**-Matrix fitted curve disagrees with the Yale-UConn data set with a χ^2 per data point of 7.2, primarily caused by disagreements over the width of the primary peak. The Yale-UConn(‘96) data set is in agreement with the earlier Yale-UConn(‘93) results as shown in fig 5.6.

In order to better understand any discrepancies between the data sets, which are somewhat obscured by comparisons using logarithmic scales, in fig. 6.6a, 6.6b, and 6.6c the ratios of the data sets of Seattle(‘95) to Mainz(‘71), TRIUMF(‘94) and Mainz(‘71), and TRIUMF(‘94) to Seattle(‘95) respectively are plotted on linear scales. In fig 6.7a, the ratio of the averaged TRIUMF(‘94) theory curve to the Yale-UConn(‘96) data set is plotted. Fig. 6.7b shows the ratio of the averaged Seattle(‘95) theory curve to the Yale-UConn(‘96) data set. It is important to note that all the data sets which include the secondary maximum agree over the energy region of the secondary maximum. The principle disagreement is in the width of the primary peak, leading to discrepencies in the interference minimum.

The data sets disagree in that the FWHM of the primary peak in the TRIUMF(‘94) data set is about 330 keV, that of the Seattle(‘95) is about 355 keV, and that of Mainz(‘71) is about 350 keV (see Appendix A). In fact the original TRIUMF(‘93) version of the TRIUMF data set was approximately 10 keV narrower than the later TRIUMF(‘94) version. The ratio of the TRIUMF(‘94) to TRIUMF(‘93) data sets is shown in fig 6.8. This demonstrates that the narrow line shape advocated in the TRIUMF(‘93) paper by Buchmann *et al.* [Bu93, is an artifact of the data analysis.

The f-wave, which also comprises a portion of the secondary maximum, is solely determined by the depth of the secondary minimum. A significantly larger f-wave component to the secondary maximum would significantly affect the magnitude of the p-wave component of the secondary maximum, and thus the extracted S-factor.

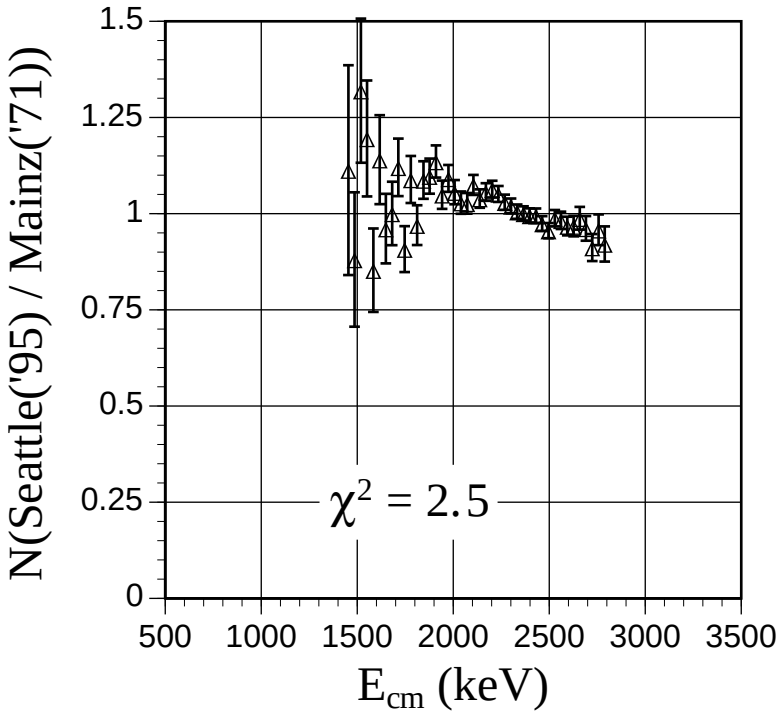

Figure 6.6a: Normalized ratio of Mainz(‘71) data to Seattle(‘95) data.

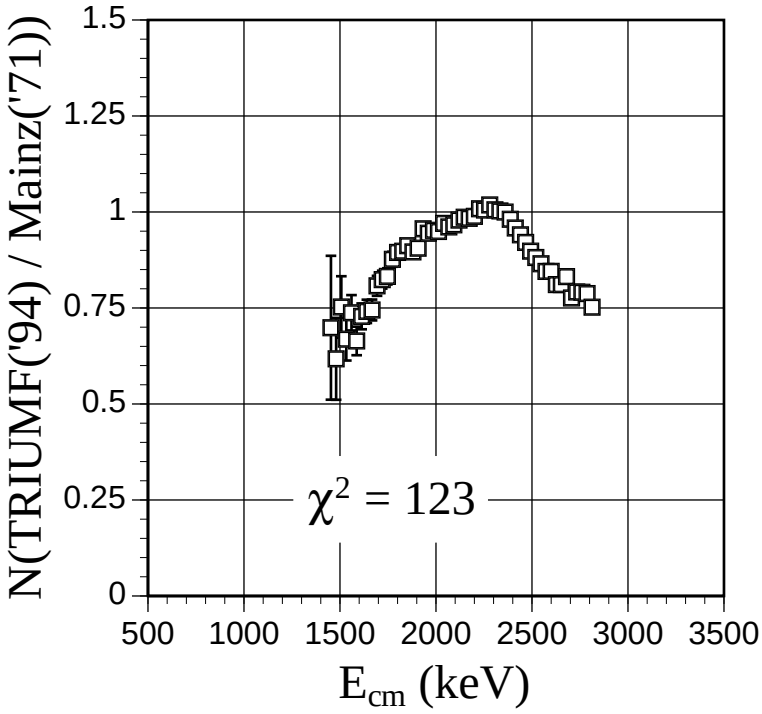

Figure 6.6b: Normalized ratio of TRIUMF(‘94) data to Mainz(‘71) data, clearly showing the high energy as well as low energy deficits in the TRIUMF data set that suggest a narrower line shape.

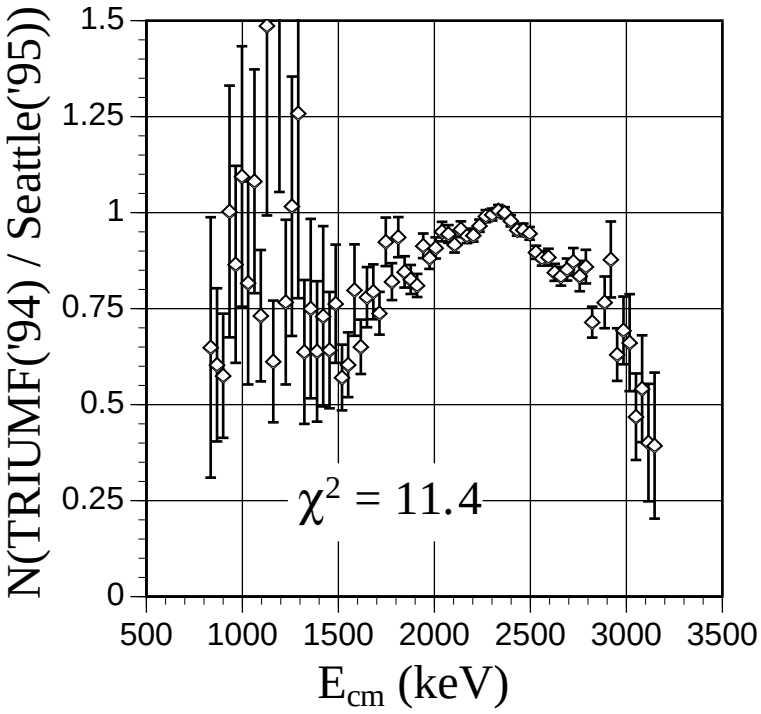

Figure 6.6c: Normalized Ratio of the TRIUMF('94) data set to the Seattle('95) data set. Note the deficits in the TRIUMF data set at both high energies (>2350 keV) and around the p-wave interference minimum (~1400 keV).

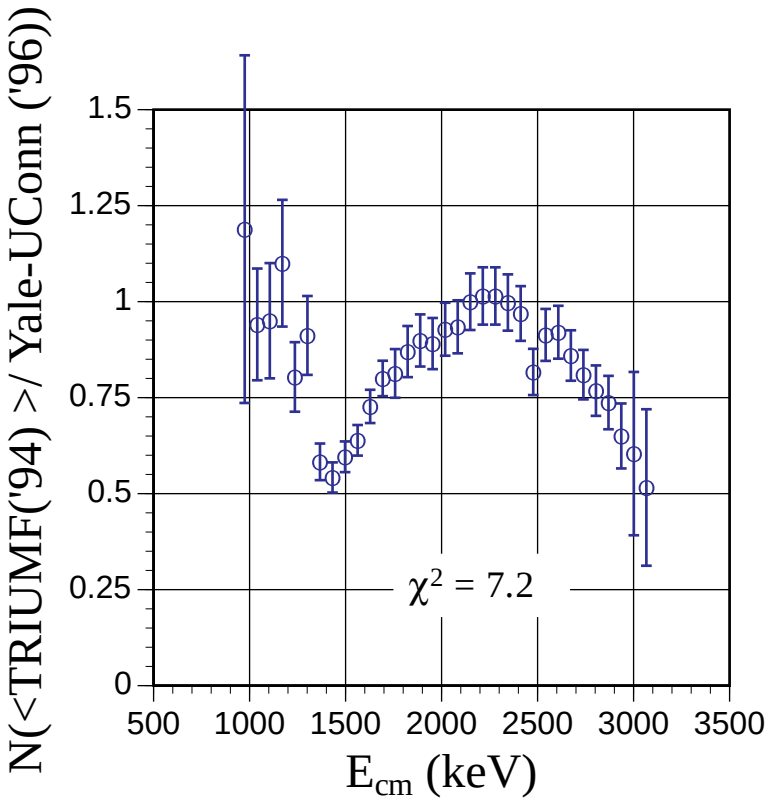

Figure 6.7a: The ratio of the averaged TRIUMF(‘94) **R**-Matrix fitted curve to the Yale-UConn(‘96) data set. Note the sharp disagreements at high energy and in the region of the p-wave interference minimum. χ^2 per degree of freedom is 7.2.

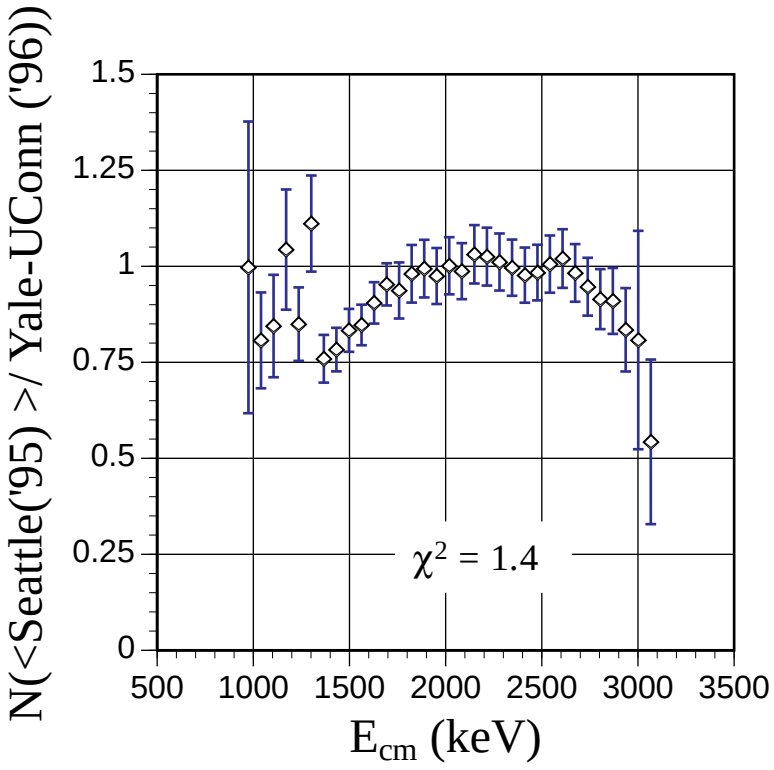

Figure 6.7b: Ratio of the averaged Seattle('95) **R**-Matrix fitted curve to the Yale-UConn('96) data. Note that over most of the energy range the two are in close agreement over most of the spectrum. The Yale-UConn('96) data set has slightly larger tails to the primary peak. χ^2 per data point is 1.4

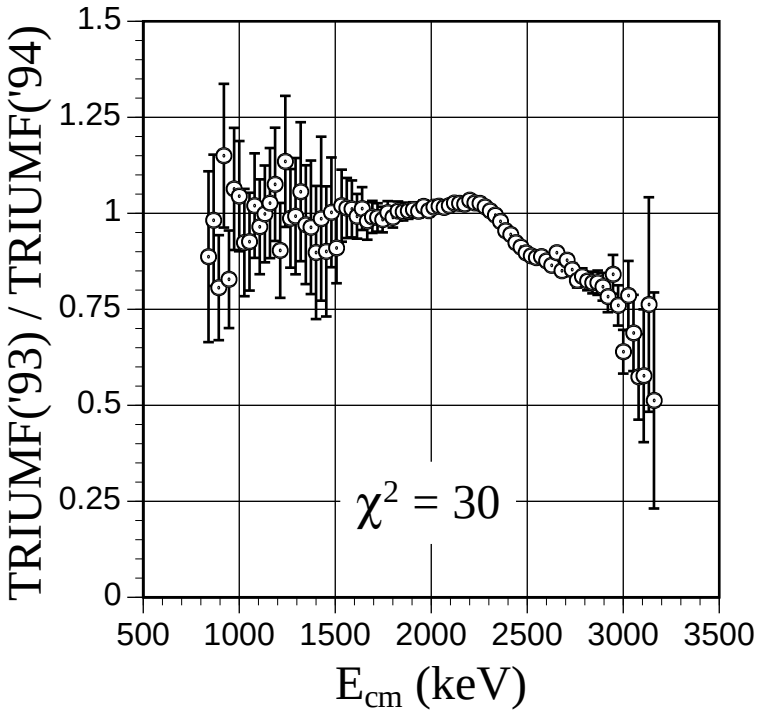

Figure 6.8: Ratio of TRIUMF(‘93) to TRIUMF(‘94) data sets. Note the systematic deviation at high energies (beginning immediately after the peak at 2360 keV). These are from two different analyses of the same data set. The TRIUMF(‘94) data set and **R**-Matrix fitted curve were used elsewhere throughout this work.

VII: Conclusion

We have measured the beta-delayed alpha-particle emission of ^{16}N with high statistics (nearly 280,000 counts in the final adjusted spectrum). Our line shape is corrected through the use of measured quantities and is well determined. Our data set largely agrees with the Seattle('95) results and thus the Mainz('71) results while it does not agree with the TRIUMF('94) results. These data sets fail to adequately determine the width of the primary peak, the low energy tail of which has a significant effect on the depth of the interference minimum. Without clear knowledge of this minimum, the f-wave component cannot be determined and subtracted out to give a clean p-wave spectrum.

We conclude that with the current available ^{16}N beta-delayed alpha-particle emission data sets the p-wave S-factor of the $^{12}C(\alpha,\gamma)^{16}O$ reaction cannot be determined at this stage with the accuracy (of 15-20%) required for stellar evolution models.

REFERENCES

[Az94] R.E. Azuma, L. Buchmann, F.C. Barker, C.A. Barnes, J.M. D'Auria, M. Dombsky, U. Giesen, K.P. Jackson, J.D. King, R.G. Korteling, P. McNeely, J. Powell, G. Roy, J. Vincent, T.R. Wang, S.S.M. Wong, and P.R. Wrean. *Phys. Rev.*, **C50**(1994)1194.

[Ba67] F.C. Barker. *Aust. J. Phys.*, **20**(1967)341.

[Ba68] F.C. Barker, H.J. Hay, and P.B. Treacy. *Aust. J. Phys.*, **21**(1968)239.

[Ba69] F.C. Barker. *Aust. J. Phys.*, **22**(1969)293.

[Ba71] F.C. Barker. *Aust. J. Phys.*, **24**(1971)777.

[Ba87] F.C. Barker. *Aust. J. Phys.*, **40**(1987)25.

[Ba88] D. Baye and P. Descouvemont. *Nuclear Physics*, **A481**(1988)445.

[Ba96] F.C. Barker, private communication.

[Ba96a] C.A. Barnes, private communication.

[Be68] H.A. Bethe. *Physics Today*, **21:9**(1968)36.

[Be85] H.A. Bethe and G. Brown. *Scientific American*, **252:5**(1985)60.

[Bi54] J.W. Bitner and R.D. Moffat. *Phys Rev.* **96**(1954)374.

[Bl79] J.M. Blatt and V.F. Weisskopf. *Theoretical Nuclear Physics*. Dover Publications Inc. 1979.

[Bo72] W. Bohne, J. Bommer, H. Fuchs, K. Grabisch, H. Kluge, and G. Roschert. *Nuc. Phys.* **A196**(1972)41.

[Bo77] J.E. Bond and F.W.K. Firk. *Nuc. Phys.* **A287**(1977)317.

[Br70] C. Brassard. Ph.D. Thesis. Yale University 1970.

[Bu93] L. Buchmann, R.E. Azuma, C.A. Barnes, J.M. D'Auria, M. Dombsky, U. Giesen, K.P. Jackson, J.D. King, R.G. Korteling, P. McNeely, J. Powell, G. Roy, J. Vincent, T.R. Wang, S.S.M. Wong, and P.R. Wrean. *Phys. Rev. Lett*. **70**(1992)726.

[Ch84] S. Chandrasekhar. *Review of Modern Physics*, **56**(1984)137.

[Cl83] D.D. Clayton. *Principles of Stellar Evolution and Nucleosynthesis.* University of Chicago Press, 1983.

[Dy74] P. Dyer and C.A. Barnes. *Nuc. Phys.* **A233**(1974)495.

[Fo84] W.A. Fowler. *Rev. Mod. Phys*., **58**(1984)149.

[Ga92] R.F. Garrison. In S.P. Maran editor, *The Astronomy and Astrophysics Encyclopedia*, page736, Van Nostrand Reinhold, 1992.

[Ha91] M. Harwit. *Astrophysical Concepts.* 2nd edition, corrected 2nd printing, Springer-Verlag, 1991. $\eta = \frac{Z_1 Z_2 e^2}{\hbar v}$

[Ha96] G.M. Hale. Proc. Conf. on Nuclei in the Cosmos '96, Notre Dame, 1996, to be published, and private communication.

[Ho54] F. Hoyle. *Astrophys. J. Suppl*., **1**(1954)121.

[Hu52] D.T. Hurd. *An Introduction to the Chemistry of the Hydrides.* John Wiley and Sons, 1952.

[Hu91] J. Humblet, B.W. Fillippone, and S.E. Koonin. *Phys. Rev*., **C44**(1991)2530.

[Ji90] X. Ji, B.W. Fillippone, J. Humblet, and S.E. Koonin. *Phys. Rev*., **C41**(1990)1736.

[Jo62] C. Miller Jones, G.C. Phillips, R.W. Harris, and E.H. Beckner. *Nuc. Phys.* **37**(1962)1.

[Ke82] K.U. Kettner, H.W. Becker, L. Buchmann, J. Görres, H. Kräwinkel, C. Rolfs, P. Schmalbrock, H.P. Trautvetter, and A. Vlieks. *Z. Phys. A-Atomic and Nuclei*, **308**(1982)73.

[Ko74] S.E. Koonin, T.A. Tombrello, and G. Fox. *Nuc. Phys.* **A220**(1974)221.

[Kr88] R.M. Kremer, C.A. Barnes, K.H. Chang, H.C. Evans, B.W. Filippone, K.H. Hahn, and L.W. Mitchell. *Phys. Rev. Lett.* **60**(1988)1475.

[La58] A.M. Lane, and R.G. Thomas. *Rev. Mod. Phys*., **30**(1958)257.

[La83] K. Langanke and S.E. Koonin. *Nuc. Phys.* **A410**(1983)334

[La85] K. Langanke and S.E. Koonin *Nuc. Phys.* **A439**(1985)384

[Le67] F.A. Lewis. *The Palladium Hydrogen System*. Academic Press, 1967.

[Ne74] K. Neubeck, H. Schober, and H. Waffler. *Phys. rev.* **C10**(1974)320.

[No70] L.C. Northcliffe and R.F. Schilling. *Nuclear Data Tables.* **7**(1970)233.

[No91] K. Nomoto, T. Shigeyama, S. Kumagi, and H. Yamaoka. In S.E. Woosley editor, *Supernovae: The Tenth Santa Cruz Summer Workshop in Astronomy ans Astrophysics*, page 176, Springer-Verlag, 1991.

[Ou92] J.M.L. Ouellet, H.C. Evans, H.W. Lee, J.R. Leslie, J.D. MacArthur, W. McLatchie, H.-B. Mak, P. Skensved, J.L. Whitton, and X. Zhao. *Phys. Rev. Lett.*, **69**(1992)1896.

[Pl87] R. Plaga, H.W. Becker, A. Redder, C. Rolfs, and H.P. Trautvetter. *Nuc. Phys.* **A465**(1987)291.

[Po95] J.D. Powell, R.E. Azuma, L. Buchmann, F.C. Barker, C.A. Barnes, J. D`Auria, M. Dombsky, K.P. Jackson, J.D. King, R.G. Korteling, P. McNeely, G. Roy, J. Vincent, S.S.M. Wong, and P.R. Wean. In A. Astbury, B.A. Cambel, W. Israel, F.C. Khanna, D. Page, and J.L. Pinfold editors, *Proceedings of the Ninth Lake Louise Winter Institute, Particle Physics and Cosmology*, page 468, World Scientific, 1995.

[Po96] J.D. Powell, private communication

[Re87] A. Redder, H.W. Becker, C. Rolfs, and H.P. Trautvetter. *Nuc. Phys.* **A462**(1987)385.

[Ro88] C.E. Rolfs and W.S. Rodney. *Cauldrons in the Cosmos*. Chicago, 1988.

[Sc77] D.N. Schramm and R.V. Wagoner. *Rev Nucl. Sci*., **27**(1977)37.

[Sh67] B.L. Shaw. *Inorganic Hydrides*. Pergamon Press, 1967.

[Sh82] F.H. Shu. *The Physical Universe*. University Science Books, 1982.

[Sp61] F.H. Spedding and A.H. Daane. *The Rare Earths*. John Wiley and Sons, 1961.

[Te52] T. Teichmann and E.P. Wigner. *Phys. Rev.*, **87**(1952)123.

[Th49] P.C.L. Thorne and E.R. Roberts. *Inorganic Chemistry*. Interscience, 1949.

[Ti93] D.R. Tilley, H.R. Weller, and C.M. Cheves, *Nuc. Phys.* **A564**(1993)1.

[Wa86] E.K. warburton. *Phys. Rev.* **C33**(1986)303.

[We80] T.A. Weaver and S.E. Woosley. Ann. NY Acad. of Sci. **336**(1980)335.

[We93] T.A. Weaver and S.E. Woosley. *Pysics Reports*, **227**(1993)65.

[Wi47] E.P. Wigner and L. Eisenbud. *Physical Review*, **72**(1947)29.

[Wi96] E.L. Wilds, Ph.D. Thesis. University of Connecticut. 1996.

[Wo86] S.E. Woosley and T.A. Weaver. *Ann. Rev. Astron. Astrophys*., **24**(1986)205

[Zh93a] Z. Zhao. Ph.D. Thesis. Yale University. 1993.

[Zh93b] Z. Zhao, R.H. France III, K.S. Lai, S.L. Rugari, M. Gai, and E.L. Wilds. *Phys. Rev. Lett.*, **70**(1993)2066.

[Zh93c] Z. Zhao, R.H. France III, K.S. Lai, M. Gai, E.L. Wilds, R.A. Kryger, J.A. Winger, and K.B. Beard. *Phys. Rev*., **C48**(1993)429.

[Zh93e] Z. Zhao, private communication.

[Zh95] Z. Zhao, L. DeBrackeleer, and E.G. Adelberger, 1995, to be published, and private communication.

[Zi77] J.F. Ziegler. *Stopping Powers and Range in all elements*. Pergamon Press, 1977.

[Zi92] J.F. Ziegler. *TRIM'92* manual.